Magnetic resonator structures as sensors with wireless magnetic read out

Master Thesis

Author(s):
Eberle, Patric

Publication date:
2010

Permanent link:
https://doi.org/10.3929/ethz-a-006885407

Master Thesis

Magnetic Resonator Structures as Sensors with Wireless Magnetic Read Out

Patric Eberle

Olgaç Ergeneman
Adviser
Prof. Dr. Bradley J. Nelson
Institute of Robotics and Intelligent Systems
Swiss Federal Institute of Technology Zurich (ETH)

2010-10

IRIS
Institute of Robotics and Intelligent Systems

ETH
Eidgenössische Technische Hochschule Zürich
Swiss Federal Institute of Technology Zurich

Preface

First of all, I would like to thank Olgaç Ergeneman for offering this fascinating master project to me and for being again a great advisor. His thorough understanding of the subject, his patience in explaining me the cleanroom work and the constructive discussions provided an excellent and stimulating support.

I would like to thank also Marcel Suter from the micro - and nanosystems group. His process for the fabrication of magnetic nanoparticle polymer composite structures served as an excellent base for the CoNi fabrication process. I greatly appreciated his continuing support.

Some special thanks I want to convey to George Chatzipirpiridis for his ideas for the design of the mechanical parts and for machining of them. For the electroplating work and for the support to improve the adhesion of CoNi to the anchor layer I would like to thank Dr. Salvador Pane and Kartik Sivaraman.

I want to express my gratitude to Prof. Dr. Bradley Nelson for accepting me as a master student in the multi-scale robotics lab the Department of Mechanical and Process Engineering of ETH Zurich.

The atmosphere in the multi-scale robotics lab group has been all the time friendly and inspiringly. My gratitude goes also to all other members of the multi-scale robotics lab.

Abstract

A sensor system based on a magnetic resonator structure with wireless magnetic actuation and wireless magnetic read out is presented in this thesis. The resonator structures are intended for mass sensing for the detection of e.g. bio-molecules and are designed as disposables. Cobalt-nickel and magnetic nanoparticle polymer composite materials are employed for the resonator structures. The cobalt nickel resonator structures are fabricated by photolithography and electroplating. The magnetic nanoparticle polymer composite structure is made of SU-8 with distributed superparamagnetic iron-oxide nanoparticles (mean diameter $>$ 8 nm) and structured by photolithography. Typical resonator structure sizes vary from $50 - 400\,\mu$m (L) x $50 - 400\,\mu$m (W) x $1 - 3\,\mu$m (th). CoNi structures have a thickness of up to $12\,\mu$m (th).

This work focuses on the fabrication of the CoNi structures and the wireless magnetic read out of magnetic resonators. An electromagnet applies a magnetic force to excite the resonator structure and the magnetic field change of the oscillating structure is detected by pick-up coils. Adsorbing species alter the mass of the functionalized sensor and the mass change results in a shift of the resonant frequency. The resonant frequency is measured with a probe signal and a lock-in amplifier in order to increase the sensitivity and reduce the thermal electronic noise effects. Specific analytical models were derived and numerical simulations performed to predict the read out signal and optimize the coils. By using several types of resonator structures, the successful read out and resonant frequency detection of in-plane and out-plane oscillations were experimentally demonstrated. The deployment of a CoNi structure as a mass sensor with wireless magnetic read out was shown. Successfull operation in water was demonstrated with an in-plane resonator. Additionally, the read out of a magnetostrictive sensor was shown.

Zusammenfassung

Ein Sensorsystem basierend auf einem magnetischen Resonator mit drahtlosem magnetischem Ansteuern und Auslesen wird in dieser These präsentiert. Die Resonatorstrukturen sind als Massensensor zur Detektion von z.B. Biomolekülen vorgesehen und sind als Einwegartikel (Disposable) ausgefürt. Cobalt-Nickel und magnetische Nanopartikel Polymer Verbindungen werden als Materialien für die Resonatorstrukturen eingesetzt. Die Cobalt-Nickel Strukturen werden mit Photolithographie bemustert und mit Elektroplating aufgebracht. Die Strukturen aus magnetischer Nanopartikel Polymer Verbindung werden aus SU-8 mit verteilten superparamagnetischen Eisenoxid Nanopartikeln (mittlerer Durchmesser 8 nm) hergestellt und strukturiert mit Photolithographie. Typische Resonatorstrukturen variieren von $50 - 400\,\mu$m (L) x $50 - 400\,\mu$m (W) x $1 - 3\,\mu$m (th). CoNi Strukturen weisen eine Dicke von bis zu $6\,\mu$m (th) auf.

Diese Arbeit befasst sich mit der Fabrikation von CoNi Strukturen und mit dem drahtlosen magnetischen Auslesen von magnetischen Resonatoren. Ein Elektromagnet erzeugt eine magnetische Kraft zur Anregung der Resonatorstruktur und die Magnetfeldänderung durch die oszillierende Struktur wird mit einer Pick-up Spule detektiert. Adsorbierende Spezies verändern die Masse des funktionalisierten Sensors und die Massenänderung bewirkt eine Verschiebung der Resonanzfrequenz. Die Resonanzfrequenz wird mit einem Probe-Signal und einem Lock-In Verstärker gemessen, um die Sensitivität zur erhöhen und um die Auswirkungen des thermischen elektronischen Rauschens zu reduzieren. Spezifische analytische Modelle wurden hergeleitet und numerische Simulationen durchgeführt, um das Auslesesignal vorauszuberechnen und die Spulen zu optimieren. Das Auslesen und die Bestimmung der Resonanzfrequenz von Oszillationen in der Ebene und aus der Ebene wurde erfogreich experimentell demonstriert anhand von verschiedenen Typen von Resonatorstrukturen. Der Verwendung einer CoNi Struktur als Massensensor mit drahtlosem magnetischem Auslesen wurde aufgezeigt. Der erfolgreiche Betrieb in Wasser eines in der Ebene oszillierenden Resonators wurde demonstriert. Zustzlich wurde das Auslesen eines magnetostriktiven Sensors gezeigt.

Contents

List of Tables

List of Figures

Notation

Latin Letters:

$\vec{A}$	Vector Potential
a	Parameter
$\vec{B}$	Magnetic Flux Density
b	Parameter
C	Capacitance
c	Constant
f	Frequency
g	Substituted Function
$\vec{D}$	Electric Flux Density
$\vec{E}$	Electric Field Strength
E	Energy or Young's Modulus
$\vec{F}$	Force
G	Green's Function or Gain of Power Amplifier
$\vec{H}$	Magnetic Field Strength
$\vec{I}$	Normalized Derivative Field
I	Electric Current
$\vec{J}$	Current Density
k	Spring Constant
k_B	Boltzmann Constant $1.3806504 \cdot 10^{-23}\,\mathrm{J/K}$
L, l	Length
L	Inductance
$\vec{M}$	Magnetization
m	Mass
$\mathbf{N}$	Demagnetization Matrix
N	Number of Windings
n	Integer
$\vec{P}$	Polarization
P	Power
Q	Quality Factor

$\vec{R}$	Normalized Field
R	Resistance
$\vec{r}$	Coordinate Vector
S	Surface Area
s	Laplace Parameter
T	Absolute Temperature or Transfer Function
t	Time
th	Thickness
U	Electrical Voltage
u	Function Substitution
V	Volume
v	Function Substitution
W, w	Width
x	Spatial Coordinate
y	Spatial Coordinate
z	Spatial Coordinate

Greek Letters:

β	Function Substitution
χ	Magnetic Susceptibility
δ	Damping Ratio or Skin Depth
ϵ	Parameter
ϵ_0	Electric Permittivity of Vacuum $8.854 \cdot 10^{-12}\,\mathrm{F/m}$
ϵ_r	Relative Electric Permittivity
ϕ	Magnetic Flux
φ	Scalar Potential Field or Phase
Γ	Field Distribution Function
γ	Approximation Function
λ	Approximation Function
μ_0	Magnetic Permeability $4\pi \cdot 10^{-7}\,\mathrm{Vs/Am}$
μ_r	Relative Magnetic Permeability
ν	Poisson's Ratio
ρ	Specific Resistance or Volume Charge Density
σ	Surface Charge Density
ω	Angular Frequency
∇	Nabla Operator
$\times$	Vector Cross Product

1 Introduction

Lab-on-a-chip systems promise high measurement accuracy and short processing times. In a chip integrated mass sensors offer high sensitivity and can be used for e.g. to detect biomolecules, cells, nanoparticles. Sensors designed as disposable allow ease of use and a high throughput of measurement cycles since the cleaning process can be omitted. Disposable sensors must be necessarily cost efficient and have to be, thus, fabricated with low cost materials in a cost efficient process. Additionally, wireless actuation and read out is required to keep the sensor design simple. Furthermore, easy functionalization of the surface is demanded. Typically, such sensor systems are operated in a microfluidic environment.

This work deals with magnetic resonator structures employed as sensors and in particular with the wireless magnetic read out of magnetic resonator structures. A wireless magnetic read out system was designed, which has some unique advantages compared to light based read out methods. The sensors were operated at their resonant frequency and the shift in resonant frequency was used to detect the mass or viscosity change. Resonator structures made of cobalt nickel (CoNi) and magnetic nanoparticle polymer composite (MPC) were used. The CoNi structures were fabricated in this work, while the MPC structures were provided by the micro- and nanosystems group of ETH.

1.1 Objective and Outline of this Work

The objective of the work was to design a sensor system based on a magnetic resonator with wireless magnetic actuation and wireless magnetic read out. Previous work had been done on the wireless actuation of the MPC structures in [17] and some preliminary studies had been done on the wireless magnetic read out in [13]. The read out work included the analysis, modeling and simulation of the read out signal, the design and simulation of the experimental setup and the conduction of read out experiments for different resonator structures. MPC structures are more difficult to read out due to their rather low magnetic nanoparticle concentration and magnetization capability, respectively. Several types of resonator structures were read out. It began with the read out of rather big-sized structures made of

full magnetic material and continued to small sizes until MPC structures were attempted to read out.

Resonator structures were fabricated made of CoNi. The structures were patterned by photholithography and CoNi was electroplated. As anchor, a layer of SU-8 was used, which was formed by a second photholithography step. The design of the CoNi structures is the same as of the MPC structures and the same masks for the photolithography processings were used. Since the CoNi structures were deviated from the MPC structures, large portions of the MPC fabrication process could be adopted for the CoNi process. In principal, the structural MPC layer was exchanged by a CoNi layer. CoNi structure sizes vary from $50 - 400\,\mu m$ length(L), $50 - 400\,\mu m$ width(W), $6 - 12\,\mu m$ thickness(th).

As mentioned in the previous section, the MPC structures were provided by the micro- and nanosystems group of ETH.

1.2 The MPC Project

Magnetic polymer composites are promising materials for microactuators, they combine the advantages of polymers with magnetic materials. The polymer composite allows easy fabrication, currently with a few process steps in a cleanroom environment, and later on injection mold based fabrication can be considered. It offers also product cost effectiveness, easy functionalization, ease of use and biocompatibility. The embedded magnetic nanoparticle allow wireless actuation and read out. Structure sizes vary actually from $50 - 400\,\mu m$(L), $50 - 400\,\mu m$(W), $1 - 3\,\mu m$(th).

The magnetic nanoparticle polymer composite (MPC) structure is based on a photosensitive polymer matrix SU-8 and uniformly distributed superparamagnetic nanoparticles Fe_3O_4 with a mean diameter of 8 nm (M. Suter *et al.* [43]). Uniform distribution of the nanoparticle is achieved due to the superparamagnetic property of the nanoparticles and by the aid of a surfactant. Currently, a nanoparticle volume concentration of up to 5% has been attained. Larger concentrations impair the photolithography based fabrication process and degrade

the quality of the structures. Superparamagnetic materials exhibit no remanent magnetization and no hysteresis in the magnetization characteristic. An external magnetic field is required to magnetize the MPC structures.

Two research institutions contribute to the project. The micro- and nanosystems group (MNS) works on the development of the fabrication process of the MPC and the design of the resonator structures. The multi-scale robotics lab (IRIS) works on the wireless actuation and read out of the MPC structures. In the current state of the project, successful fabrication [43] with a nanoparticle volume concentration of 1-5% and succesful wireless actuation [17] of the MPC structures has been demonstrated.

During the last year, the project has moved towards lateral oscillating structures due to the lower damping factor compared to the vertical oscillating structures. Damping of vertical oscillating structures becomes critical when the structure is operated in liquids. For lateral oscillating structures the fluidic resistance is much lower.

1.3 Functional Principle

The sensor is designed as a resonator structure for the purpose of mass sensing. Structures can be cantilevers or plate-like structures suspended by a spring. The sensing structure is functionalized by acceptors and actuated in its mechanical resonant frequency. The specific molecules or particles to be sensed attach on the functionalized surface and increases the mass of the structure. Hence, the resonant frequency changes due to the additional mass and the analyte can be detected. Mass change sensors that work based on the resonant frequency shift principle are less susceptible to electronic thermal noise than strain based sensors. In particular in micro- and nanosystems electronic thermal noise represents one of the critical problems to overcome because of the usually weak signal levels. Detecting a resonant shift is far less error prone than measuring an analogous quantity in a system with low signal to noise ratio. Frequencies can be measured with high accuracy and resolution.

1.4 Application

Sensors based on resonator structures are used for a variety of applications in bio-, chemical sensing and material science and have been intensively studied from a number of research groups around the globe already for many years. Applications include weighing of biomolecules, single cells, single nanoparticles [10], ions and heavy metals. Specific species are recognized by an appropriate functionalization of the resonator structure. Such sensing systems are already commercially available and spin-off companies have been founded. Biosensor products represent a fast growing segment within the biotechnology market.

1.5 The Sense of the Magnetic Read Out

It is, however, not so obvious why a magnetic read out system should be employed, since very precise laser doppler vibrometer read out devices have been available already for years.

There is, indeed, one distinct and very obvious disadvantage of laser based read out methods. The laser based read out requires to see the resonator structure and a light transparent channel must exist from the laser source to the resonator structure. If the resonator structure is for e.g. embedded in a flow channel, the flow channel must be designed transparent at least in the region of the resonator structure. Moreover, the liquid in the flow channel needs to be transparent as well. Absorption of the laser beam may become a problem in the flow channel material and the liquid. High refractive index of the liquid may lead to reflections at the interfaces liquid flow channel or flow channel air of the resonator reflected laser beam.

For magnetically excited resonator structures, the resonator structures are often hidden by the excitation coil and a hole in the excitation coil is needed for the laser beam. The hole has typically a high aspect ratio and if the reflected beam of the resonator structure is slightly tilted, the beam hits the wall of the hole and is absorbed there. Tilting of the reflected beam occurs, if the entrance - and exit angle of the laser beam to the resonator structure is not perpendicular.

In practical applications it occurs easily for bended - and misaligned structures.

A magnetic read out method overcomes the difficulties mentioned above due to its magnetically based read out principal. There is neither transparency of the flow channel nor of the liquid required. However, it is essential to place the pick-up coils as close as possible to the resonator structure. As intuitively expected and as demonstrated by this thesis, the magnetic based read out has a significant lower sensitivity than a laser doppler vibrometer. The magnetic read out can typically read out µm deflections while the laser dopper vibrometer reaches pm detection capability. On the other side, the magnetic read out can be designed substantially more cost efficient due to the simpler designs. At the bottom line, for magnetic resonator structures with moderate sensitivity requirements, the magnetic read out represents an attractive alternative especially if the sensor system is commercialized. For commercialization, the magnetic read out should be preferably fully integrated in order to leverage the cost advantage.

2 Read Out Strategy

In [13] several read out methods for magnetic resonators were presented and analyzed. For this work, the most promising method was selected, further developed and implemented. In principal, the read out method is based on the frequency response of the system. The system is excited with a sine signal, while the response of the system is monitored and the sine frequency is swept over a frequency band. This section describes the read out principle in an intuitive way. A full mathematical treatment of the problem can be found in the simulation section 3.

If the excitation frequency is swept over a band including the resonant frequency, at the resonant frequency the deflection amplitude of the resonator structure becomes maximal and the phase lag between excitation and response signal changes distinctively. Either effect can be used to detect the resonant frequency.

Figure 1 illustrates schematically the arrangement with excitation -, probe - and pick-up coils. The excitation coil, which is driven by an alternating current (AC), generates the excitation field and the excitation field provokes a mechanical force at the resonator structure. Magnitude and direction of the force are determined by the gradient of the excitation magnetic field and the magnetization of the resonator structure. In order to increase the force an additional DC field component can be superposed which is uniform over the resonator structure. The DC component is not illustrated in figure 1. A probe coil generates the probe field used to detect the resonator structure vibration. Two pick-up coils are arranged symmetrically to the probe coil and connected differentially to cancel the voltage induced by the probe field. No cancellation of the probe field decreases the sensitivity, since the signal level is larger at the input of the following lock-in amplifier and may most likely saturate the input. If the resonator structure deflects, the magnetic flux in the pick-up coil changes and a voltage is induced according to the law of Faraday.

$$U_{P,A/B} = -\frac{d}{dt}\int_{S_{A/B}} \vec{B}d\vec{S} \tag{2.1}$$

$$\tag{2.2}$$

whereas $S_{A/B}$ represents the effective area of pick-up coil A or B. Since pick-up coil A is much closer to the resonator structure, the resonator structure induces mainly a voltage in pick-up coil A. The difference voltage can be used to monitor the resonator structure vibration.

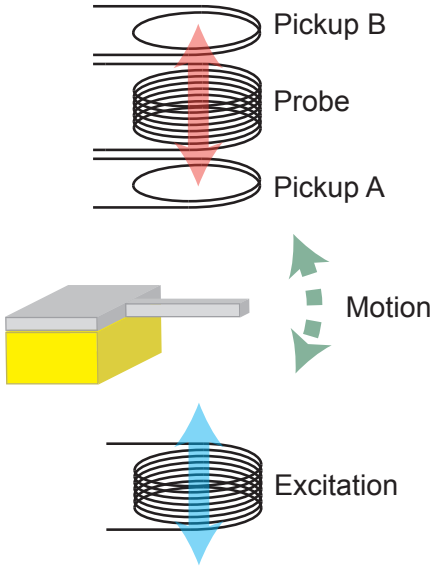

Figure 1: Schematic illustration of actuation and read out arrangement. The resonator structure is shown by a cantilever.

2.1 Mechanical Model of Resonator Structure

In [48], a useful summary and overview of the beam theory with solutions of the Euler-Bernoulli differential equation is given. Interested readers are encouraged to look at this publication. For the resonator structure deflection, the model of a mass-spring-damper system can be used. Mestroma *et al.*[31] propose this Ansatz, which seems very intuitive and reasonable. The mass-spring-damper sys-

tem is described by a second order ordinary differential equation (ODE).

$$\ddot{z} + 2\delta\omega_0\dot{z} + \omega_0^2 = \frac{F_e}{m} \tag{2.3}$$

$$\omega_0 = \sqrt{\frac{k}{m}} \tag{2.4}$$

where m, k, δ, ω_0, F_e are the mass, spring constant, damping ratio, the natural angular frequency and the excitation force.

Figure 2 depicts the frequency response of the second order system. Eye catching is the overshoot of the amplitude and the distinctive phase change in the vicinity of the resonant frequency. Both effects depend on the damping ratio. Increasing damping ratios decrease the amplitude overshoot and phase change rate. The deflection amplitude and phase of the resonator structure affect the pick-up voltage, which is explained in more detail in the following sub section.

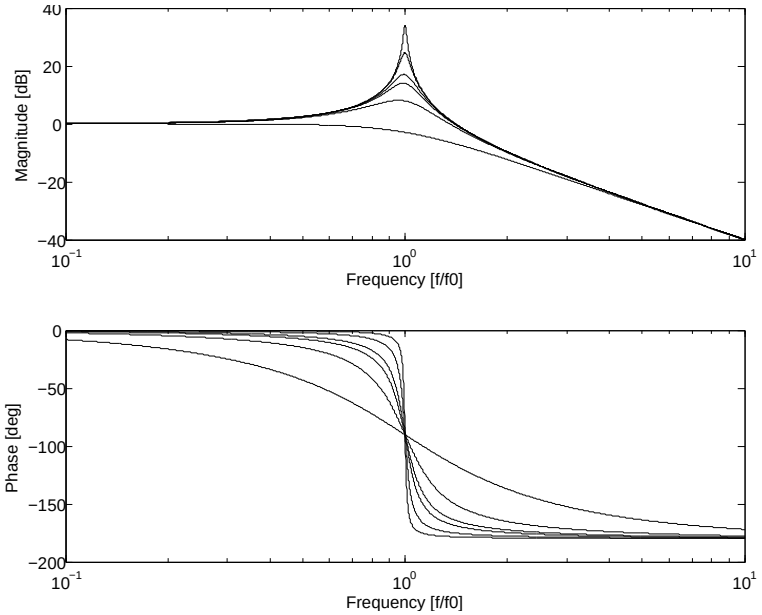

Figure 2: Frequency response of the second order system for six different damping ratios $\delta = [0.01, 0.03, 0.07, 0.1, 0.2, 0.7]$. A lower damping ratio increases the overshoot and phase slope around the resonant frequency.

2.2 Modulation Effect

If the resonator structure vibrates mechanically an amplitude modulation of the pick-up signal in the time domain or a frequency shifting effect in the frequency domain occurs. As mentioned earlier, this section focuses on an intuitive explanation of the effects and a full mathematical investigation can be obtained in the simulation section 3.

Figure 3 illustrates schematically the resonator structure with pick-up coil and the modulated spatial induced magnetic field. If the resonator structure deflects the spatial magnetic field shifts linearly by the amount of the deflection, called z_d. In case of a sinusoidal deflection the pick-up coil experiences a sinusoidal field change at the point of the pick-up coil z_p. The last assumes a linear spatial field distribution around z_p. The resonator structure itself is magnetized by the excitation field resulting in a magnetization component M_{DC} and M_{AC}. M_{DC} and M_{AC} induce a magnetic field with a spatial circumference as depicted by the function $B_{I0} * \Gamma_z(z)$ (see figure 3). $\Gamma_z(z)$ represents the spatial field distribution function normalized at the resonator structure center $z = 0$ and B_{I0} is the magnitude of the field. B_{I0} is linearly proportional to M_{DC} and M_{AC} and is, thus, modulated by the alternating part M_{AC}. Hence, two magnetic field components are present within the pick-up coils and both components change according the deflection of the resonator structure with the vibration frequency f_m. While the first component has a constant amplitude from the DC magnetization M_{DC}, the amplitude of the second component is modulated with the alternating magnetization M_{AC}. In the frequency domain, the second magnetic field component consists of two frequency components at $f_e \pm f_m$.

If the DC magnetization M_{DC} is larger than the alternating magnetization M_{AC} the major force part acting on the resonator structure oscillates with the excitation frequency and, hence, the resonator structure mainly deflects with the excitation frequency. Due to the afore explained modulation effect, a frequency component appears at the second harmonic whose amplitude linearly depends on the deflection amplitude of the resonator structure. Therefore, the second harmonic can be used as a potential read out frequency. On the first harmonic, there is a large portion induced by the excitation field and the resonator structure

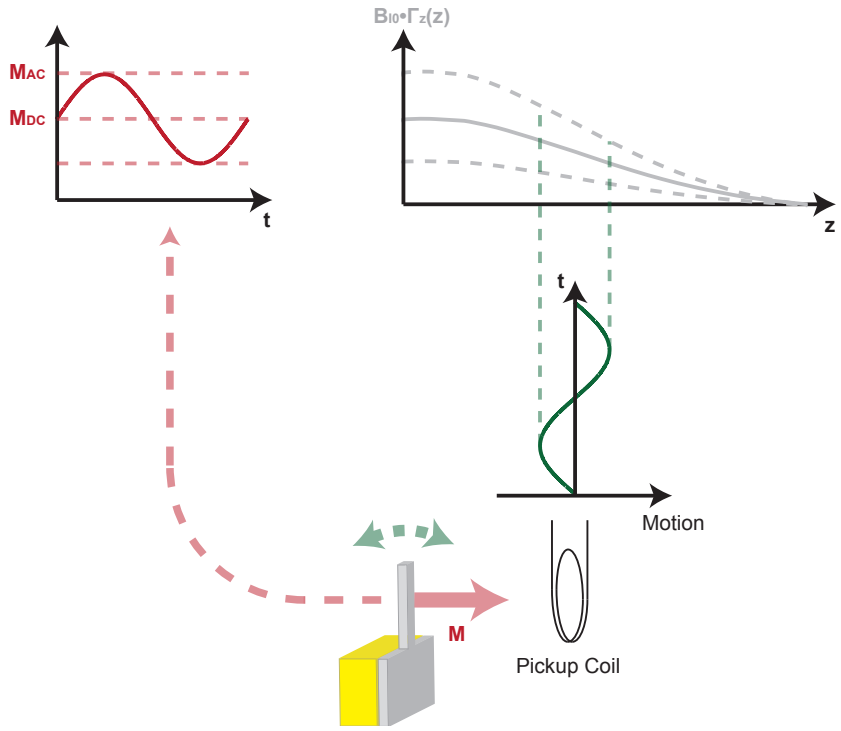

Figure 3: Schematic illustration of the resonator structure modulation effect.

induced signal is very small compared to that. Despite of the electronic compensation capability built in the amplification-compensation-signal-conditioning (ACSC) unit, it still remains hard to measure the resonator structure deflection on the first harmonic.

2.3 Modulation by Probe Field

For the probe magnetic field the same modulation and frequency shift occurs as described in the previous section 2.2. The probe field is superposed to the excitation field and generates an additional magnetization M_P at the resonator structure. Because of the superposition, care has to be taken not to exceed the saturation level of the magnetization characteristic of the resonator structure material. Some headroom has to be reserved for the probe field, hence DC -, excitation - and probe field have to be balanced out for best performance. The probe frequency is selected much higher than the excitation frequency. The resonator structure vibration induces two side bands at $\omega_p - \omega_m$ and $\omega_p + \omega_m$ due

to the modulation effect (see figure 4).

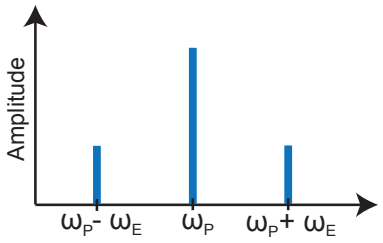

Figure 4: Main and first side band of the probe signal.

The side band is deployable as a resonator structure read out because its amplitude is a linear function of the deflection amplitude. However, highly attractive is the fact that the side band signal is amplified by the probe frequency, which represents a free selectable parameter and can be selected sufficiently large. Thereby, the read out sensitivity and signal to noise ratio can be improved significantly. It is obvious, there is an upper limit for the probe frequency in an experimental setup due to the limited bandwidth of the lab instruments, the employed coils and the magnetization frequency characteristic of the magnetic resonator material.

2.4 Frequency Response

The frequency is swept over a band centered at the resonant frequency of the resonator structure as depicted in figure 5.

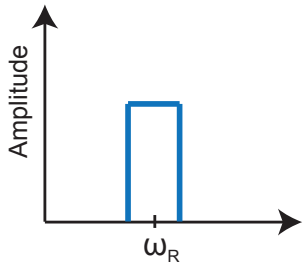

Figure 5: Excitation frequency sweep.

Figure 6 illustrates the received response in the pick-up coils at the second harmonic of the excitation frequency and the probe side band. At the second harmonic and the first side band of the probe frequency, the resonator structure deflection component oscillating at the excitation frequency is perceivable. The increased resonator structure deflection in the vicinity of the resonance results in a overshoot in the response at the second harmonic of the excitation frequency (see 6(a)) and a larger overshoot in the response at the first side band (see 6(c)). Coinciding with the overshoot in magnitude, a distinctive phase change at the second harmonic and at the first side band is noticeable around the resonant frequency (see (b) and (d)).

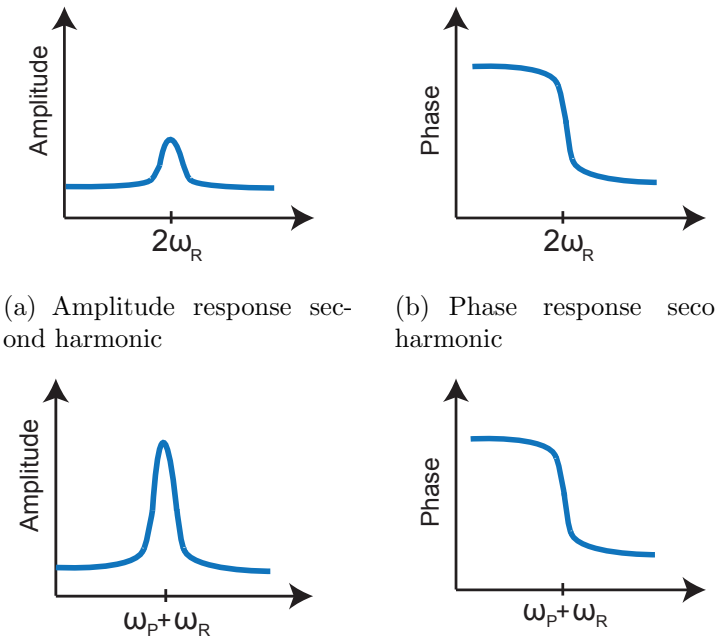

(a) Amplitude response second harmonic

(b) Phase response second harmonic

(c) Amplitude response side band

(d) Phase response side band

Figure 6: Expected frequency response at resonance at the second harmonic and the first side band of the probe frequency.

If the resonator structure AC magnetization is larger than the DC magnetization ($M_{AC} > M_{DC}$) the resonator structure is mainly actuated with twice of the excitation frequency. The main component of the force acting on the resonator structure oscillates with twice of the excitation frequency. In this case, the excitation signal should run with half of the resonant frequency. Potential read out

candidates are then the third harmonic and the second probe side band $f_P \pm 2f_E$, since their signal is proportional to the resonator structure deflection. However, as expected, the read out on the second probe side band outperforms the third harmonic due to the amplification property of the probe side band.

3 Simulation and Modeling of the Read Out Signal System

3.1 Introduction

The simulation and modeling work presented in this section investigates the physical relation of the induced pick-up signal in function of the resonator structure magnetization, the resonator structure oscillation, the dimensions and arrangement of resonator structure and pick-up coil. The derived model predicts accurately the received frequency spectrum and the respective amplitudes. It allows the determination of the optimal pick-up coil geometry and location without performing parameter sweeps. Hence, the model can be used as a tool for feasibility studies and optimization tasks. For the following analytical derivations it is beneficial but not absolutely required, if the reader is familiar with the main results and derivations presented in the previous work [13].

3.2 Field Analysis

The pick-up signal is governed by the set of Maxwell and constitutive equations. For convenience and completeness, all equations are given here but not discussed in detail. The respective literatures ([27], [21]) is recommended for readers interested in the detailed derivations and descriptions.

$$\nabla \times \vec{H} = \vec{J} + \frac{\partial \vec{D}}{\partial t} \tag{3.1}$$

$$\nabla \cdot \vec{B} = 0 \tag{3.2}$$

$$\nabla \times \vec{E} = -\frac{\partial \vec{B}}{\partial t} \tag{3.3}$$

$$\nabla \cdot \vec{D} = \rho \tag{3.4}$$

These derivative equations can be transformed into integral equations by applying the divergence (Gauss) or curl (Stokes) theorem. The integral form is in some cases more convenient to use.

In the above equations 3.1 - 3.4 the following definitions are used:

$\vec{H}$	Magnetic field [A/m]
$\vec{B}$	Magnetic flux density [T]
$\vec{E}$	Electric field [V/m]
$\vec{D}$	Electric flux density [As/m^2]
$\vec{J}$	Electric current density [A/m^2]
ρ	Electric charge density [As/m^3]

The Maxwell equations are completed by the constitutive equations, which introduce the material properties into the mathematical relations:

$$\vec{B} = \mu_0(\vec{H} + \vec{M}) \tag{3.5}$$
$$\vec{D} = \epsilon_0(\vec{E} + \vec{P}) \tag{3.6}$$

where $\vec{M}$ [A/m] is the magnetization, $\vec{P}$ [As/m^2] is the polarization and $\mu_0 = 4\pi * 10^{-7}$ Tm/A is the magnetic permeability and $\epsilon_0 = 8.854 * 10^{-12}$ F/m the electric permittivity of vacuum.

In the present application case regarding the induction of a pick-up signal voltage by the oscillation of a resonator structure the used frequency range is from a few kHz up to about 20 MHz. Thus, the $\frac{\partial \vec{D}}{\partial t}$ component in the Maxwell equations can be neglected, since the wavelength in free space is much larger than the pick-up coil arrangement. This is the so called quasi-static case. The set of Maxwell equations required to compute the magnetic field is reduced and simplified to:

$$\nabla \times \vec{H} = \vec{J} \tag{3.7}$$
$$\nabla \cdot \vec{B} = 0 \tag{3.8}$$

The above set of equations 3.7 hold true for static and quasi static magnetic fields. In the quasi-static case, the magnetic field induced by the resonator structure magnetization changes instantaneously when the magnetization changes in time. For example a permanent magnet serves as a model for the magnetized

resonator structure in order to determine the magnetic field.

3.2.1 Vector Potential

The usage of a vector potential allows to combine the two magnetostatic equations 3.7 into one single equation by considering the constutive equation 3.5. Hence, the mathematical treatment is simplified. A vector potential $\vec{A}$ is introduced:

$$\vec{B} = \nabla \times \vec{A} \tag{3.9}$$

Substitute equation 3.9 into equation 3.7 and use the relation $\nabla \times \nabla \times \vec{A} = \nabla(\nabla\vec{A}) - \nabla^2\vec{A}$:

$$\begin{aligned} \nabla^2\vec{A} - \nabla(\nabla\vec{A}) &= -\mu_0\vec{J} && (3.10)\\ &= -\mu_0(\vec{J}_{free} + \nabla \times \vec{M}) && (3.11)\\ &= -\mu_0(\vec{J}_{free} + \vec{J}_m) && (3.12) \end{aligned}$$

where $\vec{J}_{free}$ represent the free current and $\vec{J}_m$ the internal current due to the magnetization $\vec{M}$.

The derivative definition 3.9 of the vector potential $\vec{A}$ allows to gauge the potential. By imposing the Coulomb gauge condition $\nabla \cdot \vec{A} = 0$, equation 3.10 reduces to:

$$\nabla^2\vec{A} = -\mu_0(\vec{J}_{free} + \vec{J}_m) \tag{3.13}$$

3.2.2 Scalar Potential

For current-free regions $\nabla \times \vec{H} = 0$ a scalar potential field φ_m Ansatz can be used to solve the magnetostatic field equations 3.7. A scalar potential field φ_m is introduced with the following relation to the irrotational magnetic field $\vec{H}$:

$$\vec{H} = -\nabla\varphi_m \tag{3.14}$$

Equation 3.14 and the constitutive relation $\vec{B} = \mu_0(\vec{H} + \vec{M})$ 3.5 is substituted into $\nabla \cdot \vec{B} = 0$ 3.8 and the scalar potential PDE is obtained:

$$\nabla^2\varphi_m \;=\; \nabla\vec{M} \tag{3.15}$$

3.2.3 Current Model

The current model [21] can be used in the analysis of permanent magnets. In this model, the magnet is reduced to a distribution of equivalent currents. This is then input into the magnetostatic field equations as a source term, and the field is obtained using standard methods for steady currents. The derivation of the current model starts with the vector potential field equation 3.13.

If there is no free current ($\vec{J}_{free} = 0$) and if it is assumed infinite homogeneous material (no boundaries), then the solution to equation 3.13 can be written in integral form using the free space Green's function $G(\vec{r}, \vec{r'}) = -1/(4\pi \left|\vec{r} - \vec{r'}\right|)$ for the operator ∇^2.

$$\vec{A} = \frac{\mu_0}{4\pi} \int \frac{\vec{J}_m(\vec{r'})}{\left|\vec{r} - \vec{r'}\right|} dv' \tag{3.16}$$

If the magnetization $\vec{M}$ is confined to a volume V (of permeability μ_0), and falls abruptly to zero outside of V, the following equations hold true:

$$\vec{A}(\vec{r}) = \frac{\mu_0}{4\pi} \int_V \frac{\vec{J}_m(\vec{r'})}{\left|\vec{r} - \vec{r'}\right|} dv' + \frac{\mu_0}{4\pi} \oint_S \frac{\vec{j}_m(\vec{r'})}{\left|\vec{r} - \vec{r'}\right|} ds' \tag{3.17}$$

and

$$\vec{B}(\vec{r}) = \frac{\mu_0}{4\pi}\int_V \vec{J}_m(\vec{r'}) \times \frac{\vec{r}-\vec{r'}}{\left|\vec{r}-\vec{r'}\right|^3}dv' + \frac{\mu_0}{4\pi}\oint_S \vec{j}_m(\vec{r'}) \times \frac{\vec{r}-\vec{r'}}{\left|\vec{r}-\vec{r'}\right|^3}ds' \qquad (3.18)$$

where $\vec{r}$ is the observation point, $\vec{r'}$ is the source point, S is the surface of the magnet and $\vec{J}_m$ and $\vec{j}_m$ are equivalent volume and surface current densities. These are defined in the following:

$\vec{J}_m$	Volume current density $[\,\mathrm{A/m^2}]$
$\vec{j}_m$	Surface current density $[\,\mathrm{A/m}]$

In equation 3.18 it has been used that:

$$\vec{B} = \nabla \times \vec{A} \qquad (3.19)$$

$$\nabla \times \frac{\vec{J}_m(\vec{r'})}{\left|\vec{r}-\vec{r'}\right|} = -\vec{J}_m(\vec{r'}) \times \nabla\frac{1}{\left|\vec{r}-\vec{r'}\right|} \qquad (3.20)$$

∇ denotes the differentiation to the unprimed coordinates $\vec{r}$.

3.2.4 Charge Model

The charge model [21] is another useful method for analyzing permanent magnets. In this model, a magnet is reduced to a distribution of equivalent "magnetic charge". The charge distribution is used as a source term in the magnetostatic field equations, and the fields are obtained using standard methods. The derivation of the charge model starts with scalar potential equation 3.15 for current-free regions $\nabla \times \vec{H} = 0$.

In the absence of boundary surfaces the solution to the scalar potential equation 3.15 in integral form using the free space Green's function $G(\vec{r}, \vec{r'})$ for the ∇^2 operator yields:

$$\varphi_m(\vec{r}) = -\frac{1}{4\pi}\int \frac{\nabla_{\vec{r'}} \cdot \vec{M}(\vec{r'}}{\left|\vec{r}-\vec{r'}\right|}dv' \qquad (3.21)$$

where $\vec{r}$ is the observation point, $\vec{r'}$ is the source point, $\nabla_{\vec{r'}}$ acts on the primed coordinates and the integration is over the volume for which the magnetization exists.

If $\vec{M}$ is confined to a volume V (of permeability μ_0), and falls abruptly to zero outside of this volume, then equation 3.21 becomes:

$$\varphi_m(\vec{r}) = -\frac{1}{4\pi}\int_V \frac{\nabla_{\vec{r'}} \cdot \vec{M}(\vec{r'})}{\left|\vec{r} - \vec{r'}\right|} dv' + \frac{1}{4\pi}\oint_S \frac{\vec{M}(\vec{r'}) \cdot \vec{\hat{n}}}{\left|\vec{r} - \vec{r'}\right|} ds' \tag{3.22}$$

where S is the surface that bounds V, and $\vec{\hat{n}}$ is the outward unit normal to S. The form of equation 3.22 suggests the definitions of volume and surface charge densities given in the following:

$$\rho_m = -\nabla \cdot \vec{M} \qquad \text{Volume charge density } [\,\mathrm{A/m^2}] \tag{3.23}$$

$$\sigma_m = \vec{M} \qquad \text{Surface charge density } [\,\mathrm{A/m}] \tag{3.24}$$

If the magnet is in free space, $\vec{B} = \mu_0 \vec{H}$, the field $\vec{B}(\vec{r})$ is obtained from equation 3.14 and 3.22:

$$\vec{B}(\vec{r}) = -\frac{\mu_0}{4\pi}\int_V \frac{\rho_m \cdot (\vec{r} - \vec{r'})}{\left|\vec{r} - \vec{r'}\right|^3} dv' + \frac{\mu_0}{4\pi}\oint_S \frac{\sigma_m \cdot (\vec{r} - \vec{r'})}{\left|\vec{r} - \vec{r'}\right|^3} ds' \tag{3.25}$$

3.3 Analytical Solution for the Pick-up Voltage

Figure 7 illustrates the situation of resonator structure and pick-up coil. It has to be noted, figure 7 shows schematically one geometrical form and arrangement of pick-up coil and magnet bar, but the derivations and equations in this section hold true for any other geometrical forms and arrangements and are, thus, generally valid. As shown in sub section 3.2, the magnetized resonator structure can be modeled as a permanent magnet to obtain the magnetic field. The permanent magnet is illustrated by the magnet bar in figure 7. In this report the expression magnet bar is widely used as an equivalent for magnetized resonator structure. The magnetization vector can point in any direction and may vary in magnitude for the equations in this sub section. However, in later sub sections, when specific arrangements are modeled, the magnetization is kept constant over the whole resonator structure and points in z-direction. For consistency reasons, this convention is used from here onwards.

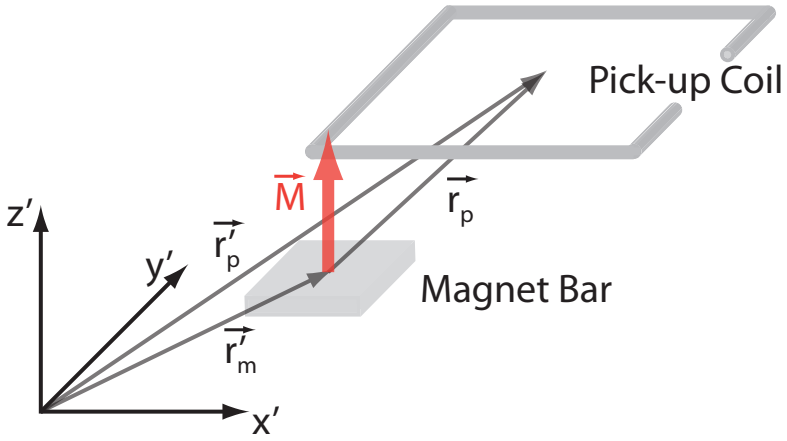

Figure 7: Schematic arrangement of pick-up coil and magnet bar.

In figure 7 $\vec{r'}_m$ denotes the center of the magnet, $\vec{r'}_p$ denotes the center of the pick-up coil and $\vec{r}_p$ denotes the center of the pick-up coil in the coordinate frame located at the center of the magnet bar. The magnet bar boundaries are identified as x'_1, x'_2, y'_1, y'_2 and the pick-up coil boundaries as $x'_{p1}, x'_{p2}, y'_{p1}, y'_{p2}$. For the further treatment of the problem it is favorable to use the coordinate frame located at the center of the magnet bar, which are the unprimed coordinates. The coordinate transformation is $\vec{r}_p = \vec{r'}_p - \vec{r'}_m$ and the vibrational velocity of the

magnet bar is transformed into a velocity of the pick-up coil: $\vec{v'}(\vec{r'}_m) = -\vec{v}(\vec{r}_p)$.

According the law of Faraday the induced voltage in the pick-up coil is given as:

$$U_p = -\frac{d}{dt}\int_S \vec{B}d\vec{S} \tag{3.26}$$

where S is the pick-up coil surface.

It is assumed that the magnet bar vibrates translationally in one direction. Any direction is possible, but rotational movements are not considered here. It follows that the pick-up coil vibrates in the transformated coordinate frame and, hence, $\vec{r}_p$ is a function of time. This allows to decompose the time derivative of equation 3.26 by applying the chain rule into:

$$\begin{aligned} U_p &= -(\frac{d\vec{r}_p}{dt}\nabla_{\vec{r}_p} + \frac{\partial}{\partial t})\int_S \vec{B}d\vec{S} && (3.27)\\ &= (\vec{v}_p\nabla_{\vec{r}_p} + \frac{\partial}{\partial t})\int_S \vec{B}d\vec{S} && (3.28)\end{aligned}$$

where $\vec{v}_p = \vec{v}(\vec{r}_p)$.

Alternatively, equation 3.26 can be developed into a Taylor progression in $\vec{r}_p$ at the coordinate $\vec{r}_p = \vec{r}_{p0}$. As mentioned above, the pick-up coil vibrates translationally and, therefore, the coordinates of the surface S change with the motion. Thus, the integral of equation 3.26 is over a non-stationary surface. It is advantageously to use relative coordinates from the pick-up coil center $\vec{r}_p$ for the integral, since the relative coordinate is constant and the deflection is only present in the center coordinate $\vec{r}_p$.

$$\vec{B}(\vec{r}) = \vec{B}(\vec{r}_p + \vec{r}_r) \tag{3.29}$$

where $\vec{r}_r$ is the relative coordinate from the pick-up coil center to the coordinate of interest.

For the given small deflections $|\Delta\vec{r}_p| << 1$, equation 3.26 developed into a

Taylor progression yields to

$$U_p = -\frac{d}{dt}\int_{S_0}\Big(\vec{B}(\vec{r}_{p0}+\vec{r}_r)+\frac{\partial\vec{B}}{\partial\vec{r}_p}\Big|_{\vec{r}_{p0}+\vec{r}_r}\Delta\vec{r}_p\Big)d\vec{S} \tag{3.30}$$

$$\tag{3.31}$$

where S_0 denotes the surface coordinates in the non deflected state. It is important to note that the integration can now be performed over a stationary surface and the deflection is considered by the multiplication with $\Delta\vec{r}_p$ in the second term. This allows also an easy interpretation of the terms, what one sees in equation 3.32.

After moving the time differentiation into the integral one obtains

$$U_p = -\int_{S_0}\frac{\partial}{\partial t}\vec{B}d\vec{S}-\int_{S_0}\Big(\frac{\partial^2\vec{B}}{\partial t\partial\vec{r}_p}\Delta\vec{r}_p+\frac{\partial\vec{B}}{\partial\vec{r}_p}\vec{v}_p\Big)d\vec{S} \tag{3.32}$$

The first term in equation 3.30 is the direct induction from the excitation and probe field without a mechanical deflection of the resonator structure. A probe field may be used to improve the detection sensitivity. The advantages will become clearer later in this section.

The last two terms in equation 3.32 generate the higher harmonic of the excitation frequency and generate the probe side band due to a mechanical resonator structure deflection. The tensor $\frac{\partial\vec{B}}{\partial\vec{r}_p}$ consists of a frequency component at the excitation frequency and at the probe frequency. The tensor is then multiplied by $\Delta\vec{r}_p$ or $\vec{v}_p$ which oscillate at the mechanical vibration frequency.

The resonator structure vibrates mechanically either with the excitation - or twice the excitation frequency or with both frequencies. This depends the DC and AC component of the resonator structure magnetization. The DC component of the magnetization causes the resonator structure to vibrate with the excitation frequency while the AC component exerts a force with twice the excitation frequency (refer to [13]). The AC component is induced by the excitation field and,

hence, the double excitation frequency component is always present. The DC component may be either induced by a DC excitation field or be present due to a remanent magnetization. One of the components may be overemphasized and be the determining force component. If one of the force frequencies coincide with the fundamental or higher order resonant frequencies of the resonator structure the deflection shows a maximum.

The exerted force on the resonator structure is according the following law:

$$\vec{F} = \mu_0 \int_V \begin{pmatrix} \frac{\partial}{\partial x}\vec{H}^T \\ \frac{\partial}{\partial y}\vec{H}^T \\ \frac{\partial}{\partial z}\vec{H}^T \end{pmatrix} \vec{M} dV \tag{3.33}$$

The subsequent derivations focus only on the probe side band voltage due to the favorable read out properties. Equation 3.32 can be re-written for the probe side band:

$$U_{SB} = U_p(\omega_p \pm \omega_m) = -\Big[\Delta\vec{r}_p(\omega_m)\frac{\partial}{\partial t} + \vec{v}_p(\omega_m)\Big] \int_{S_0} \frac{\partial \vec{B}(\omega_p)}{\partial \vec{r}} d\vec{S} \tag{3.34}$$

In equation 3.34 the derivative to $\vec{r}_p$ has been replaced by the equivalent derivative to $\vec{r}$. The following temporal relation of the flux density $\vec{B}$ and the deflection $\Delta\vec{r}_p$ are introduced:

$$\vec{B}(\vec{r}) = B_0 sin(\omega_p t)\vec{R} \tag{3.35}$$

$$\Delta\vec{r}_p = \Delta\widehat{\vec{r}}_p sin(\omega_m + \varphi_m) \tag{3.36}$$

where $\vec{R} = \frac{\vec{B}(\vec{r})}{B_0}$ is the field normalization, $B_0 = \left|\vec{B}(\vec{r}_p)\right|$, ω_m the oscillation frequency of the resonator structure deflection and φ_m the phase lag between the mechanical force exerted on the resonator structure and the mechanical deflection.

Ansatz 3.35 can be substituted into equation 3.34:

$$U_{SB} = -B_0 \Big[\Delta\vec{r}_p \omega_p cos(\omega_p t) + \vec{v}_p sin(\omega_p t) \Big] \int_{S_0} \frac{\partial \vec{R}}{\partial \vec{r}} d\vec{S} \tag{3.37}$$

and also substituting equation 3.36 into 3.37:

$$\begin{aligned} U_{SB} = -\frac{B_0 \vec{I} \Delta\widehat{\vec{r}_p}}{2} \Big[& (\omega_m - \omega_p) sin((\omega_p - \omega_m) - \varphi_m) + \\ & (\omega_m + \omega_p) sin((\omega_p + \omega_m) + \varphi_m) \Big] \end{aligned} \tag{3.38}$$

where substitution

$$\vec{I} = \int_{S_0} \frac{\partial \vec{R}}{\partial \vec{r}} d\vec{S} \tag{3.39}$$

has been used.

Equation 3.38 depicts the amplification of the probe side band amplitude by the probe frequency which is a freely selectable parameter and which can be selected adequate high. This is a favorable feature of the probe side band read out. Thereby, signal to noise ratio can be improved and the overall sensitivity is increased. The probe side band read out has been already theoretically derived and experimentally proved in the previous work [13].

In reality limitations arise from the power amplifier by the limited bandwidth and output power and the magnetization properties of the resonator structure material. For the probe field headroom in the magnetization characteristic has to be reserved, which in turn may limit the DC and excitation field.

$B_0 \vec{I} \Delta\widehat{\vec{r}_p}$ is physically interpreted as the $\Delta\phi = \phi_d - \phi_0$, which is the flux difference in the pick-up coil between the deflected and non deflected state of the resonator structure. Hence, equation 3.38 can be re-written as:

$$U_{SB} = -\frac{\Delta\phi}{2}\Big[(\omega_m - \omega_p)sin((\omega_p - \omega_m) - \varphi_m) + \tag{3.40}$$

$$(\omega_m + \omega_p)sin((\omega_p + \omega_m) + \varphi_m)\Big] \tag{3.41}$$

$\vec{I}$ is determined by the geometry and location of the pick-up coil only. The condition

$$max\{U_{SB}\} \propto max\{\Delta\vec{r}_p\vec{I}\} \tag{3.42}$$

maximizes the probe side band read out. In practical cases, the deflection direction $\Delta\vec{r}_p$ is given and the optimal pick-up coil geometry and location can be determined by maximizing 3.42. However, due to mechanical constraints in the flow channel the pick-up coil surface normal direction is given as well, which reduces condition 3.42 to $max\{\left|\vec{I}\right|\}$ in the plane of the pick up coil surface and the given deflection direction. By experience out of this project, it is most easy to plot the function $\frac{\partial\vec{R}}{\partial\vec{r}}$ and determine graphically the outline of the pick-up coil based on the graph. Some examples will follow in the next sub sections.

3.3.1 Analytical Solution for Defined Geometries and Magnetization Directions

The derivation of an analytical pick-up voltage equation for a given geometry and magnetization direction may either start with equation 3.26 or 3.28. Both equations are equivalent. Alternatively, equation 3.38 may be used, which is more straightforward and delivers directly the side band voltages. It has to be noted that equation 3.38 represents a linearization and will not consider non-linearities.

For the experimental part of this thesis the following cases have been identified:

- In-plane motion with out-plane magnetization. This corresponds typically to a magnetic polymer lateral resonator (in-plane) with no preferred magnetization axis.

- Out-plane motion with out-plane magnetization. This case refers typically to a magnetic polymer vertical resonator (out-plane) with no preferred magnetization axis.
- In-plane motion with in-plane magnetization. This corresponds typically to a ferromagnetic lateral resonator (in-plane) like cobalt-nickel with preferred in-plane magnetization axis.
- Out-plane motion with in-plane magnetization. This case refers typically to a ferromagnetic vertical resonator (out-plane) like cobalt nickel with preferred in-plane magnetization axis.

In the following sections analytical solutions for the first three cases will be worked out. There, the term magnetization refers generally only to the probe magnetization and the term pick-up voltage to the first side band amplitude. The last case is not used in the experiment.

3.3.2 Analytical Solution of the Magnetic Field

For further analytical derivations or numerical simulations the $\vec{B}$ field has to be known. The following sub section 3.4 derives an analytical model for the $\vec{B}$ field of a magnet bar. The model can be used as an input for the further analytical or numerical pathway. An advantage compared to numerical methods such as finite element method (FEM) is that the field is not only at discrete points accurately determined but continuously in space. Furthermore, the derivative field can be determined analytically and, hence, the derivative field does not suffer from potential inaccuracies as it may occur for derivatives taken from numerical FEM solutions. The implementation effort for the analytical equations in for e.g. Matlab is moderate and due these reasons it has been selected not only for the analytical pathway, but also for the numerical computizations as description for the magnetic field.

3.3.3 FEM based solution of the Magnetic Field

Alternatively, the $\vec{B}$ field can be numerically computed with for e.g. the finite element method (FEM). FEM tools like COMSOL compute the $\vec{B}$ field via the

scalar potential equation 3.15 and perform once a differentiation to compute the $\vec{B}$ field. It is crucial to select at least a quadratic or higher order Lagrange element because the determination of the pick-up voltage requires another differentiation in space. With the derivative field, equation 3.38 can be used to compute the pick-up voltage.

Another method is to compute the flux in the pick-up coil once at the deflected position and once at the non-deflected position of the resonator structure. The flux difference can then be used to compute the pick-up voltage in consideration of the vibration frequency. This method, however, delivered unreliable results for small deflections. It is assumed that the ratio mesh size to deflection should not be below a critical value.

3.4 Analytical Solution for the Magnet Bar

In the following sub section an analytical equation for the magnet bar [21] based on the charge model 3.2.4 is presented. Figure 8 illustrates the magnet bar with the coordinate system centered in the magnet bar. (x_1, x_2), (y_1, y_2) and (z_1, z_2) denote the positions of the edges of the magnet with respect to the x-, y-, and z-axis.

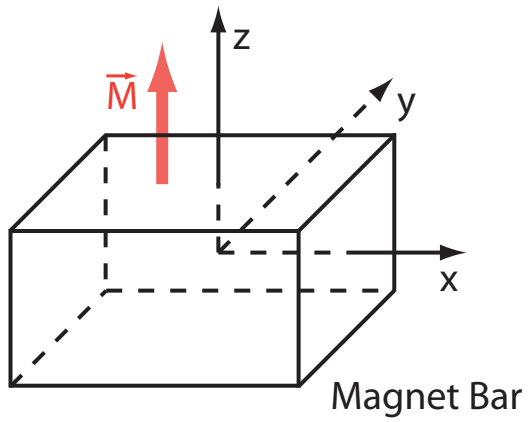

Figure 8: Magnet bar coordinate system.

The magnetization $\vec{M} = M_s\vec{e}_z$ is assumed to be uniform over the whole magnet bar and points in direction of the z-axis. First, the magnet is reduced to an equivalent charge distribution. From equation 3.23, one finds that the volume charge density is zero $\rho_m = -\nabla \cdot \vec{M} = O$. However, there is a surface charge density:

$$\sigma_m = \begin{cases} M_s & (z = z_2) \\ -M_s & (z = z_1) \end{cases}$$

The $\vec{B}$-field follows from equation 3.25:

$$\begin{aligned} \vec{B}(x,y,z) = \frac{\mu_0 M_s}{4\pi} \sum_{k=1}^{2} (-1)^k \\ \cdot \int_{y_1}^{y_2} \int_{x_1}^{x_2} \frac{[(x-x')\vec{e}_x + (y-y')\vec{e}_y + (z-z_k)\vec{e}_z]dx'dy'}{[(x-x')^2 + (y-y')^2 + (z-z_k)^2]^{3/2}} \end{aligned} \tag{3.43}$$

After integrating twice, the resulting field expression for the x-component is

$$B_x(x,y,z) = \frac{\mu_0 M_s}{4\pi} \sum_{k=1}^{2} \sum_{m=1}^{2} (-1)^{k+m} ln[F(x,y,z,x_m,y_1,y_2,z_k)] \tag{3.44}$$

where

$$F(x,y,z,x_m,y_1,y_2,z_k) = \frac{(y-y_1)+[(x-x_m)^2+(y-y_1)^2+(z-z_k)^2]^{1/2}}{(y-y_2)+[(x-x_m)^2+(y-y_2)^2+(z-z_k)^2]^{1/2}} \tag{3.45}$$

and the y-component is

$$B_y(x,y,z) = \frac{\mu_0 M_s}{4\pi} \sum_{k=1}^{2} \sum_{m=1}^{2} (-1)^{k+m} ln[H(x,y,z,x_1,x_2,y_m,z_k)] \tag{3.46}$$

where

$$H(x,y,z,x_1,x_2,y_m,z_k) = \frac{(x-x_1)+[(x-x_1)^2+(y-y_m)^2+(z-z_k)^2]^{1/2}}{(x-x_2)+[(x-x_2)^2+(y-y_m)^2+(z-z_k)^2]^{1/2}} \tag{3.47}$$

and the z-component is

$$\begin{aligned} B_z(x,y,z) = -\frac{\mu_0 M_s}{4\pi} \sum_{k=1}^{2} \sum_{n=1}^{2} \sum_{m=1}^{2} (-1)^{k+n+m} \\ \cdot arctan\Big[\frac{(x-x_n)(y-y_m)}{(z-z_k)} g(x,y,z,x_n,y_m,z_k)\Big] \end{aligned} \tag{3.48}$$

where

$$g(x, y, z, x_n, y_m, z_k) = \frac{1}{[(x - x_2)^2 + (y - y_m)^2 + (z - z_k)^2]^{1/2}} \tag{3.49}$$

3.5 In-Plane Motion and Out-Plane Magnetization

The first case, which will be analyzed deeper, is the in-plane motion with out-plane magnetization. This configuration is favorably employed to read out magnetic nano-particle polymer composite (MPC) resonators, which vibrate in lateral direction. MPC resonators have no preferred magnetization axis due to their isotropic magnetization characteristic. The pick-up coil axis is perpendicular to the plane, which means the pick-up coil surface is parallel in order to be as close as possible to the resonator structure. It is a necessity to place the pick-up coil as close as possible to the resonator structure for a successful read out. Due to the spatial constraints of the flow channel, the closest position for the pick-up coil is to place the pick-up coil surface parallel to the resonator structure plane. Figure 9 illustrates the situation. The magnet bar plane and the pick-up coil surface is parallel to the x-y plane and the magnet bar oscillates in x-direction. The coordinate system origin is selected to be in the center of the magnet bar.

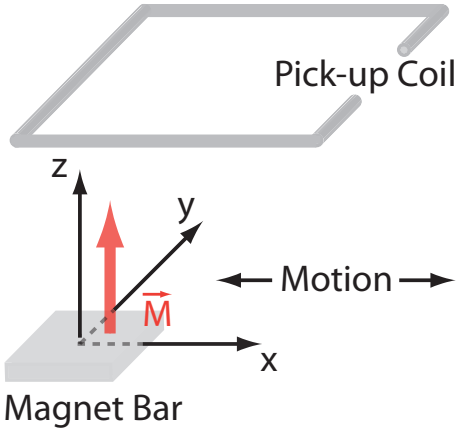

Figure 9: In-plane motion and out-plane magnetization pick-up coil and magnet bar arrangement.

3.5.1 Derivation of Analytical Approximation Function

For the described arrangement, the B_z component of the flux density field $\vec{B}$ induces a voltage in the pick-up coil and has to be known therefore. As described in section 3.3 any of the equations 3.26, 3.28, 3.38 can be used to start off with the

pick-up voltage derivation. The analytical determination of the surface integral is, however, not possible for the $\vec{B}$ field nor for the derivative $\frac{\partial \vec{B}}{\partial x}$ field. Therefore, an approximation function will be used, which is fitted to the original function by adjusting the fitting parameters. In order to find a suitable approximation function the B_z component has been plotted along an area parallel to the x-y plane at a viable distance to the magnet bar. The distance magnet bar pick-up coil is selected as $z_h = 300\,\mu\text{m}$, which suits to the current flow channel - resonator structure configuration.

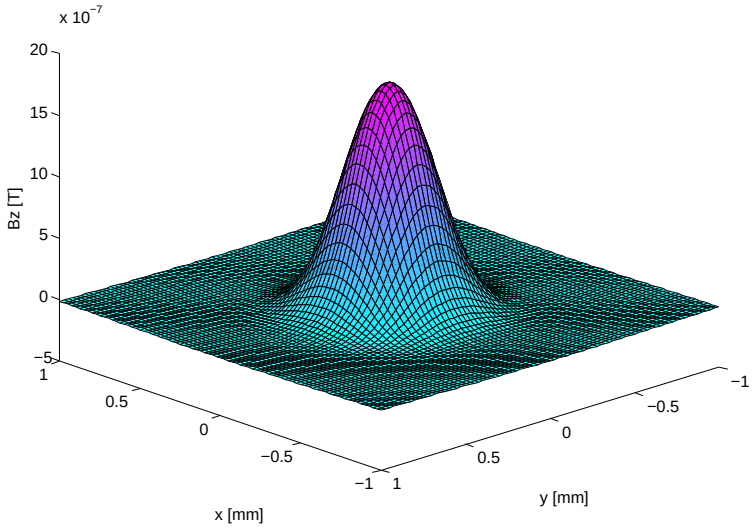

Figure 10: Field component B_z of magnet bar 400 µm x 400 µm x 2.5 µm at a distance of 300 µm with 1 kA/m magnetization.

The plot in figure 10 shows the B_z component of the $\vec{B}$ field for a representative magnet bar (400 µm x 400 µm x 2.5 µm at a distance of 300 µm) with 1 kA/m magnetization. The shape of the graph looks similar as a Gaussian distribution function 3.51 or as a Lorentzian function 3.55. Both approximation functions offer three fitting parameters. The fitting can be performed for e.g. with the least squares method, which minimizes the squared deviation:

$$min\{S\} = min\Big\{ \sum_{i}^{n} \big[B_z(i) - B_{G,z}(i)\big]^2 \Big\} \tag{3.50}$$

However, the fitting can be performed easier at dedicated coordinates like the magnet bar center and edge. This approach yields satisfactorily accurate pick-up

voltage results if the conditions later on specified in this section are met. The fitting is then performed at the center coordinate ($x = 0, y = 0$) and at the x-edge ($x_1 = -200\,\mu m$) and at the y-edge ($y_1 = -200\,\mu m$). Other fitting strategies may improve the approximation accuracy depending on the case. This should be checked per case preferably by comparing the plots. Figure 11 shows the x-view of the original function and of both approximation functions fitted to the original function 10.

The Gaussian approximation function is defined as follows

$$B_{G,z} = \quad a \cdot exp(\tfrac{x^2}{b_x} + \tfrac{y^2}{b_y}) \tag{3.51}$$

with the fitting parameters

$$a = \quad B_z(0,0,z_h) \tag{3.52}$$
$$b_x = \quad -\tfrac{x_1^2}{ln[B_z(x_1,0,z_h)/a]} \tag{3.53}$$
$$b_y = \quad -\tfrac{y_1^2}{ln[B_z(y_1,0,z_h)/a]} \tag{3.54}$$

and the Lorentzian approximation function as

$$B_{L,z} = \quad \tfrac{a}{1+\frac{x^2}{b_x}+\frac{y^2}{b_y}} \tag{3.55}$$

with the fitting parameters

$$a = \quad B_z(0,0,z_h) \tag{3.56}$$
$$b_x = \quad \tfrac{x_1^2}{a/B_z(x_1,0,z_h)-1} \tag{3.57}$$
$$b_y = \quad \tfrac{y_1^2}{a/B_z(y_1,0,z_h)-1} \tag{3.58}$$

Referring to figure 11, it is obvious that the Gaussian function possesses a very similar shape as the original function. The Lorentzian function falls off earlier than the original function close to the magnet bar center and is around the magnet bar edges $x = x_1 = -200\,\mu m$ less steep and converges slower to 0 for

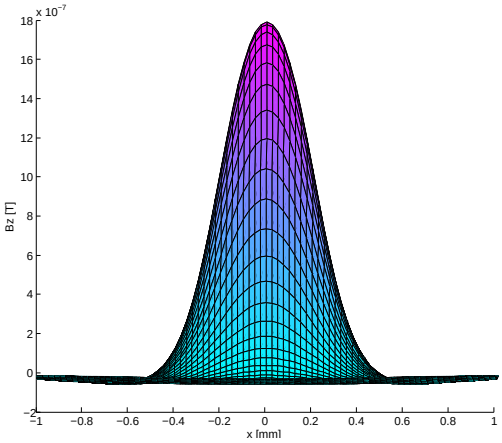

(a) Original Function

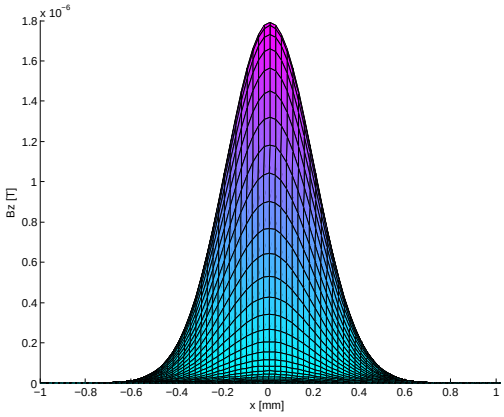

(b) Gaussian Function

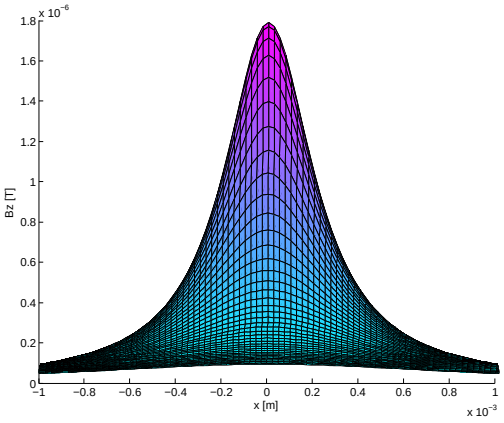

(c) Lorentzian Function

Figure 11: Approximation functions for B_z.

large x or y. Both approximation function do not turn into the negative side as the original function does for coordinates out of the magnet bar. Although the Gaussian function does not have this property, it is a good approximation of the original function, if the following conditions are met:

- One of the coil edges should be within the magnet bar boundaries.
- The deflection is small compared to the magnet bar length and width. Larger deflections increase the size of the error.
- The distance pick-up coil magnet bar is greater than half of the length or width of the magnet bar, which ever size is larger.

In this case the derivation of the pick-up voltages starts off with equation 3.26. Plugging in the pick-up coil boundaries yields

$$U_p = -\frac{d}{dt}\int_{x_{p1}}^{x_{p2}}\int_{y_{p1}}^{y_{p2}} B_{G,z}(x,y)dydx \tag{3.59}$$

One obtains after integrating twice over the boundaries of the pick-up coil

$$U_p = -\frac{d}{dt}\Big(\frac{\pi a\sqrt{b_x b_y}uv}{4}\Big) \tag{3.60}$$

with the used substitutions

$$\begin{aligned} erfd(e_1,e_2,b) &= erf(\frac{e_2}{\sqrt{b}}) - erf(\frac{e_1}{\sqrt{b}}) && (3.61)\\ u &= erfd(x_{p1},x_{p2},b_x) && (3.62)\\ v &= erfd(y_{p1},y_{p2},b_y) && (3.63)\end{aligned}$$

where $erf(x)$ means the error function with the following definition

$$erf(x) = \frac{2}{\sqrt{\pi}}\int_0^x e^{-t^2}dt \tag{3.64}$$

Based on equations 3.35 and 3.36 the temporal relation for the flux density and the deflection are as follows:

$$\begin{aligned} a &= \hat{a}sin(\omega_p t) && (3.65)\\ x_{1,2} &= x_{10,20} + \Delta\hat{x}_p sin(\omega_m t + \varphi_m) && (3.66)\\ v_x &= \frac{d}{dt}(x_{1,2}) = \omega_m\Delta\hat{x}_p cos(\omega_m t + \varphi_m) && (3.67)\end{aligned}$$

Substituting equations 3.65 into 3.60 and differentiate to the time one obtains

$$\begin{aligned} U_p =& \frac{\pi v \hat{a} \sqrt{b_x b_y}}{4} \Big\{ u \omega_p cos(\omega_p t) + \\ & \frac{2\omega_m \Delta \hat{x}_p}{\sqrt{\pi b_x}} sin(\omega_p t) cos(\omega_m t + \varphi_m) \big[e^{\frac{-x_{p2}{}^2}{b_x}} - e^{\frac{-x_{p1}{}^2}{b_x}} \big] \Big\} \end{aligned} \tag{3.68}$$

For macro-coils, if $-y_{p1}/\sqrt{b_y}, y_{p2}/\sqrt{b_y} >> 1$ and $x_{p1}/\sqrt{b_x} << -1$, equation 3.68 reduces to

$$\begin{aligned} U_p =& \frac{\pi \hat{a} \sqrt{b_x b_y}}{2} \Big\{ \omega_p cos(\omega_p t) \big[1 + erf(\frac{x_{p2}}{\sqrt{b_x}}) \big] + \\ & \frac{2\omega_m \Delta \hat{x}_p}{\sqrt{\pi b_x}} sin(\omega_p t) cos(\omega_m t + \varphi_m) e^{\frac{-x_{p2}^2}{b_x}} \Big\} \end{aligned} \tag{3.69}$$

In order to obtain the probe side band amplitude equation 3.68 is linearized at the non deflected position

$$U_{p,L}(\Delta x_p) = U_p(x_{p10}, x_{p20}) + \left. \frac{\partial U_p}{\partial x_{p1}} \right|_{x_{p10}} \Delta x_p + \left. \frac{\partial U_p}{\partial x_{p2}} \right|_{x_{p20}} \Delta x_p \tag{3.70}$$

After some mathematical manipulations one obtains

$$\begin{aligned} U_{p,L} =& \frac{\pi v \hat{a} \sqrt{b_x b_y}}{4} \Big\{ \omega_p cos(\omega_p t) \cdot erfd(x_{p10}, x_{p20}, b_x) + \frac{2\Delta \hat{x}_p}{\sqrt{\pi b_x}} \big[e^{-\frac{x_{p20}{}^2}{b_x}} - e^{-\frac{x_{p10}{}^2}{b_x}} \big] \\ & \cdot \big[\omega_p cos(\omega_p t) sin(\omega_m t + \varphi_m) + \omega_e sin(\omega_p t) cos(\omega_m t + \varphi_m) \big] \Big\} \end{aligned} \tag{3.71}$$

The probe main band term $\omega_p cos(\omega_p t) erfd(x_{10}, x_{20}, b_x)$ is removed from equation 3.71 to obtain only the side bands. It has to be noted that the main band term in equation 3.71 is not accurate enough due to the approximation.

$$U_{SB} = \frac{v\hat{a}\sqrt{\pi b_y}\Delta\hat{x}_p}{4}\left[e^{-\frac{x_{p20}{}^2}{b_x}} - e^{-\frac{x_{p10}{}^2}{b_x}}\right] \cdot \Big\{[\omega_e - \omega_p]sin((\omega_p - \omega_e)t - \varphi_m) + [\omega_e + \omega_p]sin((\omega_p + \omega_e)t + \varphi_m)\Big\} \tag{3.72}$$

Equation 3.72 simplifies for macro coils, if $-y_{p1}/\sqrt{b_y}, y_{p2}/\sqrt{b_y} >> 1$ and $x_{p1}/\sqrt{b_x} << -1$ to

$$U_{SB} = \frac{\hat{a}\sqrt{\pi b_y}\Delta\hat{x}_p}{2}e^{-\frac{x_{p20}{}^2}{b_x}} \cdot \Big\{[\omega_e - \omega_p]sin((\omega_p - \omega_e)t - \varphi_m) + [\omega_e + \omega_p]sin((\omega_p + \omega_e)t + \varphi_m)\Big\} \tag{3.73}$$

Alternatively, the side band equations 3.72, 3.73 could have been derived directly with equation 3.38. In that case the derivative field had to be approximated. However, the approximation of the magnetic flux density field $\vec{B}$ has been assessed as simpler and because of this the derivations here started with equation 3.26, although the following mathematical effort is larger. The selected Ansatz offers also the advantage that equation 3.68 considers non linearities in the magnetic field and models correctly for e.g. the case if the pick-up coil is centered above the magnet bar. If the pick-up coil is centered above the magnet bar, the flux in the pick-up coil will decrease for either motion direction. This results in a frequency doubling effect and the resulting side bands will then appear at $\omega_p - 2 * \omega_m$ and $\omega_p + 2 * \omega_m$. This effect is not considered in the linearized model, but is less important at the bottom line, since for an optimal read out the pick-up coil edge needs to be aligned at the magnet bar center.

3.5.2 Pick-up Coil Geometry and Location

In section 3.3 it has been shown that $\vec{I}$ defined in 3.39 has to be maximized to maximize the pick-up voltage. For in-plane motion in x-direction with pick-up coil in x-y plane $\vec{I}$ simplifies to

$$I = \int_{S_0} \frac{\partial R_z}{\partial x} dS \tag{3.74}$$

where

$$\begin{aligned} \frac{\partial R_z}{\partial x} =& \frac{\mu_0 M_s}{4\pi B_0} \sum_k \sum_n \sum_m \Big\{ (-1)^{k+n+m} \frac{1}{1 + (\frac{(x-x_n)(y-y_m)}{(z-z_k)} g)^2} \\ & \cdot \big[\frac{y-y_m}{z-z_k} g - \frac{(x-x_n)^2 (y-y_m)}{z-z_k} g^3 \big] \Big\} \end{aligned} \tag{3.75}$$

Function $\frac{\partial B_z}{\partial x} = B_0 \frac{\partial R_z}{\partial x}$ is plotted in figure 12 along an area for an exemplary configuration.

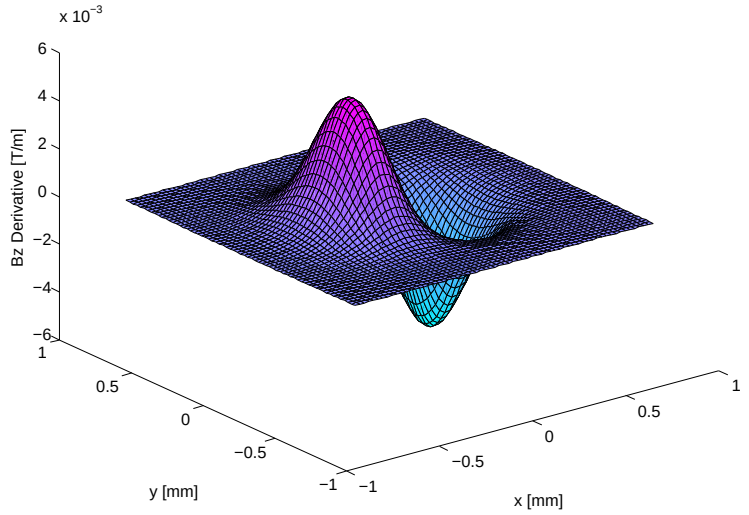

Figure 12: $\frac{\partial B_z}{\partial x}$ field of magnet bar 400 µm x 400 µm x 2.5 µm at a distance of 300 µm with 1 kA/m magnetization.

The maximization of the integral I requires to encircle either the positive or the negative mountain shown in figure 12 along a line where $\frac{\partial B_z}{\partial x} = 0$. This border line is found around the positive or negative mountain where the function becomes flat , typically at $x = \pm 500\,\mu\text{m}$, $y = \pm 500\,\mu\text{m}$ and at $x = 0$ coordinate in the shown configuration. For coordinates $x < 500\,\mu\text{m}$ the function is slightly negative and for coordinates $x > 500\,\mu\text{m}$ slightly positive. At the coordinate center, one observes that the function turns from the positive into the negative when

passing the $x = 0$ coordinate from the negative to the positive x-coordinate. This is a clear illustration that the pick-up coil should not encircle both mountains which results in a cancellation of the pick-up voltage. Preferably one edge of the pick-up coil should be aligned at the line $x = 0$. It has to be noticed that the plot of function 3.75 depends on the selected magnet bar geometry, the distance between magnet bar and pick-up coil. Hence, the optimized pick-up coil geometry depends on the magnet bar geometry and the distance magnet bar pick-up coil. However, the edge alignment of the pick-up coil at the center line $x = 0$ holds true always.

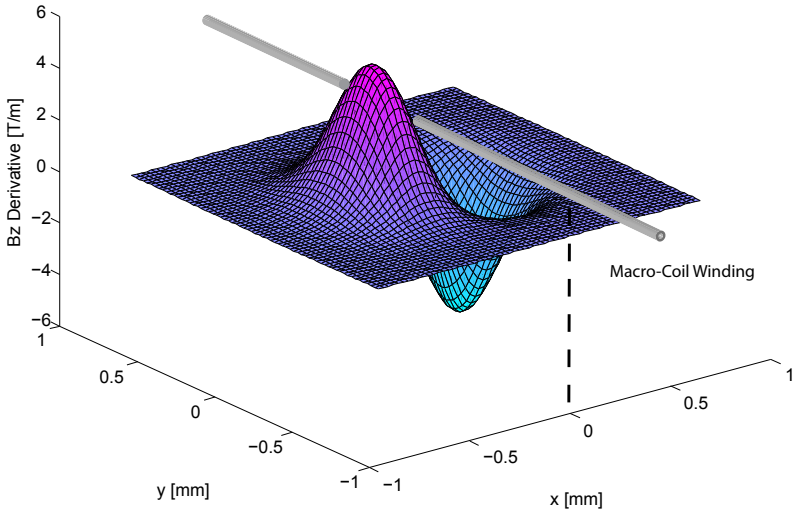

Figure 13: Macro coil alignment.

For macro sized coils the pick-up voltage is only slightly reduced when compared to μ-coils, because if for e.g. the pick-up coil covers the positive mountain of function 3.75 with edge alignment at the $x = 0$ coordinate ($x_{p2} = 0$), it will also cover a much larger area down the negative x-coordinate, but there, however, has the function 3.75 only very little negative values. Hence, one can conclude that μ-coils do not significantly outperform macro-coils. This is confirmed by figure 14 which shows the side band amplitude in variation of length and width of a rectangular pick-up coil. The maximum side band amplitude is obtained in this configuration for a length of $l_x = 600\,\mu\text{m}$ and a width of $w_y = 1100\,\mu\text{m}$ and larger sizes of pick-up coils may have only up to 20% less output voltage. Figure 14 has been numerically simulated with the original $\vec{B}$ field function 3.48

and equation 3.40.

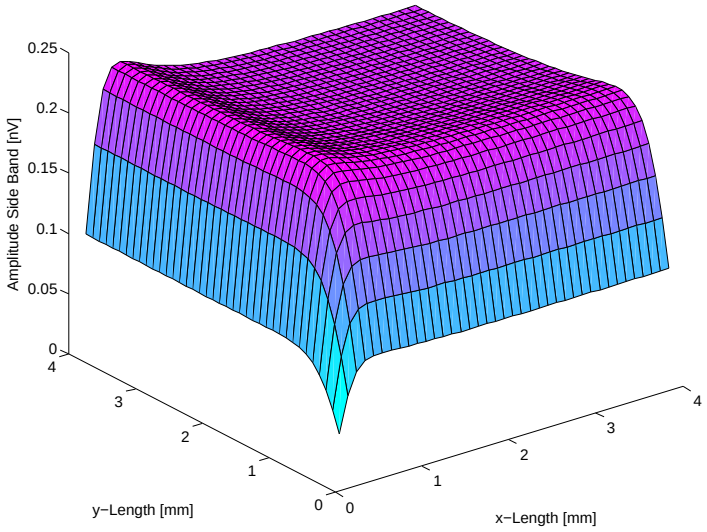

Figure 14: Side band amplitude of a rectangular pick-up coil in variation of pick-up coil length and width at a distance of $z_p = 300\,\mu\text{m}$ to a magnet bar ($400\,\mu\text{m}$ x $400\,\mu\text{m}$ x $2.5\,\mu\text{m}$). Pick-up coil is optimally aligned to magnet bar. Used parameters: magnetization $M_z = 1\,\text{kA/m}$, probe frequency $f_p = 100\,\text{kHz}$, vibration frequency $f_m = 2\,\text{kHz}$ and deflection $\Delta\hat{x}_p = 1\,\mu\text{m}$.

Figure 15(a) shows a numerical simulation of the pick-up voltage in relation to the alignment of pick-up coil. The maximum output amplitude is reached for a pick-up coil of 4 mm x 4 mm when the pick-up coil center is at $x_p = -2\,\text{mm}$, that corresponds to the alignment of the edge to the center coordinate ($x_{p2} = 0$). This observation coincides with the conclusions of equation 3.75. Figure 15(b) shows the relation of the pick-up coil voltage to the distance pick-up coil magnet bar. It is clear that a short gap between magnet bar and pick-up coil is highly desirable to increase the signal amplitude which improves the sensitivity.

3.5.3 Resonator Structure Size

Figure 16 shows the side band amplitude as a function of the resonator structure length and width. The plot shows a numerical simulation of the original $\vec{B}$ field function 3.48 and equation 3.40. By intuition, it is expected an increase in the pick-up voltage when the resonator structure size is increased, because the magnitude of the $\vec{B}$ field increases with the resonator structure size. Interesting

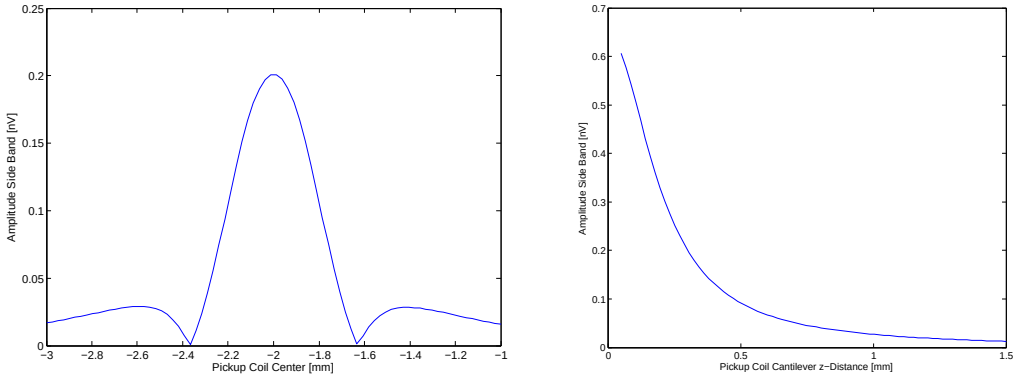

(a) Center coordinate variation (b) Distance coordinate variation

Figure 15: Side band amplitude of a rectangular pick-up coil (4 mm x 4 mm) in variation of the pick-up coil (a) center x_p coordinate ($y_p = 0\,\text{mm}$) and (b) distance coordinate z_p to a magnet bar (400 µm x 400 µm x 2.5 µm). For (a) the distance coordinate is $z_p = 300\,\mu\text{m}$ and for (b) the center coordinate is adjusted optimally to $x_p = -2\,\text{mm}$ and $y_p = 0\,\text{mm}$. Used parameters: magnetization $M_z = 1\,\text{kA/m}$, probe frequency $f_m = 100\,\text{kHz}$, vibration frequency $f_m = 2\,\text{kHz}$ and deflection $\Delta\hat{x}_p = 1\,\mu\text{m}$.

to remark is that the voltage increases fairly linear with the resonator structure width, but if the length is varied the voltages increases until to a critical length, in this case $l_x \approx 400\,\mu\text{m}$, and keeps than constant for larger lengths. The conclusion of the observation is easy and straightforward. Rectangular shapes of resonator structure with larger width should be used to optimize the pick-up voltage.

In the appendix A.1 figure 69 shows the pick-up voltage in variation of the resonator structure thickness. As expected, the side band amplitude increases linearly with the resonator structure thickness.

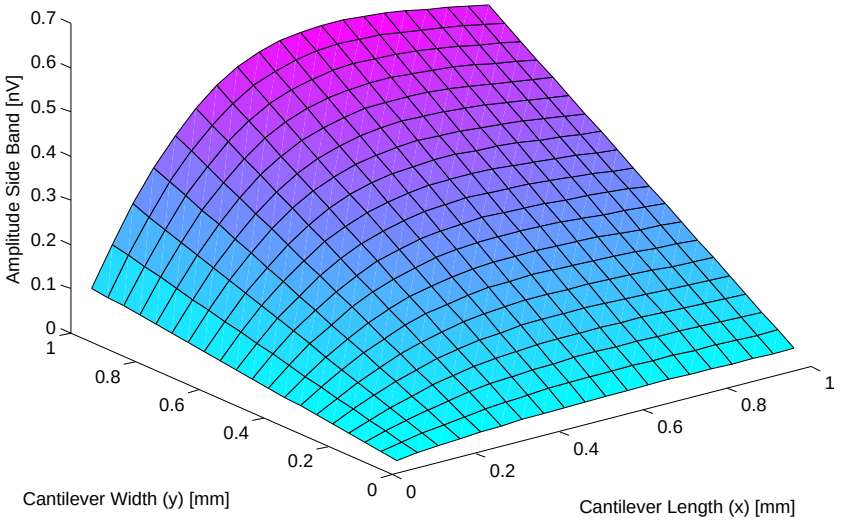

Figure 16: Side band amplitude of a rectangular pick-up coil (4 mm x 4 mm) in variation of the magnet bar length and width with a magnet bar thickness of 2.5 µm. Pick-up coil is optimally aligned to magnet bar ($x_p = -2\,\text{mm}$ and $y_p = 0\,\text{mm}$) and the distance pick-up coil magnet bar is $z_p = 300\,\mu\text{m}$. Used parameters: magnetization $M_z = 1\,\text{kA/m}$, probe frequency $f_p = 100\,\text{kHz}$, vibration frequency $f_m = 2\,\text{kHz}$ and deflection $\Delta\hat{x}_p = 1\,\mu\text{m}$.

3.5.4 Resonator Structure Array

Figure 17 illustrates a resonator structure array arrangement with the pick-up coil winding. In this case the motion is in x-direction, which is the preferred direction when the resonator structures are organized in a row. Motion in y-direction is possible as well, but is less optimal concerning the read out performance. Similar to section 3.5.2 the derivative field $\frac{\partial R_z}{\partial x}$ is used to obtain the optimal pick-up geometry and location.

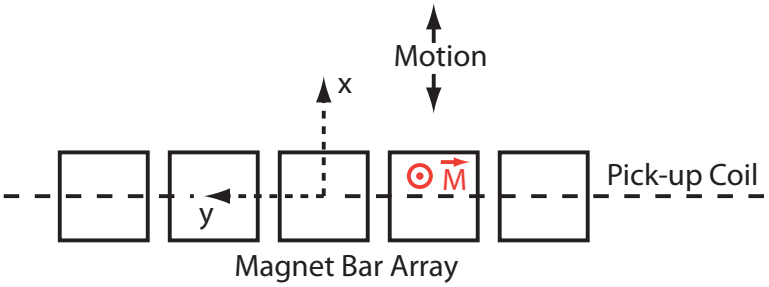

Figure 17: Resonator structure array arrangement with favorable pick-up coil alignment for in-plane motion and out-plane magnetization.

For resonator structure arrays the derivative field can be written as the superposition of the individual resonator structure derivative fields

$$\int_{S_0} \frac{\partial R_z}{\partial x} dS = \int_{S_0} \sum_C \frac{\partial R_{C,z}}{\partial x} dS = \sum_C \int_{S_0} \frac{\partial R_{C,z}}{\partial x} dS \tag{3.76}$$

and in case of constructive superposition and if the resonator structures have the same size and shape

$$\int_{S_0} \frac{\partial R_z}{\partial x} dS \approx n \int_{S_0} \frac{\partial R_{C,z}}{\partial x} dS \tag{3.77}$$

where n is the number of resonator structures.

It follows that the side band amplitude of an array is n times the side band amplitude of a single resonator structure in case of constructive superposition.

$$U_{A,SB} \approx n \cdot U_{SB} \tag{3.78}$$

Figure 18 shows the derivative field of five magnet bars. Clearly observable is the constructive superposition of the derivative field of the individual resonator structures. Constructive superposition is highly desirable to optimize the read out performance, since the total amplitude is then n times the amplitude of the single resonator structure, and the resonator structure array needs to be arranged such that the derivative field superposes constructively. Destructive superposition occurs for e.g. if the same array would deflect in y-direction (row-direction), which is obviously less optimal. At the taken distance of $z_p = 300\mu m$ one sees that the individual mountains merge into one single mountain. A macro coil, covering all mountains, performs, therefore, as good as a μ-coil. If the distance pick-up coil magnet bar is considerably decreased, the usage of a μ-coil becomes beneficial, since it can be matched to the individual mountains.

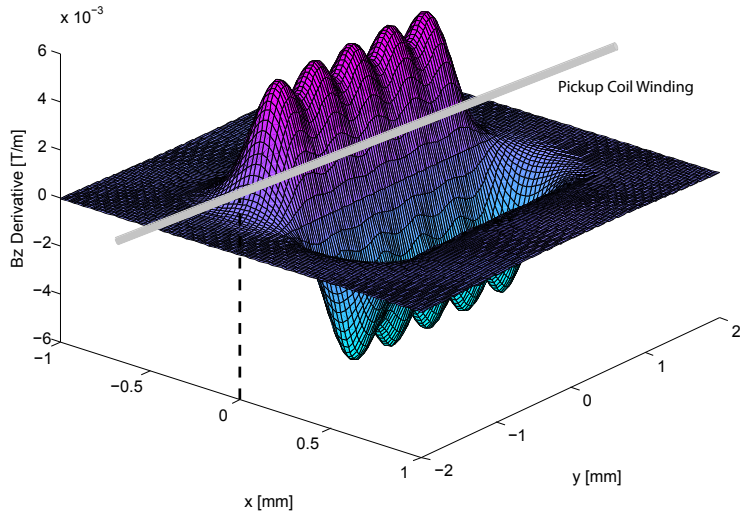

Figure 18: $\frac{\partial B_z}{\partial x}$ derivative field of five magnet bars (400 µm x 400 µm x 2.5 µm) displaced by 500 µm at a distance of 300 µm with 1 kA/m magnetization. Illustrated is also the optimal alignment of the pick-up coil winding at $x = 0$.

3.6 Out-Plane Motion and Out-Plane Magnetization

The second case is the out-plane motion with out-plane magnetization. This configuration is preferably used to read out magnetic nano-particle polymer composite (MPC) resonators, which vibrate in out-plane direction. MPC resonators have no preferred magnetization axis due to their isotropic magnetization characteristic. Like in the previous case 3.5 for lateral resonators the pick-up coil surface is parallel to the x-y plane in order to be as close as possible to the resonator structure. Figure 19 illustrates the situation. As a difference to the previous case the magnet bar oscillates in z-direction. The coordinate system origin is selected to be in the center of the magnet bar for all plots and function definitions in this section.

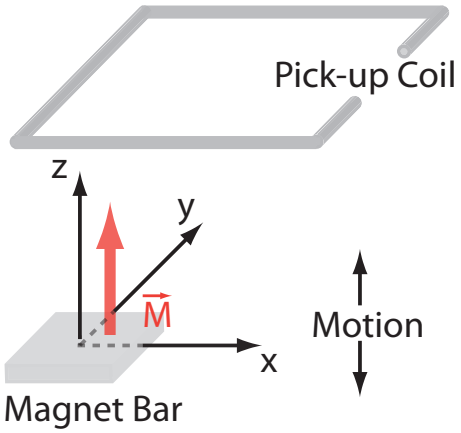

Figure 19: Out-plane motion and out-plane magnetization pick-up coil and magnet bar arrangement.

3.6.1 Derivation of Analytical Approximation Function

The derivation starts off with Ansatz 3.38. For out-plane motion and out-plane magnetization $\vec{I}$ reduces to

$$I = \int_{S_0} \frac{\partial R_z}{\partial z} dS \tag{3.79}$$

where

$$\frac{\partial R_z}{\partial z} = -\frac{\mu_0 M_s}{4\pi B_0} \sum_k \sum_n \sum_m \Big\{ (-1)^{k+n+m} \frac{1}{1 + (\frac{(x-x_n)(y-y_m)}{(z-z_k)} g)^2} \cdot \Big[\frac{(x-x_n)(y-y_m)}{(z-z_k)^2} g + (x-x_n)(y-y_m) g^3 \Big] \Big\} \tag{3.80}$$

Function 3.80 is, however, analytically not integrable. The procedure is now the same as in the previous section. The derivative field 3.80 is plotted along a surface parallel to the x-y plane for a representative size of magnet bar and at a viable distance to the magnet bar. Figure 20 shows the plot of the derivative field.

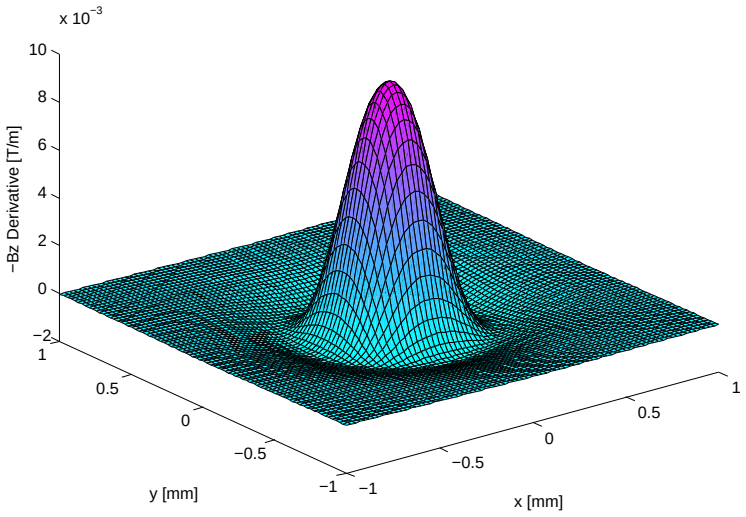

Figure 20: $-\frac{\partial B_z}{\partial z}$ field of magnet bar 400 µm x 400 µm x 2.5 µm at a distance of 300 µm with 1 kA/m magnetization.

Again the graph possesses a Gaussian similar shape, but the function turns also into the negative side for $r > \sqrt{(}x_1^2 + y_1^2)$ before it converges slowly to zero for large coordinates.

The following function γ is proposed as approximation. It includes a Gaussian function with a turn into the negative side before converging to zero

$$\gamma = a \left(\epsilon - \frac{x^2}{b_x} - \frac{y^2}{b_y} \right) e^{-\frac{x^2}{b_x} - \frac{y^2}{b_y}} \tag{3.81}$$

Integrated over the rectangular surface of the pick-up coil with boundaries x_{p1}, x_{p2}, y_{p1} and y_{p2} yields

$$\begin{aligned}\int_{x_{p1}}^{x_{p2}} \int_{y_{p1}}^{y_{p2}} \gamma dydx =& \frac{\sqrt{\pi}a}{4}\Big\{ v\sqrt{b_y}\big(x_{p1}e^{-\frac{{x_{p1}}^2}{b_x}} - x_{p2}e^{-\frac{{x_{p2}}^2}{b_x}}\big) \\ &+ u\sqrt{b_x}\big[(\epsilon-1)v\sqrt{\pi b_y} + y_{p1}e^{-\frac{{y_{p1}}^2}{b_y}} - y_{p2}e^{-\frac{{y_{p2}}^2}{b_y}}\big]\Big\}\end{aligned} \tag{3.82}$$

If the pick-up coil is large ($-x_{p1}, x_{p2}, -y_{p1}, y_{p2} \to \infty$) the pick-up voltage has to converge to zero. This physical condition demands that

$$\int_{-\infty}^{\infty} \int_{-\infty}^{\infty} \gamma dydx = 0 \tag{3.83}$$

which requires $\epsilon = 1$.

The approximation function 3.81 becomes then

$$\gamma = a\left(1 - \frac{x^2}{b_x} - \frac{y^2}{b_y}\right) e^{-\frac{x^2}{b_x}-\frac{y^2}{b_y}} \tag{3.84}$$

and equation 3.82

$$\int_{x_{p1}}^{x_{p2}} \int_{y_{p1}}^{y_{p2}} \gamma dydx = \frac{\sqrt{\pi}a}{4} v\sqrt{b_y}\big(x_{p1}e^{-\frac{{x_{p1}}^2}{b_x}} - x_{p2}e^{-\frac{{x_{p2}}^2}{b_x}}\big) \tag{3.85}$$

Function 3.84 has three parameters left which can be used for the fitting to the original function 3.80. Again, the fitting could be performed for e.g. with the least squares method, but if the approximation function is fitted at the magnet bar coordinates, the result is satisfactory. Other fitting strategies may improve the approximation quality depending on the configuration. This should be checked per case preferably by comparing the plots. The fitting equations are as follows

$$\frac{\partial B_z}{\partial z}(x=0, y=0) = \gamma(0,0) = a \tag{3.86}$$

$$\frac{\partial B_z}{\partial z}(x=x_1, y=0) = \gamma(x_1,0) = a\Big(1 - \frac{{x_1}^2}{b_x}\Big)e^{-\frac{{x_1}^2}{b_x}} \tag{3.87}$$

$$\frac{\partial B_z}{\partial z}(x=0, y=y_1) = \gamma(0,y_1) = a\Big(1 - \frac{{y_1}^2}{b_y}\Big)e^{-\frac{{y_1}^2}{b_y}} \tag{3.88}$$

b_x 3.87 and b_y 3.88 have to be determined by an iterative nonlinear solver, since the equation is implicit.

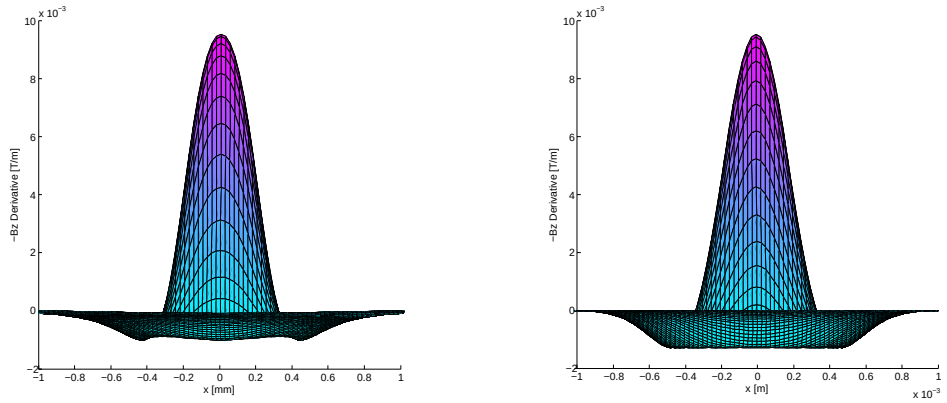

(a) Original Function (b) γ-Approximation Function

Figure 21: Side view of derivative field $\frac{\partial B_z}{\partial z}$ and of fitted γ-approximation function.

Figure 21 shows the original function $\frac{\partial B_z}{\partial z}$ and the fitted γ-approximation function. The turn into the negative side is stronger emphasized in the approximation function than in the original function. Nevertheless, in a number of comparisons with numerical simulations it turned out that the proposed γ-function is a satisfying approximation of the original function for the purpose of computing the pick-up voltage. The following conditions should be met:

- One of the coil edge should be within the magnet bar boundaries.
- The deflection is small compared to the magnet bar length and width. Larger deflections increase the size of the error.
- The distance pick-up coil magnet bar is greater than half of the length or width of the magnet bar, which ever size is larger.

In order to obtain the final analytical approximative side band amplitude function 3.89 equation 3.85 is substituted into equation 3.38.

$$U_{SB} = \frac{\sqrt{\pi}a\Delta\hat{z}_p}{8}\Big\{v\sqrt{b_y}\big(x_{p2}e^{-\frac{{x_{p2}}^2}{b_x}} - x_{p1}e^{-\frac{{x_{p1}}^2}{b_x}}\big) + u\sqrt{b_x}\big(y_{p2}e^{-\frac{{y_{p2}}^2}{b_y}} - y_{p1}e^{-\frac{{y_{p1}}^2}{b_y}}\big)\Big\} \cdot \Big[(\omega_m - \omega_p)sin((\omega_p - \omega_m) - \varphi_m) + (\omega_m + \omega_p)sin((\omega_p + \omega_m) + \varphi_m)\Big] \tag{3.89}$$

For large coils $-x_{p1}, -y_{p1}, y_{p2} >> 1$ expression 3.89 can be reduced to

$$U_{SB} = \frac{\sqrt{\pi b_y}a\Delta\hat{z}_p}{4}\big(x_{p2}e^{-\frac{{x_{p2}}^2}{b_x}}\big) \cdot \Big[(\omega_m - \omega_p)sin((\omega_p - \omega_m) - \varphi_m) + (\omega_m + \omega_p)sin((\omega_p + \omega_m) + \varphi_m)\Big] \tag{3.90}$$

3.6.2 Pick-up Coil Geometry and Location

Condition 3.42 maximizes the probe side band read out. For out-plane motion in z-direction with pick-up coil in x-y plane $\vec{I}$ simplifies to equation 3.79. Plugging in the γ-approximation function yields

$$max\{I\} = max\{\int \gamma\} = max\{\int a\left(1 - \frac{x^2}{b_x} - \frac{y^2}{b_y}\right)e^{-\frac{x^2}{b_x}-\frac{y^2}{b_y}}\} \tag{3.91}$$

Equation 3.91 maximizes if the integration is performed over a surface where the integrand is only positive. This surface is defined by the ellipsoid function in the first term of the integrand of 3.91.

$$\frac{x^2}{b_x} + \frac{y^2}{b_y} = 1 \tag{3.92}$$

Based on the γ-approximation function the optimal shape for the pick-up coil is an ellipsoid centered at the coordinate center with the half-radii $\sqrt{b_x}$ and $\sqrt{b_y}$.

Alternatively, the optimal shape can be determined by plotting $\frac{\partial R_z}{\partial z}$, which uses the original function and, hence, is more accurate than the Ansatz with the

γ-approximation function. Figure 20 shows graphically the mentioned derivative field. The maximization of the integral I requires to encircle the positive mountain along a border line where $\frac{\partial B_z}{\partial z} = 0$. In this case with the selected quadratic magnet bar dimensions, this is a circle with radius $r \approx 300\,\mu\text{m}$. For macro sized coils, it is important to have one edge of the pick-up coil aligned with the zero crossing of the derivative field in order to avoid the cancellation of the flux in the pick-up coil. Refer to figure 22. Macro coils encircling the positive mountain in a broad manner have no magnetic flux pick-up and the induced pick-up voltage is zero.

It shall be noted that the graph of the derivative field 20 depends on the selected magnet bar geometry and the distance between magnet bar and pick-up coil. Therefore, the optimized pick-up coil geometry depends on the magnet bar geometry and the distance magnet bar pick-up coil. However, the edge alignment of the pick-up coil at the zero crossing line $\frac{\partial R_z}{\partial z} = 0$ is always valid.

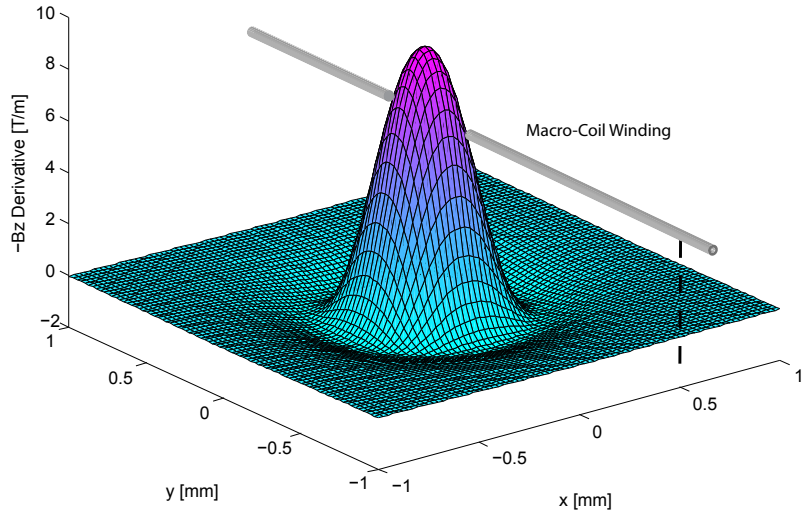

Figure 22: Macro coil alignment.

Figure 23 shows the side band amplitude in variation of length and width of a rectangular pick-up coil with proper edge alignment for a representative configuration. Macro coils have a pick-up voltage of about 35% of the maximal value which is obtained for the optimal rectangular μ-coil. Hence, the output voltage is lower for the macro-coil, but again like in the in-plane motion and out-plane

magnetization case the performance gain of the μ-coil is not so significant. Figure 23 has been numerically simulated with the original $\vec{B}$ field function 3.48 and equation 3.40.

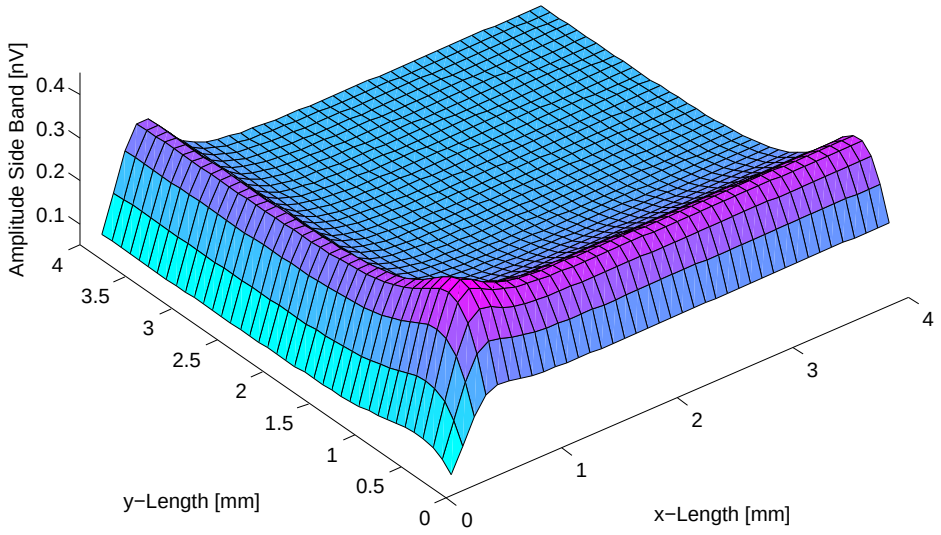

Figure 23: Side band amplitude of a rectangular pick-up coil in variation of pick-up coil length and width at a distance of $z_p = 300\,\mu\text{m}$ to a magnet bar ($400\,\mu\text{m}$ x $400\,\mu\text{m}$ x $2.5\,\mu\text{m}$). Pick-up coil is optimally aligned to magnet bar. Used parameters: magnetization $M_z = 1\,\text{kA/m}$, probe frequency $f_p = 100\,\text{kHz}$, vibration frequency $f_m = 2\,\text{kHz}$ and deflection $\Delta\hat{z}_p = 1\,\mu\text{m}$.

Figure 24(a) shows a numerical simulation of the pick-up voltage in relation to the alignment of the macro pick-up coil. The maximum output amplitude is reached pick-up coil edge x_{p2} is aligned to the zero crossing of the derivative field on the positive x-coordinate. In the shown configuration the coil center is then at $x_p = -1.753\,\text{mm}$. This is in good agreement with the conclusion of the ellipsoid function 3.92 and the observation of the derivative field in figure 20. Figure 24(b) illustrates the relation of pick-up voltage and distance pick-up coil to magnet bar. It is intuitive, that decreasing the distance increases the pick-up voltage and improves the read out sensitivity.

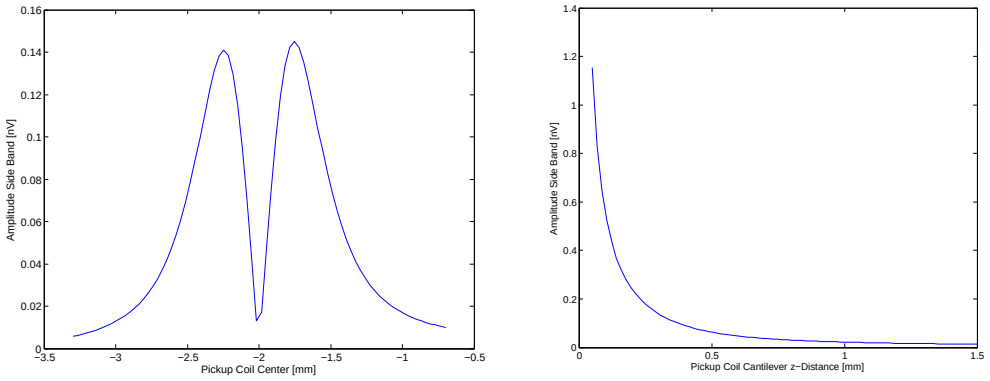

(a) Center coordinate variation (b) Distance coordinate variation

Figure 24: Side band amplitude of a rectangular pick-up coil (4 mm x 4 mm) in variation of the pick-up coil (a) center x_p coordinate ($y_p = 0\,\text{mm}$) and (b) distance coordinate z_p to a magnet bar (400 µm x 400 µm x 2.5 µm). For (a) the distance coordinate is $z_p = 300\,\mu\text{m}$ and for (b) the center coordinate x_p is adjusted optimally depending on the distance coordinate z_p and $y_p = 0\,\text{mm}$. Used parameters: magnetization $M_z = 1\,\text{kA/m}$, probe frequency $f_m = 100\,\text{kHz}$, vibration frequency $f_m = 2\,\text{kHz}$ and deflection $\Delta\hat{x}_p = 1\,\mu\text{m}$.

3.6.3 Resonator Structure Size

Figure 25 shows the side band amplitude as a function of the resonator structure length and width. The plot shows a numerical simulation of the original $\vec{B}$ field function 3.48 and equation 3.40. The same comment apply here as in the case of in-plane motion and out-plane magnetization. It is intuitively expected that the pick-up voltage is increased when the resonator structure size is increased, because the magnitude of the $\vec{B}$ field increases with the resonator structure size. While the pick-up voltage increases fairly linear with the resonator structure width the variation of the length increases the voltage until to a critical length and from there the voltage keeps constant for larger lengths.

In the appendix A.1 figure 70 shows the pick-up voltage in variation of the resonator structure thickness. As expected by intuition, the side band amplitude increases linearly with the resonator structure thickness.

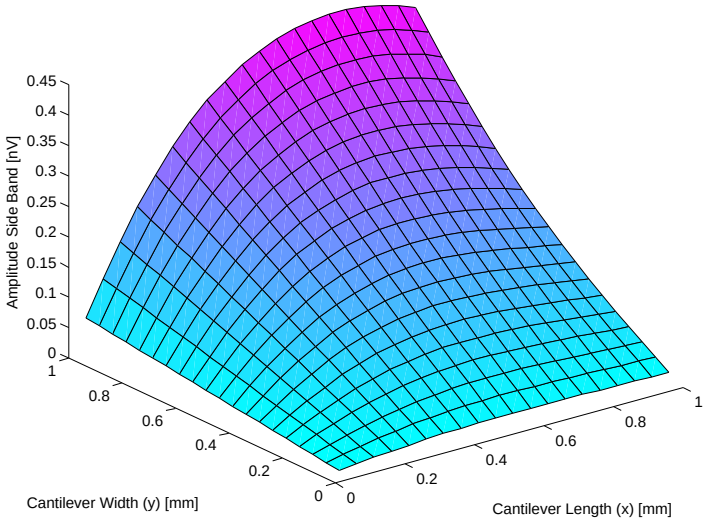

Figure 25: Side band amplitude of a rectangular pick-up coil (4 mm x 4 mm) in variation of the magnet bar length and width with a magnet bar thickness of 2.5 µm. Pick-up coil is optimally aligned to magnet bar and the distance pick-up coil magnet bar is $z_p = 300\,\mu\text{m}$. Used parameters: $M_z = 1\,\text{kA/m}$, probe frequency $f_m = 100\,\text{kHz}$, vibration frequency $f_m = 2\,\text{kHz}$ and deflection $\Delta\hat{x}_p = 1\,\mu\text{m}$.

3.6.4 Resonator Structure Array

Figure 26 shows the resonator structure array arrangement with the pick-up coil winding. Like in section 3.6.2 the derivative field $\frac{\partial R_z}{\partial z}$ is used to determine the optimal pick-up geometry and location.

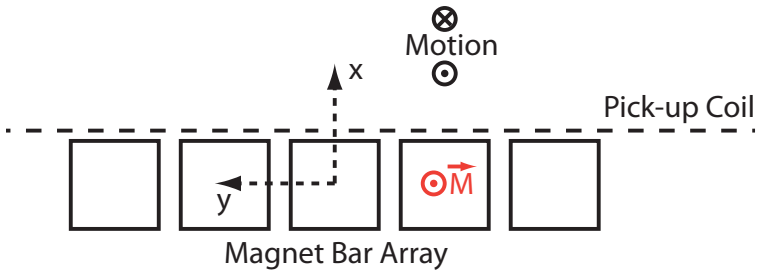

Figure 26: Resonator structure array arrangement with favorable pick-up coil alignment for out-plane motion and out-plane magnetization.

In this case the results of equation 3.77, derived in section in-plane motion with out-plane magnetization, hold true as well. For constructive superposition the total side band amplitude is equal to n times the amplitude of the individual resonator structure. It is assumed that all resonator structures have the same size and shape.

Figure 27 shows the constructive superposition of the individual resonator structure derivative fields. It is clear from the previous case that constructive superposition is important to obtain an optimal read out performance. The resonator structures can be in this case of out-plane motion organized either as a row (y-direction) or as a column (x-direction) to receive constructive superposition. At the taken distance of $z_p = 300\,\mu\text{m}$ one sees that the individual mountains merge into one single mountain. A macro coil, covering all mountains, performs, therefore, as good as a μ-coil. For distances significantly lower, the μ-coil outperforms the macro coil because the μ-coil can be designed to pick-up the individual mountains.

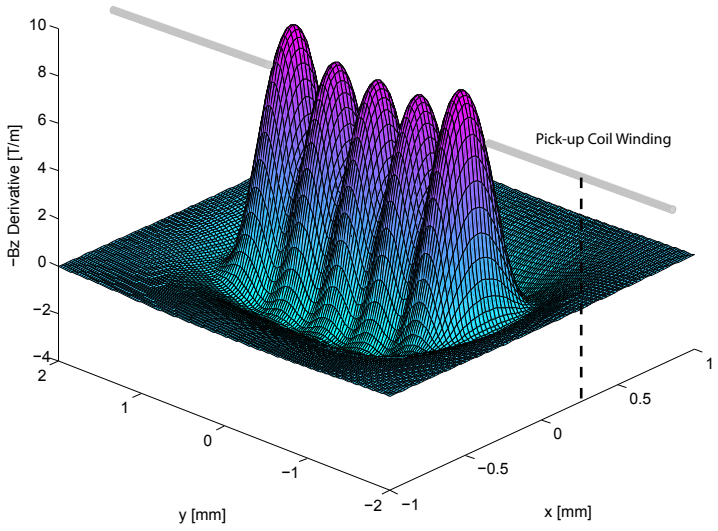

Figure 27: $-\frac{\partial B_z}{\partial z}$ derivative field of five magnet bars (400 µm x 400 µm x 2.5 µm) displaced by 500 µm at a distance of 300 µm with 1 kA/m magnetization. Illustrated is also the optimal alignment of the pick-up coil winding at $x \approx x_2$.

3.7 In-Plane Motion and In-Plane Magnetization

The third case is the in-plane motion with in-plane magnetization. This case corresponds to a lateral resonator with in-plane probe magnetization. In-plane magnetization is particularly interesting if the resonator structure consists of ferromagnetic material like for e.g. cobalt-nickel, which are magnetized much easier in-plane than out-plane and, thus, posses a preferred magnetization direction. Like in the previous cases the pick-up coil surface is arranged parallel to the magnet bar plane in order to be as close as possible to the resonator structure. Note, the magnet bar and pick-up coil arrangement has been rotated by 90^0 to maintain the magnetization in z-direction. Figure 28 illustrates the situation. The magnet bar oscillates in z-direction and the coordinate system origin is selected to be in the center of the magnet bar for all plots and function definitions in this section.

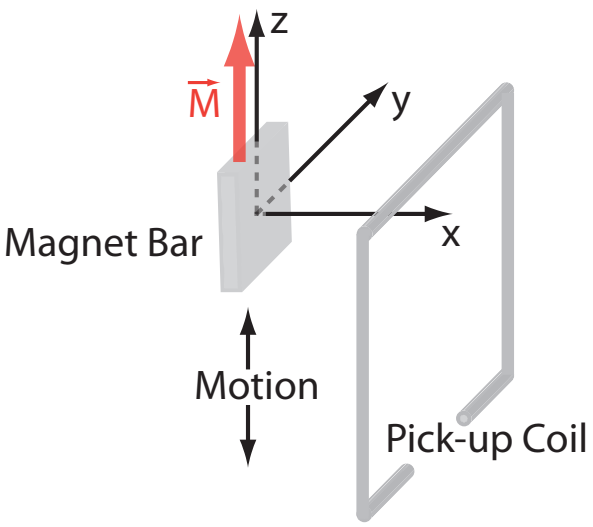

Figure 28: In-plane motion and in-plane magnetization pick-up coil and magnet bar arrangement.

3.7.1 Derivation of Analytical Approximation Function

The derivation starts off with Ansatz 3.38. For in-plane motion and in-plane magnetization $\vec{I}$ reduces to

$$I = \int_{S_0} \frac{\partial R_x}{\partial z} dS \tag{3.93}$$

where

$$\frac{\partial R_x}{\partial z} = \frac{\mu_0 M_s}{4\pi B_0} \sum_k \sum_m \left\{ (-1)^{k+m} \frac{(z - z_k)\left[\frac{1}{\beta_1}(y - y_2 + \beta_2) - \frac{1}{\beta_2}(y - y_1 + \beta_1)\right]}{(y - y_2 + \beta_2)(y - y_1 + \beta_1)} \right\} \tag{3.94}$$

by using the substitutions

$$\beta_1 = \left[(x - x_m)^2 + (y - y_1)^2 + (z - z_k)^2\right]^{\frac{1}{2}} \tag{3.95}$$

$$\beta_2 = \left[(x - x_m)^2 + (y - y_2)^2 + (z - z_k)^2\right]^{\frac{1}{2}} \tag{3.96}$$

Function 3.94 is also analytically not integrable like the derivative fields from the previous sections. The procedure is as already presented. The derivative field 3.94 is plotted along a surface parallel to the y-z plane for a representative size of magnet bar and at a viable distance to the magnet bar. Figure 29 shows the graph of the derivative field.

Once again the graph possesses a Gaussian similar shape and the function turns at this time only along the z-coordinate direction into the negative side for $z < z_1$ or $z > z_2$ before it converges slowly to zero for large coordinates.

Function 3.94 can be approximated by the following function

$$\lambda = a \left(\epsilon - \frac{z^2}{b_z}\right) e^{-\frac{y^2}{b_y} - \frac{z^2}{b_z}} \tag{3.97}$$

Integrating over the rectangular surface of the pick-up coil with boundaries x_{p1}, x_{p2}, y_{p1} and y_{p2} yields

$$\int_{y_{p1}}^{y_{p2}} \int_{z_{p1}}^{z_{p2}} \lambda dz dy = \frac{\sqrt{\pi b_y} a v}{8} \left\{ (2\epsilon - 1)\sqrt{\pi b_z} w + 2 z_{p2} e^{-\frac{{z_{p2}}^2}{b_z}} - 2 z_{p1} e^{-\frac{{z_{p1}}^2}{b_z}} \right\} \tag{3.98}$$

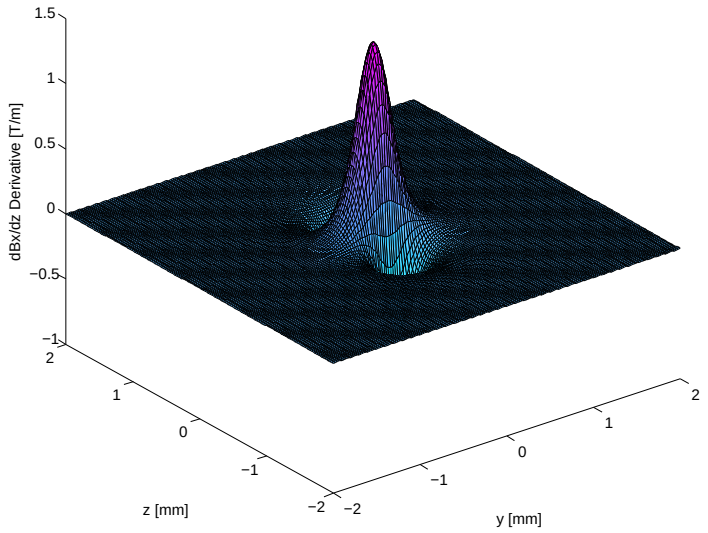

Figure 29: $\frac{\partial B_x}{\partial z}$ field of magnet bar 400 µm x 400 µm x 2.5 µm at a distance of 300 µm with 1 kA/m magnetization.

with the used substitution

$$w = erf(\frac{z_{p2}}{\sqrt{b_z}}) - erf(\frac{z_{p1}}{\sqrt{b_z}}) \tag{3.99}$$

For infinite large pick-up coils ($-x_{p1}, x_{p2}, -y_{p1}, y_{p2} \to \infty$) the pick-up voltage has to converge to zero. This physical condition demands that

$$\int_{-\infty}^{\infty}\int_{-\infty}^{\infty} \lambda dz dy = 0 \tag{3.100}$$

which requires $\epsilon = \frac{1}{2}$.

This yields to the updated approximation function

$$\lambda = a\left(\frac{1}{2} - \frac{z^2}{b_z}\right) e^{-\frac{y^2}{b_y} - \frac{z^2}{b_z}} \tag{3.101}$$

and equation 3.98 can be rewritten as

$$\int_{y_{p1}}^{y_{p2}}\int_{z_{p1}}^{z_{p2}} \lambda dz dy = \frac{\sqrt{\pi b_y} av}{4}\left\{ z_{p2} e^{-\frac{{z_{p2}}^2}{b_z}} - z_{p1} e^{-\frac{{z_{p1}}^2}{b_z}} \right\} \tag{3.102}$$

Function 3.102 offers two fitting parameters for the adjustment to the original

function 3.94. The fitting is performed at the center and at the z-edge z_1 of the magnet bar. Other fitting strategies may improve the approximation quality depending on the configuration. This should be checked per case preferably by comparing the plots. The fitting equations are as follows

$$\frac{\partial B_x}{\partial z}(y=0, z=0) = \lambda(0,0) = a \tag{3.103}$$

$$\frac{\partial B_x}{\partial z}(y=0, z=z_1) = \lambda(0,z_1) = a\Big(\frac{1}{2} - \frac{{z_1}^2}{b_z}\Big)e^{-\frac{{z_1}^2}{b_z}} \tag{3.104}$$

Equation 3.104 is implicit and b_z has to be numerically evaluated by an iterative non-linear solver.

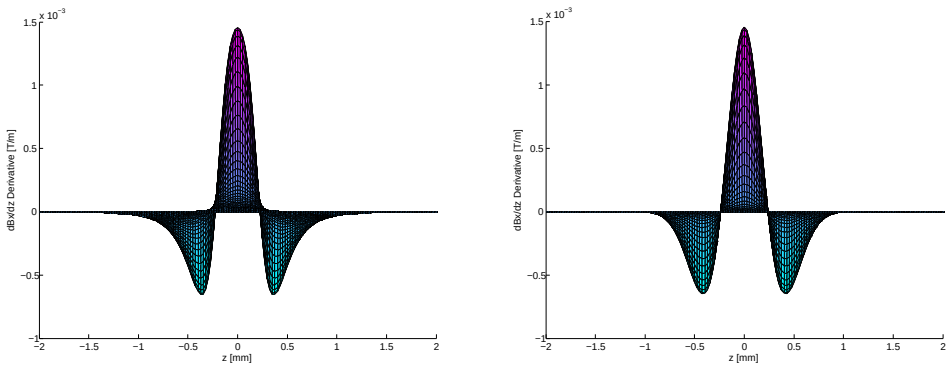

(a) Original Function (b) λ-Approximation Function

Figure 30: Side view of derivative field $\frac{\partial B_x}{\partial z}$ and of fitted λ-approximation function.

Figure 30 shows the original function $\frac{\partial B_z}{\partial z}$ and the fitted λ-approximation function. There is a good agreement between the approximation and the original function. However, it is recommended to meet the following conditions:

- One of the coil edges should be within the magnet bar boundaries.
- The deflection is small compared to the magnet bar length and width. Larger deflections increase the size of the error.
- The distance pick-up coil magnet bar is greater than half of the length or width of the magnet bar, which ever size is larger.

- The fitting of the approximation function at the magnet bar center and edge is recommended. However, other fitting points are possible and may improve the approximation depending on the case. This should be checked per case preferably by comparing the plots.

One obtains the final analytical approximative side band amplitude equation 3.105 by substituting equation 3.101 into equation 3.38.

$$U_{SB} = -\frac{\sqrt{\pi b_y} a v \Delta \hat{z}_p}{8} \Big\{ z_{p2} e^{-\frac{{z_{p2}}^2}{b_z}} - z_{p1} e^{-\frac{{z_{p1}}^2}{b_z}} \Big\} \cdot \Big[(\omega_m - \omega_p) sin((\omega_p - \omega_m) - \varphi_m) + (\omega_m + \omega_p) sin((\omega_p + \omega_m) + \varphi_m) \Big] \tag{3.105}$$

For macro coils $-y_{p1}, y_{p2}, -z_{p1} >> 1$ expression 3.105 can be simplified to

$$U_{SB} = -\frac{\sqrt{\pi b_y} a \Delta \hat{z}_p}{4} \Big\{ z_{p2} e^{-\frac{{z_{p2}}^2}{b_z}} \Big\} \cdot \Big[(\omega_m - \omega_p) sin((\omega_p - \omega_m) - \varphi_m) + (\omega_m + \omega_p) sin((\omega_p + \omega_m) + \varphi_m) \Big] \tag{3.106}$$

3.7.2 Pick-up Coil Geometry and Location

Condition 3.42 maximizes the probe side band read out. For in-plane motion in z-direction with pick-up coil in y-z plane $\vec{I}$ simplifies to equation 3.93. Substituting in the λ-approximation function yields

$$max\{I\} = max\{ \int \lambda \} = max\{ \int a \left(\frac{1}{2} - \frac{z^2}{b_z} \right) e^{-\frac{y^2}{b_y} - \frac{z^2}{b_z}} \} \tag{3.107}$$

Above expression 3.107 is maximized by a surface bordered by the z-coordinate which is defined by the first term in the integrand and by the y-coordinate which takes values from $-\infty .. + \infty$. The first term in the integrand equals to zero at the border and defines the z-coordinate.

$$z^2 = \frac{b_z}{2} \tag{3.108}$$

$$z_{p1} = -\sqrt{\frac{b_z}{2}} \tag{3.109}$$

$$z_{p2} = \sqrt{\frac{b_z}{2}} \tag{3.110}$$

$$y_{p1} \to -\infty \tag{3.111}$$

$$y_{p2} \to \infty \tag{3.112}$$

The maximizing rectangular pick-up coil is centered at the coordinate origin with finite z-coordinate boundaries and infinite y-coordinate boundaries.

The same result can be obtained by taking the gradient from the side band amplitude function U_{SB} and solve the equation set 3.113 to get the boundaries of the maximizing rectangular pick-up coil.

$$\begin{pmatrix} \frac{\partial}{\partial y_{p1}} \\ \frac{\partial}{\partial y_{p2}} \\ \frac{\partial}{\partial z_{p1}} \\ \frac{\partial}{\partial z_{p2}} \end{pmatrix} U_{SB} = \vec{0} \tag{3.113}$$

As an alternative, the optimal shape can be determined by plotting $\frac{\partial R_x}{\partial z}$, which uses the original function and, hence, is more accurate than the approximation with the λ-function. Figure 29 shows graphically the mentioned derivative field. The maximization of the integral I requires to encircle the positive mountain along a line where $\frac{\partial R_x}{\partial z} = 0$. In this case of in-plane motion and out-plane magnetization the encircling line is split into two lines, which travel from $-\infty$ to $+\infty$ for the y-coordinate and the z-coordinate is selected such that the derivative function equals to zero. Both lines are symmetric to the z-coordinate axis. They pass by between the positive and negative mountain for small y-coordinates and are forced apart for coordinates at a large distance.

Macro coils should be edge aligned at the $\frac{\partial R_x}{\partial z} = 0$ line between the positive

and negative mountain. Either of the two negative mountains is encircled by the macro coil, but it has to be avoided to encircle both negative mountains resulting in a cancellation of the pick-up voltage. Refer to figure 31.

It can be noticed that the graph of the derivative field (figure 29) depends on the selected magnet bar geometry and the distance between magnet bar and pick-up coil. Therefore, the optimized pick-up coil geometry depends on the magnet bar geometry and the distance magnet bar pick-up coil. However, the edge alignment of the pick-up coil at the zero crossing line $\frac{\partial R_z}{\partial z} = 0$ is always valid.

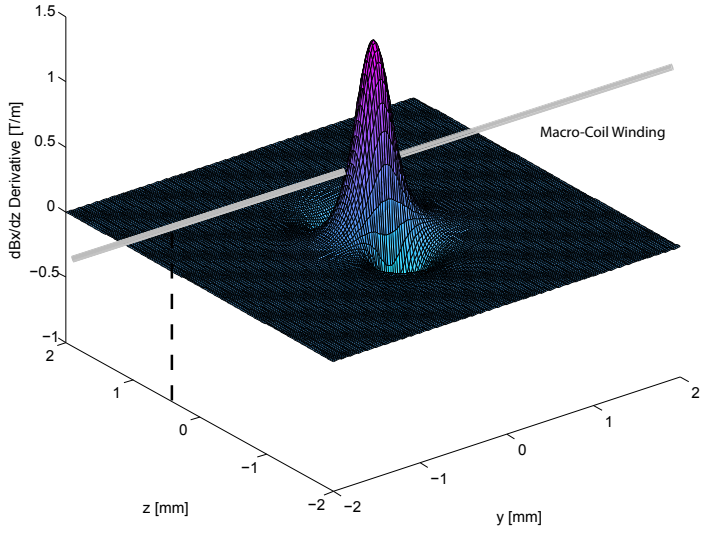

Figure 31: Macro coil alignment.

Figure 32 shows the side band amplitude in variation of length and width of a rectangular pick-up coil with proper edge alignment for a representative configuration. Macro coils have a pick-up voltage of about 50% of the maximal value obtained for the optimal rectangular μ-coil. Thus, similar to the previous cases there is no real outperformance for the μ-coil observable. Figure 32 has been numerically simulated with the original $\vec{B}$ field function 3.48 and equation 3.40.

Figure 33(a) shows a numerical simulation of the pick-up voltage in relation to the alignment of the macro pick-up coil. The maximum output amplitude is reached when the pick-up coil center is at $z_p = -1.753\,\text{mm}$, that corresponds to the alignment of the pick-up coil edge z_{p2} to the zero crossing of the derivative field on the positive z-coordinate. This is in good agreement with the findings above

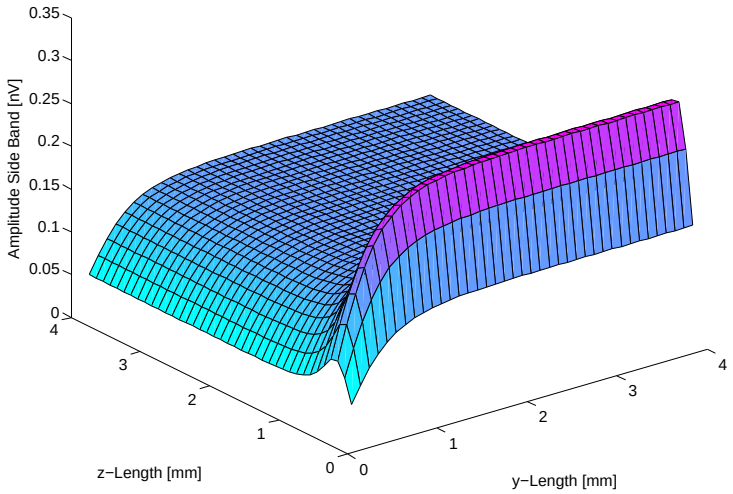

Figure 32: Side band amplitude of a rectangular pick-up coil in variation of pick-up coil length and width at a distance of $x_p = 300\mu m$ to a magnet bar (400 µm x 400 µm x 2.5 µm). Pick-up coil is optimally aligned to magnet bar. Used parameters: magnetization $M_z = 1\,\mathrm{kA/m}$, probe frequency $f_p = 100\,\mathrm{kHz}$, vibration frequency $f_m = 2\,\mathrm{kHz}$ and deflection $\Delta\hat{z}_p = 1\,\mu\mathrm{m}$.

and the condition 3.108. Figure 33(b) illustrates the relation of pick-up voltage and distance pick-up coil to magnet bar. The read out sensitivity is improved by decreasing the distance pick-up coil to magnet bar what is intuitively expected.

3.7.3 Resonator Structure Size

Figure 34 shows the side band amplitude as a function of the resonator structure length and width. The plot shows a numerical simulation of the original $\vec{B}$ field function 3.48 and equation 3.40. The same comment apply here as in the case of in-plane motion and out-plane magnetization. It is intuitively expected that the pick-up voltage is increased when the resonator structure size is increased, because the magnitude of the $\vec{B}$ field increases with the resonator structure size. While the pick-up voltage increases fairly linear with the resonator structure length the variation of the width increases the voltage until to a critical width and from there the voltage keeps constant for larger widths.

In the appendix A.1 figure 71 shows the pick-up voltage in variation of the

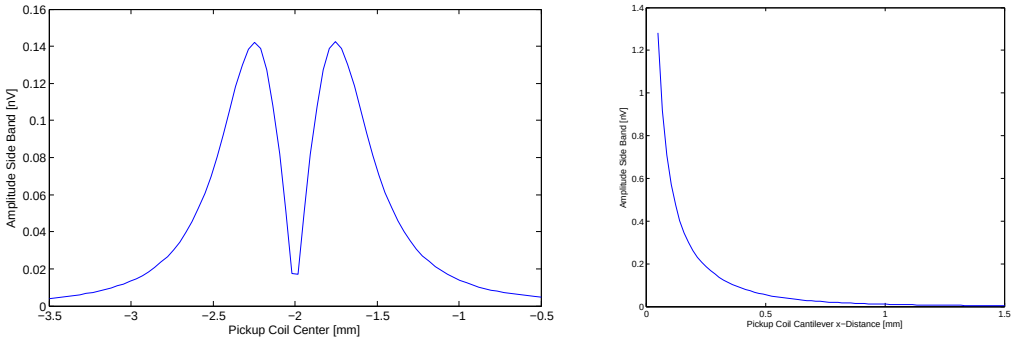

(a) Center coordinate variation (b) Distance coordinate variation

Figure 33: Side band amplitude of a rectangular pick-up coil (4 mm x 4 mm) in variation of the pick-up coil (a) center z_p coordinate ($y_p = 0\,\text{mm}$) and (b) distance coordinate x_p to a magnet bar (400 µm x 400 µm x 2.5 µm). For (a) the distance coordinate is $x_p = 300\,\mu\text{m}$ and for (b) the center coordinate z_p is adjusted optimally depending on the distance coordinate x_p and $y_p = 0\,\text{mm}$. Used parameters: magnetization $M_z = 1\,\text{kA/m}$, probe frequency $f_p = 100\,\text{kHz}$, vibration frequency $f_m = 2\,\text{kHz}$ and deflection $\Delta\hat{z}_p = 1\,\mu\text{m}$.

resonator structure thickness. As expected by intuition, the side band amplitude increases linearly with the resonator structure thickness.

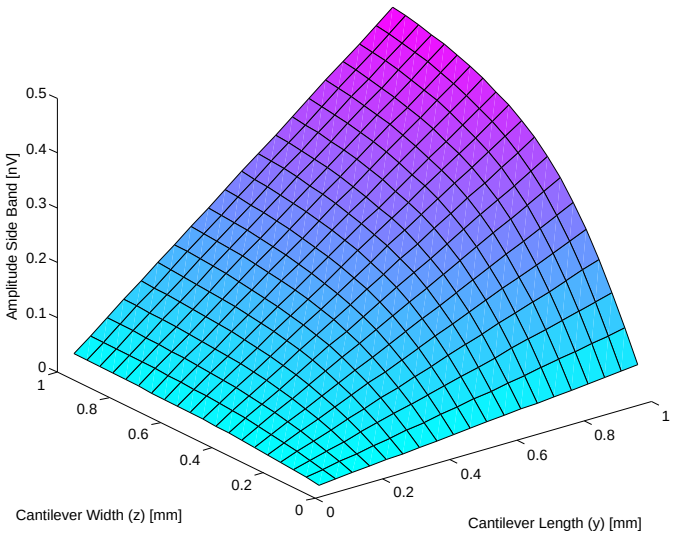

Figure 34: Side band amplitude of a rectangular pick-up coil (4 mm x 4 mm) in variation of the magnet bar length and width with a magnet bar thickness of 2.5 µm. Pick-up coil is optimally aligned to magnet bar and the distance pick-up coil magnet bar is $x_p = 300\,\mu\text{m}$. Used parameters: magnetization $M_z = 1\,\text{kA/m}$, probe frequency $f_p = 100\,\text{kHz}$, vibration frequency $f_m = 2\,\text{kHz}$ and deflection $\Delta\hat{z}_p = 1\,\mu\text{m}$.

3.8 Conclusions from the Simulation

For the different read out arrangements analytical expressions have been derived and numerical simulations have been performed. The effects of the various physical and geometrical parameters on the read out performance have been analyzed and wherever possible quantified. It is clear for e.g. how the optimal geometry of the pick-up coil should look like and where the pick-up coil should be located for an optimal read out. The side band amplitude is proportional to the probe frequency, the probe magnetization and the deflection. The increase of any of these parameters is a possible way to increase the side band amplitude.

The quantitative pick-up voltages have to be examined in order to assess the feasibility of a successful read out system. For a larger structure of a lateral plate resonator with dimension of 300 µm x 300 µm x 2.5 µm, one obtains with equation 3.40 or from the various plots in the respective sub section a read out amplitude of 2.7 nV. The read out amplitude was determined with an optimal pick-up coil alignment, a resonator plate probe magnetization $M_z = 0.25\,\mathrm{kA/m}$, a deflection amplitude $x_d = 10\,\mu\mathrm{m}$, a probe frequency $f_p = 800\,\mathrm{kHz}$ and a plate to pick-up coil gap $z_p = 300\,\mu\mathrm{m}$. The selected plate to pick-up coil gap $z_p = 300\,\mu\mathrm{m}$ is a realistic value for the flow channel arrangement. The selected resonator plate probe magnetization $M_z = 0.25\,\mathrm{kA/m}$ is representative for the used experimental setup and a MPC nanoparticle volume concentration of 4%. For smaller structures the read out amplitudes are even lower. Such very low voltage amplitudes are demanding for any detection system.

The situation is significantly better for the cobalt-nickel resonator structures. They posses a larger magnetization capability and, therefore, they are more promising for the read out.

A good lock-in amplifier has a thermal spectral noise density of about $5\,\mathrm{nV/Hz^{1/2}}$ and a good pre-amplifier has even a slightly lower figure. The effect of the thermal noise can be controlled by the selection of the bandwidth at the lock-in amplifier. However, a low bandwidth causes a slow sweep time, which may become a bothersome waiting time. A sufficient signal to noise ratio is required to distuingish the read out signal from the noise. For the low MPC read out amplitudes, the

bandwidth needs to be selected very low.

Crucial for a successful read out is the first amplification stage. The performance characteristic of this amplifier has to be excellent. It needs to have a very low noise figure and to be highly linear. Moreover, one important task of the first amplifier is to remove the large signal portions of the excitation - and probe frequency present in the pick-up signal. The excitation - and probe frequency signal parts are estimated to be a factor of 10^7-10^8 larger then the resonator structure signal. These interfering frequency components have to be removed thorough in order to avoid saturation of the amplifier stages, reduction of the sensitivity and to avoid frequency mixing. The frequency mixing between the excitation - and the probe frequency is called intermodulation distortion and generates an error signal on the first side band of the probe frequency. The amplifier needs to be highly linear to prevent from the frequency mixing effect. For this task, a special amplification-compensation-signal-conditioning (ACSC) unit is designed.

4 Fabrication of Cobalt-Nickel Structures

The fabrication process of the cobalt-nickel (CoNi) structures is to a significant extend adopted from the process of the magnetic nanoparticle polymer composite (MPC) structures developed by M. Suter *et al.* [43]. The MPC is made of SU-8 with distributed superparamagnetic Fe_3O_4 nanoparticles (mean diameter > 8 nm). Superparamagnetic materials have almost zero remanent magnetization and very low magnetization hysteresis. For the CoNi structures the structural layer of MPC is replaced by cobalt-nickel. CoNi is a soft magnetic material and exhibits a larger magnetization than the MPC structures at the same applied magnetic field. MPC structures have a 1-5% volume percentage concentration of Fe_3O_4 nanoparticles and posses a lower magnetization capability due to the low concentration. However, on the other side the functionalization capability and the biocompatibility of CoNi structures is less favorable than for polymers.

The magnetization characteristic of a soft magnetic body is discussed in more detail in the following section 5. It is mentioned here, the CoNi structures have an intrinsic anisotropy in their magnetization characteristic due to their large aspect ratio shapes. Structures made of superparamagnetic materials in contrast show an isotropic magnetization characteristic because of the negligible magnetic interaction between the nanoparticles.

The magnetic properties of electrodeposited CoNi thin films have been characterized by O. Ergeneman *et al.* [16].

4.1 Overview Fabrication of MPC and CoNi Structures

Figure 35 depicts the fabrication process of magnetic nanoparticle polymer composite - and CoNi structures. In case (a), the structure layer out of photosensitive MPC is spun with a thickness of 2.5 µm on the Cr/Au/Cr/Si wafer and exposed with the first photolithography step. Then, the 70 µm anchor layer out of SU-8 is spun and exposed with the second photolithography step. After that, both layers are developed. As a last step, the complete structure is released by selectively etching the Cr release layer.

In case (b), a 6 µm CoNi structure layer is electroplated on a photolithographic patterned Cu/Si wafer. A thin Au adhesion layer is then electroplated on the CoNi structure layer, which improves adhesion of the SU-8 anchor layer on the metallic structure layer. The 90 µm anchor layer out of SU-8 is patterned with a second photolithography step. Lastly, the structure is released by etching the Cu sacrificial layer.

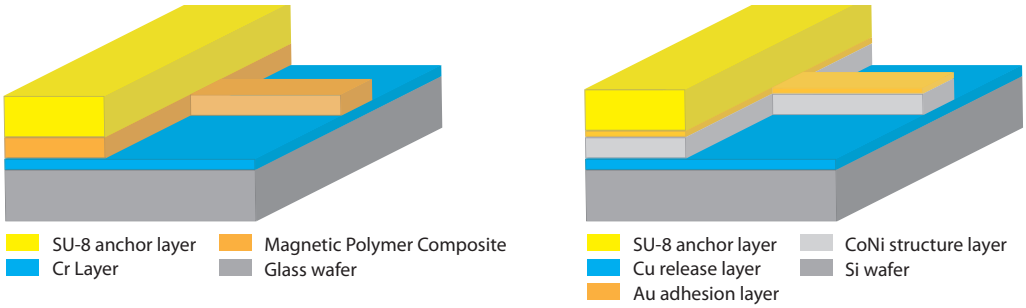

(a) Fabrication Polymer Composite Structures

(b) Fabrication CoNi Structures

Figure 35: Fabrication process of MPC - and CoNi structures.

4.2 Detailed Fabrication Process of CoNi Structures

Figure 36 illustrates the detailed fabrication process. In the following the process is explained according the numbering scheme of figure 36. It should be noticed that the fabrication process consists of steps performed in the clean-room and steps outside of the clean-room. The steps outside of the clean-room are obviously dirty and it deals with evaporation, electroplating, dicing and sacrificial layer etching. However, in the case of dicing and sacrificial layer etching the process does not need any further clean-room processing. In case of evaporation and electroplating care has to be taken to avoid contamination and if required wafers have to be cleaned before further clean-room work can be started.

Before any fabrication and wafer processing can be started, new wafers have to be cleaned as follows in order to remove any contamination:

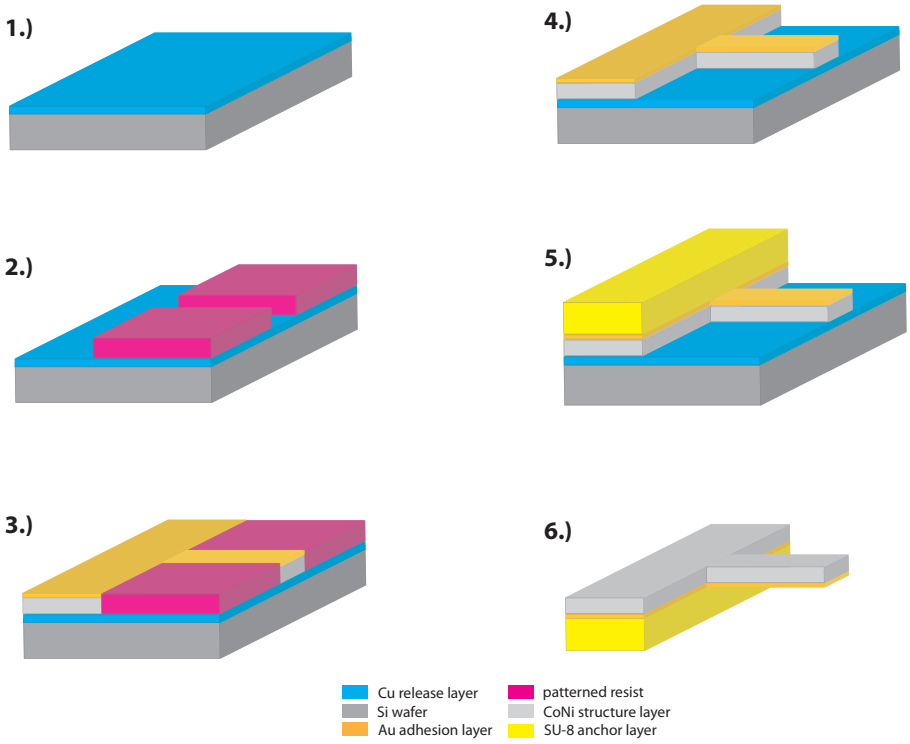

Figure 36: Detailed fabrication process of CoNi structures.

i. 10 min in acetone with ultrasonic at power 9

ii. 10 min in isopropanol with ultrasonic at power 9

iii. 10 min in piranha (Piranha is a cleaning agent based on sulfuric acid H_2SO_4 and hydrogen peroxide H_2O_2 at a mixture ratio of 3:1)

iv. quick dump rinsing until the resistivity of the bath reaches 12 MΩ

v. drying in the rinser dryer at wafer program 2

vi. plasma ashing 10 min at 600 W

The wafers are now ready to start with the concrete fabrication sequence of the CoNi structures:

1. A 1 µm Cu sacrificial layer is evaporated on the clean Si wafer. Underneath a 25 nm Ti adhesion layer is evaporated to improve the adhesion between the Cu layer and the Si wafer.

2. As the evaporation process is done outside the cleanroom, the wafer should be cleaned with acetone and isopropanol under exposure to ultrasonic for 5 min at power 9. The wafers are, then, rinsed in the quick dump rinser and dried in the rinser dryer at program 3. Resist AZ4562 [36] from Microchemicals, Inc. is spun with a thickness of 10.5 µm on clean wafers. Wafers are pre-baked for 10 min at 100 °C before the exposure with the first photolithography step. The wafer is exposed with the structural layer mask. After the exposure, the wafer is developed for 4 min in 20% volume concentration of MF351 [42] from Shipley, Inc. It follows quick dump rinsing and drying in the rinser dryer at program 3.

3. The structure layer CoNi with a target thickness of 6 µm is electroplated at a current density of $J = 20\,\mathrm{mA/cm^2}$. A few ten nm Au adhesion layer is then electroplated at a current density of $J = 10\,\mathrm{mA/cm^2}$.

4. It follows stripping of the resist with acetone and subsequent cleaning with acetone and isopropanol under exposure to ultrasonic for 5 min at power 9. After that the wafers are rinsed in the quick dump rinser and dried in the rinser dryer at program 3.

5. A thin layer of Omnicoat [33] from Micro Chem, Inc. is spun on the wafers and used as an adhesion promoter between the Au/CoNi structural layer and the SU-8 anchor layer. The Omnicoat layer is pre-baked at 200 °C for 1 min. Then, the anchor layer SU-8 [34] is spun on the wafers. Before the exposure with the second photolithography step, the wafers are pre-baked for 20 min at 65 °C and then cooled down to room temperature for about 2 h. The wafer is exposed with the anchor layer mask. After the exposure, a post-bake is performed for 40 min at 65 °C and then cooled down to room temperature for about 2 h. Then, the wafers are developed in Mr-Dev600 [35] from Micro Resist Technology, Inc. for about 6 min. Lastly, a cleaning in isopropanol for 10 min and in DI water for 5 min is performed before the drying in the dryer rinser at program 3. The anchor layer shows an average thickness of 90 µm with a standard deviation of 5 µm in the center and an average thickness of 110 µm with a standard deviation of 15 µm at the edge of the wafer.

6. Before dicing, the structure on the wafer is protected by a thin layer of

resist AZ4562 [36] from Microchemicals, Inc., which is spun onto the wafer. The wafer is then diced into individual dies and subsequently the release is performed by etching the Cu sacrificial layer. 5.2 g Ammonium persulfate $(NH_4)_2S_2O_8$ dissolved in 40 ml ammonia and 100 ml DI water is used as selective copper etchant. The dies can be bonded to a flow channel prior or after the etch step.

4.3 Electroplating of CoNi and Au

The deposition of CoNi and Au was performed with a DC current flowing from the anode through the electroplating bath to the cathode, where the deposition of the respective metal takes place. In this case, the cathode was the wafer. Electroplating can be a rather complex process if one studies it in detail. The working principal can be explained, however, in an easy and intuitive way. Positively charged metal ions are present in the electroplating bath and if an external electrical field is applied, the electrical field provokes a Coulomb force acting to the metal ions in direction of the electrical field and to the cathode respectively. When the metal ions reach the cathode, the metal ions deposit on the surface of the cathode and become electrically neutral by adding an electron from the current supply. The metal layer on the cathode grows as long as current is flowing and as long as metal ions are present in the bath. The deposition rate per area can be quite precisely controlled via the current density and the thickness of the deposited layer by the deposition time.

The composition of the bath used for the CoNi plating is as specified in table 1 and the plating was performed at the conditions in table 2. The resulting deposition is nickel rich, but the exact chemical composition has not been analyzed yet.

Element	**Quantity**
Nickel Sulfate $6H_2O$	250 g/l
Cobalt Sulfate $6H_2O$	50 g/l
Boric Acid H_3BO_3	45 g/l
Sodium Saccharinate	3 g/l
Sodium Allyl Sulfonate	5 ml/l
Organic Additives	2 g/l
Wetting Agent	3 ml/l

Table 1: CoNi bath composition.

The Au bath composition employed for the Au plating is according table 3 and the conditions for the plating process are listed in table 4. All the chemicals whose compositions are not known are proprietary chemicals of McDermid Inc., USA.

Condition	**Quantity**
Temperature	55 °C
pH	5
Agitation	Moderate Air Agitation
Anode	Nickel Sheet
Current Density	20 mA/cm^2
Deposition Time for 6 µm	877 s

Table 2: CoNi Plating Conditions.

Element	**Quantity**
Gold Potassium Cyanide (66%)	8 g/l
Potassium Citrate	90 g/l
Citric Acid	90 g/l
Brightener Concentrate	10 ml/l

Table 3: CoNi bath composition.

Condition	**Quantity**
Temperature	32 − 35 °C
pH	4
Agitation	Vigorous Air Agitation
Anode	Platinized Titanium Mesh
Current Density	10 mA/cm^2
Deposition Time for 20 nm	12 s

Table 4: Gold Plating Conditions.

4.4 Adhesion between Au/CoNi layer and SU-8 layer

The poor adhesion between the Au/CoNi layer and the SU-8 layer was one of the major challenges to overcome in the development of the fabrication process. Several publications ([38], [11]) report about the low adhesion between metals and SU-8. Mainly during the etching of the Cu release layer the adhesion was lost and the anchor layer and structure layer felt apart. It was observed that the etchant penetrated into the interface between the two layers and as a consequence the adhesion was lost. However, there was no etching of the CoNi or Au observed. The same phenomenon was observed in water with some longer waiting time. First, it was started with SU-8 on CoNi and the introduction of a thin Au coating over the CoNi layer improved the adhesion, but was, however, still insufficient for the etching process. In [38], it had been reported a more than doubled bond strength for SU-8 on Au if Omnicoat is employed as an adhesion promoter. Omnicoat [33] is a proprietary product from MicroChem, Inc. In this process, the Au/CoNi layer was coated with a thin layer of Omnicoat before the SU-8 anchor layer was spun on. The Omnicoat coating was spun and then pre-baked for 1 min at 200 °C.

4.5 Results from the Fabrication of CoNi Structures

Figure 37 shows two SEM photos of the CoNi structures. As figure 37 indicates, the structure layer is nicely formed in CoNi and even small springs are well preserved (see (b)).

4.5.1 Uniformity of Electroplated CoNi Layer

The electro-plating was performed by a DC current and variations in thickness especially at edges and small structures have to be expected. In the center of the wafer at structures with larger areas a thickness of approximately 6 µm was measured by means of the profiler and the white light interferometer. At smaller structures like springs the thickness varied from $7 - 11\,\mu m$. At the edge of the wafer at structures with larger areas a thickness of $11 - 14\,\mu m$ was observed and the spring thickness increased to $8 - 16\,\mu m$. Even within the same device variations of the spring thickness among resonators of the same design were en-

countered. One method to improve the thickness uniformity is to use a pulsed current electroplating process or alternatively reduce the current.

4.5.2 Resonant Frequency Measurements

Two types of devices with in-plane plate resonators were measured with the planar motion analyzer. The first device consists of a row of six quadratic plates with dimension 400 µm x 400 µm suspended by a spring with dimension 200 µm x 11 µm. The springs are clamped to an anchor bar. The thickness of the plate was measured to be $12 - 14\,\mu m$ and the thickness of the springs varied from $13.5 - 15.5\,\mu m$. These plate resonators vibrate in their first mode in in-plane direction. Figure 38 illustrates the arrangement and design of the resonator structures. Table 5 summarizes the obtained measuring data of the in-plane vibration. Resonant frequencies between $4.51 - 4.68\,kHz$ were detected for the six plate resonators. It is intuitive, that the variation of the plate and spring thickness is most likely the reason for the resonant frequency variation. An eigenfrequency mode analysis with COMSOL computed an in-plane eigenfrequency of 4.4 kHz.

Plate	**Resonant Frequency**	**Deflection Amplitude**
1	4.51 kHz	9 µm
2	4.42 kHz	12 µm
3	4.47 kHz	19 µm
4	4.53 kHz	21 µm
5	4.61 kHz	17 µm
6	4.68 kHz	21 µm

Table 5: Measured in-plane resonant frequencies and maximum deflection amplitudes of six 400 µm x 400 µm plates suspended by a 200 µm x 11 µm spring arranged in a row. The design of the plate resonators is depicted in figure 38.

The second measured device consists of three rows of four quadratic plates. The plate have a dimension in the first row of 400 µm x 400 µm, in the second row of 300 µm x 300 µm and in the third row of 250 µm x 250 µm. The plates are suspended by a spring with dimension 200 µm x 11 µm and the springs are clamped to an anchor bar. The thickness of the plate was measured to be $8 - 10\,\mu m$ and

the thickness of the spring varied from $8 - 11\,\mu m$. Figure 39 illustrates the arrangement and the design of the resonator structures. Table 6 summarizes the obtained measuring data of the in-plane vibration. Like in the previous case, the variation in resonant frequency is due to the thickness variation of plate and spring.

Plate	**Resonant Frequency**	**Deflection Amplitude**
1L	4.39 kHz	12 µm
2L	4.39 kHz	15 µm
3L	4.39 kHz	14 µm
4L	4.43 kHz	12 µm
1M	7.32 kHz	7.5 µm
2M	7.22 kHz	8 µm
3M	7.18 kHz	8 µm
4M	7.22 kHz	7.5 µm
1S	4.68 kHz	7.5 µm
2S	4.68 kHz	8.5 µm
3S	4.68 kHz	8 µm
4S	-	-

Table 6: Measured in-plane resonant frequencies and maximum deflection amplitudes of plate resonators suspended by a spring arranged in three rows. Plate dimension: first row 400 µm x 400 µm, second row 300 µm x 300 µm, third row 250 µm x 250 µm. Spring dimension: 200 µm x 11 µm. The design of the plate resonators is depicted in figure 39.

In the appendix B the deflection frequency response diagrams of the in-plane mode of three plate sizes are in figure 72, 73 and 74 obtainable. The eigenfrequency mode analysis was performed with COMSOL simulation. Table 14 lists the used settings for the simulation.

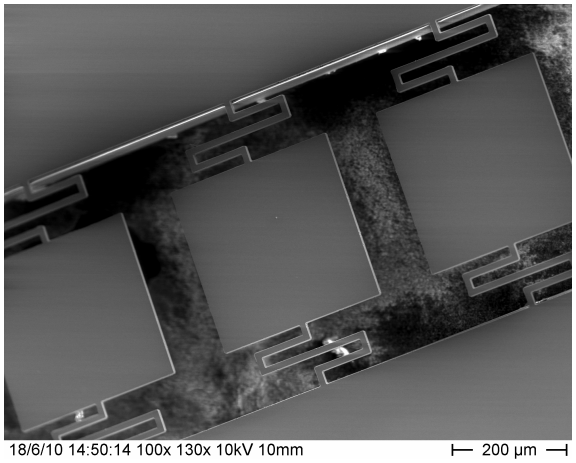

(a) SEM Photo of Double Clamped CoNi Structure

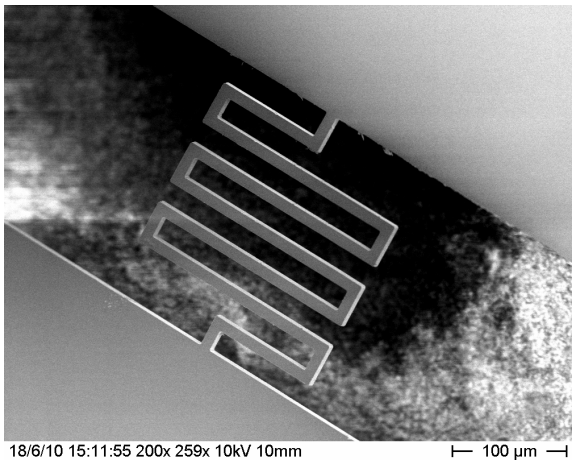

(b) SEM Photo of CoNi Spring

Figure 37: SEM photos of CoNi structures. Underneath of the CoNi structure layer the SU-8 anchor layer is visible in (a).

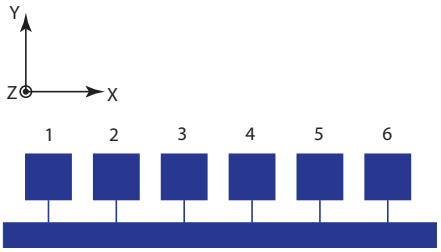

Figure 38: Arrangement of a row of six plate resonators. The in-plane mode vibrates in the x-direction in the x-y plane.

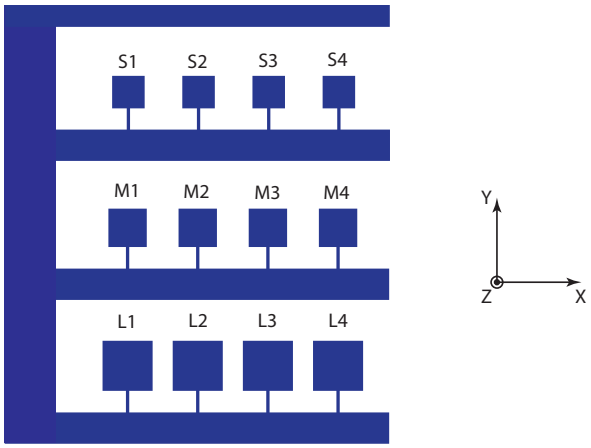

Figure 39: Arrangement of three rows of four plate resonators. The in-plane mode vibrates in the x-direction in the x-y plane.

5 Read Out Experiment

5.1 Magnetization of Soft Magnetic Bodies

The magnetization characteristic of a soft magnetic body is a function of the magnetic susceptibility and is for ferromagnetic materials also a function of the geometry of the body and the magnetization direction.

In case of superparamagnetic MPC, the volume concentration, the size and the shape of the nanoparticle influence the magnetization characteristic. For soft ferromagnetic materials like CoNi the shape of the body can provoke an anisotropy in the magnetization characteristic. Superparamagnetic materials, in contrast, posses no shape anisotropy and have the same magnetization characteristic in all directions. Detailed information on the magnetization of soft ferromagnetic bodies can be obtained in [1] from J. Abbott *et al.*.

The body internal magnetic field $\vec{H}_I$ induces a magnetization $\vec{M}$ as a function of the magnetic susceptibility χ

$$\vec{M} = \chi \vec{H}_I \tag{5.1}$$

The magnetization $\vec{M}$ provokes a demagnetization field $\vec{H}_D$ within the body counteracting the applied magnetic field $\vec{H}$. The internal magnetic field is a superposition of the two magnetic field components

$$\vec{H}_I = \vec{H} + \vec{H}_D \tag{5.2}$$

For the demagnetization field $\vec{H}_D$, one can set up the following Ansatz

$$\vec{H}_D = \mathbf{N} \cdot \vec{M} \tag{5.3}$$

where $\mathbf{N}$ represents a matrix relating the magnetization field $\vec{M}$ to the demagnetization field $\vec{H}_D$.

For a resonator with a plate geometry, the matrix $\mathbf{N}$ can be assumed with good approximation to have diagonal form $\mathbf{N} = diag(n_x, n_y, n_z)$ for coordinates within the body if the coordinate frame coincides with the principal axis of the plate. For the case of diagonal matrix form, the magnetization components can be related to their respective applied magnetic field components

$$M_{x,y,z} = H_{x,y,z} \frac{\chi}{1 + n_{x,y,z}\chi} \tag{5.4}$$

Considering the large aspect ratio of a plate geometry, the following relation holds true $L > W >> th$. It is assumed to have the length L in x-direction, the width W in y-direction and the thickness th in z-direction. The x-direction, which is in-plane, is in such a body easy magnetized since the demagnetization component is low and its demagnetization factor n_x. Hence, the x-direction can be called the easy magnetization axis. Equation 5.4 converges for $n_x << 1$ to

$$M_x = H_x \chi \tag{5.5}$$

In z-direction, which is the out-plane direction, the magnetic field has a large demagnetization component and the z-direction is then accordingly called the hard magnetization axis. For $n_z\chi >> 1$ equation 5.4 can be reduced to

$$M_z = H_z \frac{1}{n_z} \tag{5.6}$$

and for the case of $n_z \approx 1$ equation 5.4 converges to

$$M_z = H_z \tag{5.7}$$

It can be concluded for large aspect ratio geometries like plates, the out-plane magnetization has only about the magnitude of the applied field.

For bodies made of superparamagnetic material the detailed situation is more complex than presented here. However, at the macroscopic level the observed magnetization characteristic is isotropic due to the low magnetic interaction between and the small size of the nanoparticles. It is a function of the applied magnetic field, but not of the direction and the body geometry.

5.2 Design of the Experimental Setup

The experimental setup was designed based on the selected read out strategy presented in section 2, the results of the simulation presented in section 3 and on previous work available in [17], [13]. The setup consists of two principal elements the actuation part to excite the resonator structure and the read out part to sense the vibration frequency. Figure 40 illustrates the situation.

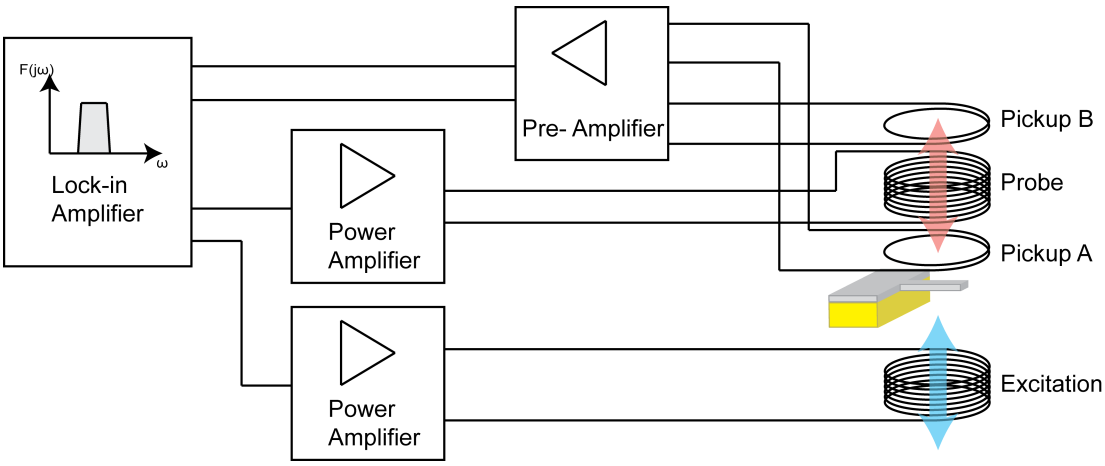

Figure 40: Experimental setup.

In the presented setup the probe coil is located above and the excitation coil below the resonator structure. The probe coil induces a probe field at the resonator structure with a frequency much larger than the mechanical vibration frequency of the resonator structure. The mechanical deflection of the resonator structure modulated with the probe field induce the read out probe side band in pick-up coil A. Two pick-up coils are arranged symmetrically to the probe coil in order to cancel the large signal induced by the probe field. The ACSC unit amplifies the weak pick-up signal and incorporates electronic compensations to reduce the signal induced by the excitation field and to further reduce the signal induced by the probe field. Additionally, the errors signal at the probe side band induced by the intermodulation distortion can be compensated. The amplified and compensated pick-up signal is then fed to the lock-in amplifier, which recovers the read out signal out of the noisy pick-up signal. The lock-in amplifier drives also via two power amplifier the probe - and excitation coil. As a result of the previous work [13] the combination of excitation - and probe coil is changed

to a separate excitation - and a separate probe coil. In the previous work one power amplifier was used to drive the excitation - and probe signal, which lead to a distortion component at the probe side band due to the non-linearity of the power amplifier. The separation of the coils allows to employ two power amplifiers and to reduce the distortion level. It further allows to optimize the coils for their respective operation frequency. On top of the lock-in amplifier a LabView code is running, which is not shown in figure 40, to control the measurement process. Table 15 in the appendix references the used instruments in the experiment.

Additional to figure 40 a pair of DC-coils is employed to generate a DC magnetic field to induce a large DC magnetization in the resonator structure. Figure 41 depicts the situation with the DC coils. The DC coil pair is arranged such that it can be tilted for 90^0 to allow out-plane or in-plane magnetization of the resonator structure. Depending on vertical or lateral excitation out-plane or in-plane magnetization is needed.

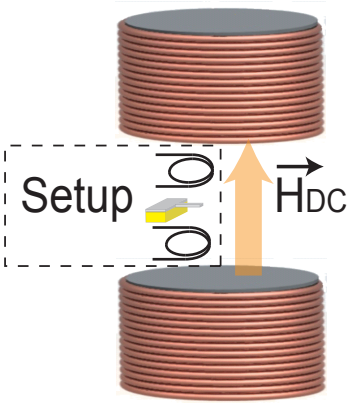

Figure 41: Experimental setup with DC coils.

In order maximize the symmetry and cancellation effectiveness of the two pick-up coils a μ-positioning stage is used to adjust the position of the pick-up coils to the probe coil. A second μ-positioning stage allows for a precise positioning of the resonator structure with respect to the pick-up coil. Figure 42 illustrates the usage of the μ-positioning stages. Figure 78 and 79 in the appendix show pictures of the experimental setup.

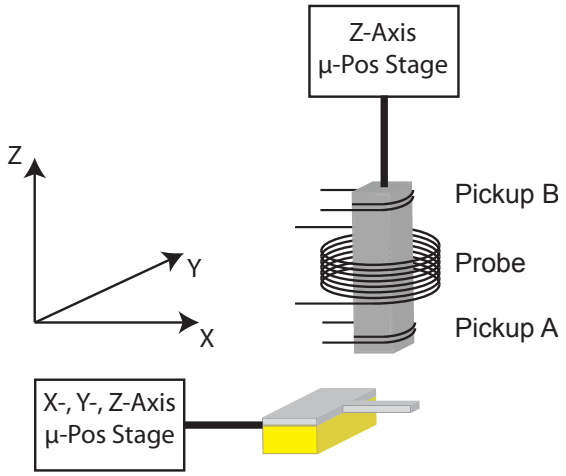

Figure 42: μ-Positioning Stages.

5.2.1 Design of DC Coil Pair

At the resonator structure, the exerted force is described by equation 3.33. As described by equation 3.33 the resonator structure magnetization is apart from the magnetic field gradient one of the force generating terms of equation 3.33. In the case of soft magnetic material the magnetization has to be induced by an external magnetic field. There are obviously two ways to generate the external magnetic field, the first is with an electromagnet and the second is by a permanent magnet. The electromagnet has some distinct advantages in the read out application, the field strength can be adjusted by the current and the magnetization characteristic is highly linear if used in vacuum or air. However, the permanent magnet is more compact and does not require current supply, but has a non-linear magnetization characteristic. A non linear magnetization characteristic generates an intermodulation distortion and, hence, an error signal at probe side band.

It is easier to generate a DC than an AC magnetic field, since less power from the current supply is needed. Due to that a DC field, generated by a coil pair, is employed to magnetize the resonator structure. The higher magnetiza-

Dimension	**(mm)**
Inner Radius	26
Outer Radius	66
Height	40
Gap Between Coils	10

Table 7: DC coil dimensions of the conductor without considering the coil body.

tion leads to a significantly increased exerted force at the resonator structure. In case of vertical excitation the DC field is directed in out-plane direction and for lateral excitation in in-plane direction. The DC coil pair can be tilted by 90^0 to accomplish the needed direction of the magnetic field. Figure 43 depicts the magnetization characteristic of SU-8 Fe_3O_4 nanoparticle polymer composite and illustrates the change in magnetization by using the DC magnetic field.

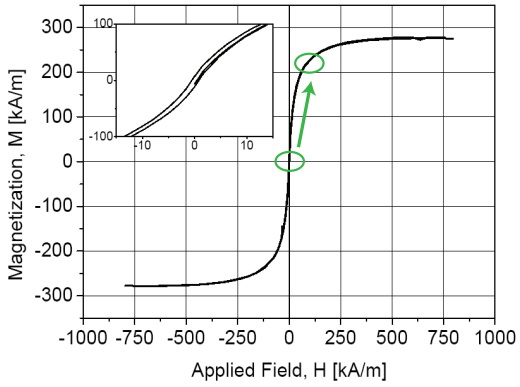

Figure 43: Magnetization of SU-8 Fe_3O_4 nanoparticle polymer composite at room temperature. The green arrow indicate the change of magnetization by using a DC magnetic field.

Based on figure 43 a magnetic field strength of up to 100 kA/m from the DC field is desirable and allows a large magnetization on the resonator structure. The DC coil pair was optimized by COMSOL FEM simulations regarding the mechanical dimensions and magnetic field strength. Table 7 shows the dimensions evaluated as optimal for the read out setup.

Figure 44 depicts the magnetic field of the DC coil pair. A maximum field strength of 83 kA/m is achieved at the resonator structure with the given current

density of 4.6 MA/m^2. This is lower than the demanded value, but represents a reasonable compromise between coil size and magnetic field strength. Table 16 in the appendix lists the settings used in the COMSOL simulation environment.

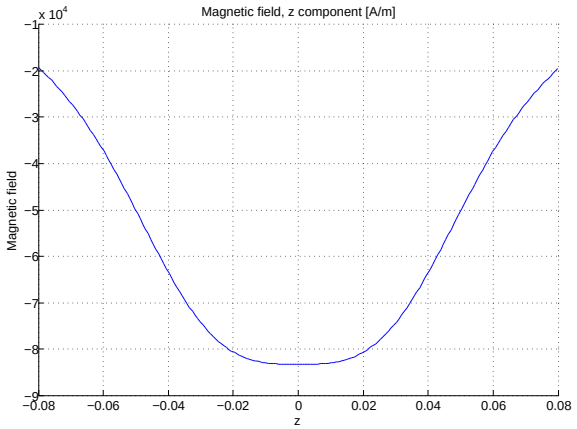

Figure 44: Magnetic field of DC coil pair. The resonator structure is located at z=0 mm.

5.2.2 Design of Excitation Coil

The purpose of the excitation coil is to generate a magnetic field gradient at the resonator structure. As mentioned in the last sub section the exerted force on the resonator structure is a function of the magnetic field gradient and the magnetization. It is desirable to achieve from the excitation coil a large magnetic field gradient while the magnetic field magnitude is kept low. Larger magnetic field magnitudes induce a magnetization at the excitation frequency and, hence, the exerted force by this component has the doubled excitation frequency. Based on the work from O. Ergeneman *et al.* [17] a field gradient $\frac{\partial B_i}{\partial i}$ of approximately $8 \cdot 10^5$ A/m^2 is required to actuate magnetic nanoparticle polymer composite structures.

As mentioned in the previous section, the DC magnetic field is aligned in vertical direction for vertical excitation and aligned in horizontal direction for horizontal excitation. If the resonator structure is made up of soft magnetic material the resonator structure DC magnetization direction coincides with the DC magnetic field. In the described setup and in consideration of equation 3.33, for

vertical excitation the field gradient $\frac{\partial H_z}{\partial z}$ and for lateral excitation the field gradient $\frac{\partial H_r}{\partial r}$ is decisive. Thus, the major force component is in the direction of the main DC magnetization component. There is, however, a minor force component generated in the other direction, but the magnitude is small for soft magnetic materials. For soft magnetic materials, the minor force component oscillates at the doubled excitation frequency because the magnetization is provoked by the excitation field.

Based on the requirement to obtain a large field gradient, the excitation coil should have preferably a small inner diameter in combination with a large cross section carrying sufficiently current. The design process of the excitation coil is, however, not so easy as it might look at the first glance. For instance one may start with the available current of the power amplifier, which may lead to a design meeting all specifications except the maximum voltage of the power amplifier at the upper frequency range. This, in turn, leads to iterations until all specifications are met. The system is in fact overdetermined if current and voltage of the power amplifier are used as independent constraints.

A more general way, which does not lead to iterations, is an energy Ansatz by using the output power capability of the power amplifier. In each period of the excitation signal the magnetic field of the excitation coil has to be *"charged"* and *"discharged"*.

Summarizing, the process is as follows:

1. Determine the energy in the inductor at the maximum output power of the power amplifier and at the highest excitation frequency.

2. By means of FEM simulation, optimize the design of the excitation coil in order to maximize the field gradient with the constraint of the maximum inductor energy.

3. The wire diameter has to be selected such that the coil current at the given wire current density meets approximately the maximum output current of the power amplifier. Compute with the optimized coil dimensions and the selected wire diameter, the winding number, the inductance and the skin

depth. The skin depth should be larger than the radius of the wire. If the skin depth is lower, a HF wire consisting of insulated single wires has to be used.

4. By means of the inductance, check at the highest excitation frequency if the required coil current can be delivered with the maximum output voltage of the power amplifier. This is to double-check that all the calculations have been performed correctly. If the process has been followed no iterations are required.

The described process optimizes the coil design for the highest excitation frequency. For lower frequencies, the same magnetic field strength can be obtained at a lower output voltage of the power amplifier because the inductance of the coil is lower. The coil current, however, should be kept the same. A lower coil current reduces proportionally the magnetic field strength.

The energy in an inductor with sinusoidal excitation can be computed as follows

$$Q(t) = \hat{U}cos(\omega t)\hat{I}sin(\omega t) = UIsin(2\omega t) \tag{5.8}$$

$$E(t) = \int Q(t)dt = \frac{UI}{2\omega}(1 - cos(2\omega t)) \tag{5.9}$$

$$\hat{E} = \frac{UI}{\omega} = \frac{S_{max}}{2\pi f_e} \tag{5.10}$$

$$\tag{5.11}$$

where as $Q(t)$, $E(t)$, $\hat{E}$, S_{max} represents the reactive power, the inductor energy, the peak inductor energy and the maximum apparent output power of the power amplifier.

Table 17 in the appendix lists the maximum apparent output power available from the power amplifier. Considering a maximal excitation frequency of 20 kHz $\hat{E}$ should be $\leq 5.97 \cdot 10^{-4}$ Ws.

The excitation coil design was optimized by using COMSOL FEM simulation. For simplification of the simulation, the single windings were combined into one

Dimension	**(mm)**
Inner Radius	2.75
Outer Radius	12.75
Height	10
Gap to Resonator	2

Table 8: Excitation coil dimensions of the conductive part without considering the coil body. Figure 45 depicts the cross section of the coil.

conductor having a rectangular cross section with height H and thickness th as depicted by figure 45. A wire current density $J_{wire} = 4.6 \cdot 10^6\,\mathrm{A/m^2}$ was used. Due to the circular shape of the wire a correction factor $\frac{\pi}{4}$ has to be considered, which results in an effective current density of $J = 3.6 \cdot 10^6\,\mathrm{A/m^2}$ used in the simulation. Within COMSOL the energy in an inductor can be computed by integrating the energy density over the computational domain. Since within the FEM simulation RMS values are used the computed energy should not exceed $\hat{E}/2$. Table 8 summarizes the selected dimensions for the excitation coil.

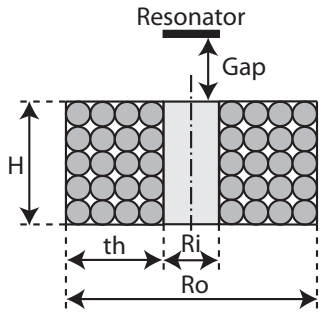

Figure 45: Cross section of the excitation coil.

Figure 46 depicts the magnetic field of the excitation coil at the RMS value of the excitation current density. Hence, the amplitude of the magnetic field is times $\sqrt{2}$ higher. Table 16 in the appendix lists the settings used within the COMSOL simulation. A field gradient in z-direction $\frac{\partial H_z}{\partial z}$ of $-4.05 \cdot 10^6\,\mathrm{A/m^2}$ and in radial direction $\frac{\partial H_r}{\partial r}$ of $-0.94 \cdot 10^6\,\mathrm{A/m^2}$ is obtained from figure 46.

Equation 5.12 and following show the relations to compute the winding number N, the inductance L and the skin depth δ.

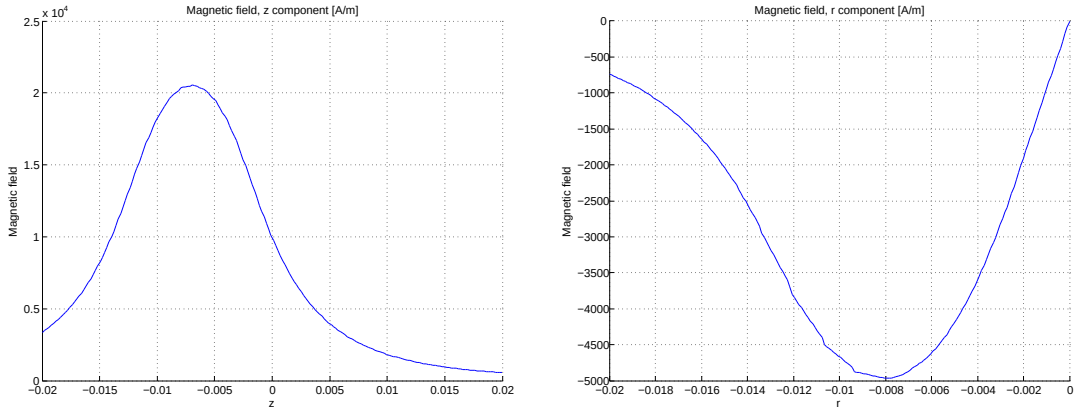

(a) Z-direction H_z at r = 0 mm

(b) Radial direction H_r at z = 0 mm

Figure 46: Magnetic field of excitation coil in z- and radial-direction. The resonator structure is located at r = 0 mm and z = 0 mm. The excitation coil is located at z = −12.. − 2 mm based on table 8.

$$N = \frac{H\,th}{d_{Wire}^2} \tag{5.12}$$

$$L = \frac{2E_{Sim}}{J\,H\,th}N^2 \tag{5.13}$$

$$\delta = \sqrt{\frac{2\rho}{\omega\mu_0}} \tag{5.14}$$

$$\tag{5.15}$$

ρ, H, th, d_{Wire}, J, E_{Sim}, ω, μ_0 denote the specific resistance, the height of the conductor, the thickness of the conductor cross section , the diameter of the wire, the effective current density, the coil energy obtained from the FEM simulation, the angular frequency and the magnetic permeability of vacuum. For the selected wire diameter of 0.4 mm table 9 shows the computed properties of the excitation coil.

The inductance was measured as 3.1 mH at $f = 100$ kHz on the experimental excitation coil. In the appendix, figure 75 shows the impedance frequency response. At frequencies below 400 kHz the excitation coil behaves like an inductor with small ohmic resistance, which is a required property over the excitation frequency band of $1 - 20$ kHz.

Property	**Value**
Winding Number (N)	625
Inductance (L)	1.6 mH
Max. Coil Current (I)	0.58 A (RMS)
Skin Depth (δ)	0.5 mm at 20 kHz

Table 9: Computed properties of the excitation coil

5.2.3 Design of Probe Coil

The goal of the probe coil is to add an additional probe magnetization on the resonator structure, which oscillates at a much larger frequency than the excitation frequency. In the simulation section 3, it has been shown that the read out amplitude is amplified with the large probe frequency and, thus, a larger read out signal can be accomplished while the signal to noise ratio is increased as well. The mechanical vibration frequency of the resonator structure modulates the probe magnetic field in the pick-up coil and thereby a probe side band is generated. It is intuitive understandable and it has been mathematically proved in section 3, the probe side band is favorable for the read out of the resonator structure.

From a design point of view the probe coil should generate a large magnetic field at the resonator structure. There are obviously limitations like the saturation and non-linearity of the magnetization characteristic of the resonator structure material, the space availability for the probe coil and the frequency response of the probe coil. Unlike in the excitation coil case the power amplifier output power capability does not represent a limitation for the probe coil. The probe frequency is constant, what allows to compensate the rather huge inductive impedance of the probe coil by a respective capacitor. For the power amplifier only the resistive component is then perceivable and the required power is far less. Electrically speaking, the probe coil is used in a resonating mode. Since only dedicated capacitor values are available, the probe frequency needs to be tuned to the respective resonance frequency of the probe coil and capacitor. In this application the capacitor is connected in series to the probe coil and the values of the used capacitances range from 46 pF to 100 pF. It is important to select high voltage capacitors because the voltage across the capacitor can easily

reach a few kV in the series resonant circuit.

With regards to the magnetization characteristic, one has to consider three components of magnetization. The first is the DC magnetization, which is due to the DC magnetic field or due to intrinsic remanent magnetization in case of ferromagnetic material. The second component is generated from the excitation magnetic field and the third from the probe magnetic field. All three components have to be balanced out to each other in order to avoid saturation and optimize the system performance.

Since the probe coil is operated at frequencies close to 1 MHz the coil behaves not only as an inductor, but also capacitances become perceivable. In this work the probe frequency is limited to < 1 MHz because of the bandwidth of the employed power amplifier. Higher probe frequencies are possible by using another power amplifier and are favorable to improve the signal to noise ratio and the read out performance (see 3). The coil capacitances are caused by the wire to wire capacitances and lower the current flowing through the inductor. Thus, the probe magnetic field is lowered.

The magnetic coupling between the probe - and the excitation coil provokes an induced voltage in the excitation coil by the changing probe magnetic field. A current flows in the excitation coil as a function of the termination impedance of the excitation coil. The current generates a magnetic field counteracting and weakening the probe magnetic field. If the situation is analyzed in the equivalent circuit view, the impedances of the excitation coil side are transformed to the probe coil side by the square of the coupling factor. As a consequence, the capacitances of the excitation coil are transformed to the probe coil side and reduce the frequency performance of the probe coil. It is worth to note that impedance measurements of the probe - or excitation coil have to be performed in the complete setup for a representative measurement.

For the design of the probe coil, it is desirable to have a low coil capacitance and to have a loose coupling between probe and excitation coil in order to maximize the probe magnetic field for a given coil current. In reality, the coil

Dimension	**(mm)**
Inner Radius	2.75
Outer Radius	8.75
Height	8
Gap to Resonator	2

Table 10: Probe coil dimensions of the conductive part without considering the coil body.

capacitances become perceivable at frequencies $f > 100\,\text{kHz}$ and the magnetic coupling cannot be avoided due to the mechanical arrangement of resonator, excitation - and probe coil. During the project it turned out to be hard to predict reliably the frequency response by simulations. Thus, a pragmatic approach was selected by measuring a few sample coils and iteratively change the design to the desired specifications. Larger probe coil sizes increase the coil capacitances and the coupling factor. As a rule of thumb for an optimal design, the probe coil should behave like an inductor at the probe frequency, which means the phase lag between voltage and current should be around 90^0. The latter can be determined with the impedance frequency response 48.

By means of COMSOL FEM simulations the magnetic field of the probe coil was computed and optimized. Table 16 in the appendix lists the settings used within the COMSOL simulation. Table 10 summarizes the selected dimensions for the probe coil.

Figure 47 depicts the magnetic field of the probe coil. By means of equations 5.12 and a selected wire diameter of 0.4 mm the probe coil properties referred in table 11 were computed. The selected wire consists of 30 insulated single wires with 40 µm diameter to avoid a resistance increase by the skin effect.

Property	**Value**
Winding Number (N)	300
Inductance (L)	300 µH
Max. Coil Current (I)	0.58 A (RMS)
Skin Depth (δ)	65 µm at 1 MHz

Table 11: Computed properties of the excitation coil

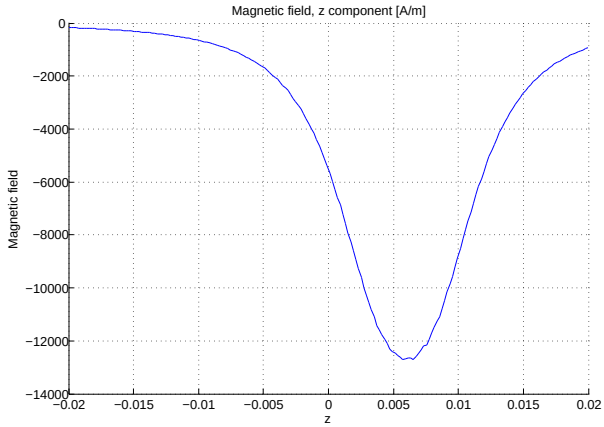

Figure 47: Z-component of the magnetic field of the probe coil along the center line of the coil. The probe coil is located at z=$-10..-2$ mm based on table 10. The resonator structure is located at r=0 mm and z=0 mm.

The inductance was determined as 0.5 mH at $f = 100$ kHz from the impedance frequency response of the experimental probe coil shown by figure 48. At frequencies below 1 MHz the probe coil behaves like an inductor, which is a demanded property at the probe frequency. In the appendix, the impedance frequency response of the probe coil with a series 47 pF capacitance is shown in figure 76 and the frequency response of the transfer function from probe - to excitation coil in figure 77.

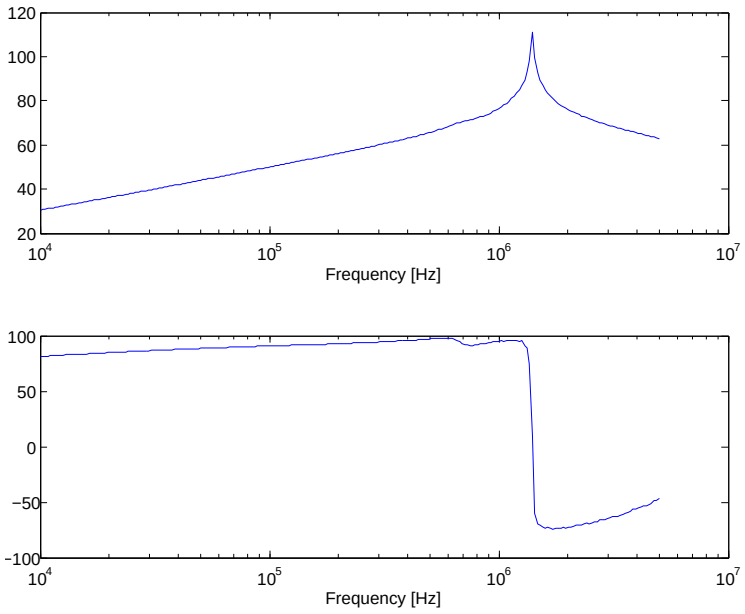

Figure 48: Impedance frequency response of probe coil. Due to the magnetic coupling between probe - and excitation coil, the excitation coil was terminated with a 240 Ω resistor, which is a representative value for the output impedance of the power amplifier.

5.3 ACSC Unit

The amplification-compensation-signal-conditioning (ACSC) unit is an essential element in the read out signal conditioning path. The weak signal from the pick-up coil, induced by the resonator structure motion, is amplified while the much larger signals induced by the excitation and probe field are attenuated significantly. For e.g. the probe signal is seven to eight orders of magnitude larger than the read out signal. The attenuation of excitation and probe signal is important in order to avoid saturation of any electronic amplifier, to maintain high sensitivity of the following lock-in amplifier and to avoid intermodulation distortion. The latter is provoked by even small non linearities present in the read out path and generates an error signal at the probe side band.

Summarizing the requirements to the ACSC unit are as follows:

- Amplification of the read out signal
- Attenuation of excitation -, of probe signal and of error signals at the probe side band
- Very low thermal electronic noise figures
- Highly linear amplification in order to avoid frequency mixing

As explained in earlier sections, the read out is performed on the probe side band and the probe side band is only separated from the probe frequency by the mechanical vibration frequency ($f_m << f_p$). A successful implementation of an analogous band pass filter, which allows a large attenuation of the probe frequency while the read out frequency passes, was assessed to be impossible due to the small frequency separation. A digital realization of the filter cannot be considered, because the large probe signal would decrease the sensitivity due to the quantization property of the analogue to digital converter.

Alternatively, the large probe and excitation signals can be decreased by a compensation strategy. In the presented concept three compensation stages are built in. Figure 49 depicts the compensation and amplification concept of the ACSC unit.

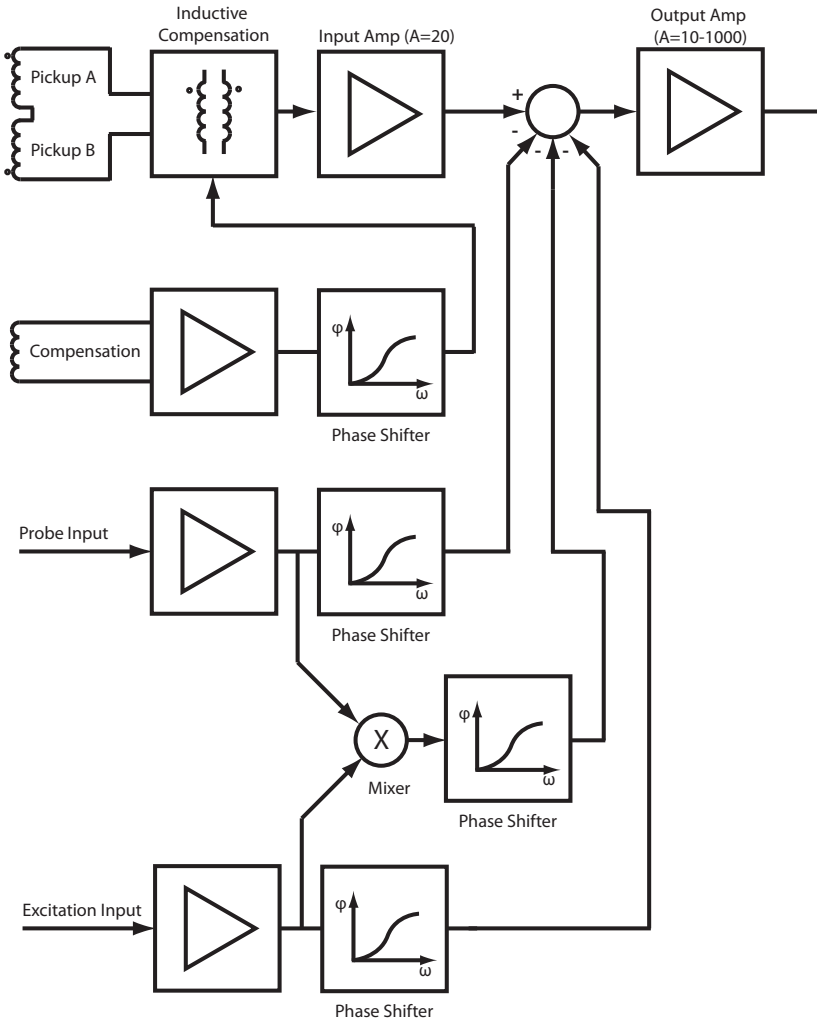

Figure 49: Block schematic of ACSC unit.

The symmetric differential arrangement of the two pick-up coils is called the first compensation stage. They are symmetrically arranged to the probe coil in order to cancel the signal induced by the probe field. Due to experience from the experiments a cancellation of approximately 95% of the probe signal is accomplishable when the pick-up coils are properly symmetrically adjusted to the probe coil by means of for e.g. a micro-positioning device.

The second compensation stage is the inductive compensation which requires the usage of a compensation coil. The compensation coil is a third pick-up coil whose signal can be amplified or attenuated and the phase can be shifted before

it is added to the input signal by means of two magnetically coupled coils. The bandwidth is currently limited to 1 MHz with used coupled coils in the current PCB design. Other coupling coils could increase the bandwidth.

Lastly, the third compensation stage is the electronic op amp adder. The probe signal and excitation signal can be amplified or attenuated and phase shifted before they are fed into the adder. Additionally, there is a mixer circuit which generates a side band signal that is also amplified or attenuated and phase shifted before it is added to the input signal. By means of this stage the probe signal can be further decreased and the excitation signal as well as intermodulation distortion component at the probe side band can be reduced. A compensation effectiveness of about 95-99% was attained for the probe signal depending on the stability of the output of the power amplifier and the drift of the entire setup. For the excitation and probe side band the compensation should be selected not larger than 95% since the phase shifter frequency response and the frequency response of the differential pick-up coil arrangement would alter the read out frequency response for larger compensation values.

It is necessary to focus mainly on the cancellation of the probe signal in the compensation concept because the probe signal amplitude represents the largest part in the pick-up signal.

5.3.1 Differential Input Amplifier

In order to minimize the effect of electronic thermal noise the signal is amplified with a relative large gain of 20 at the first amplification stage. It is clear that the components at the input stage have to be selected carefully to attain a low noise figure. However, large gain amplifiers have, even if excellent high speed op amps are selected, increased distortion figures at the higher harmonics and at the probe side bands. It has to be noted that the probe signal at this stage is still much larger than the read out signal and the intermodulation distortion component at the probe side band generated from the input amplifier is larger than the read out signal. The usage of a following differential stage cancels out the even harmonics and the odd side bands if the two input signal paths are electrically identical.

Due to that a differential input concept has been selected. Another advantage is that interferences coupled to the pick-up coils and connection wires are canceled out as well.

5.3.2 Phase Shifter

The phase shifter is based on a second order all-pass element and consists of two first order all-pass elements connected in series. The transfer function of the first order ideal all-pass element is as follows

$$T(s) = -\frac{sR_1C - 1}{sR_1C + 1} \tag{5.16}$$

Equation 5.16 shows a constant magnitude and a phase lag from $0.. - 180^0$ as frequency response.

Figure 50 depicts the used first order all-pass element. With the potentiometer the required phase lag can be adjusted. It has to be noted, due to noise optimizations a parallel resistor R_2 to the capacitor is required and in order to reduce the capacitive load to the previous op amp stage a series resistor R_3 to the potentiometer is needed. Op amps are susceptible to capacitive loads and too large capacitances lead to instabilities in the op amp circuits. However, both resistors introduce small undesired side effects. The parallel resistor provokes that the gain keeps not constant by varying the frequency or the potentiometer. The series resistor limits the phase adjustment range.

In consideration of the two additional resistors the transfer function changes to

$$T'(s) = -\frac{s(R_1 + R_3)C + \frac{R_1+R_3}{R_2} - 1}{s(R_1 + R_3)C + \frac{R_1+R_3}{R_2} + 1} \tag{5.17}$$

Figure 51 illustrates the relation phase shift and gain to the position of the potentiometer R_1 for one first order all-pass element.

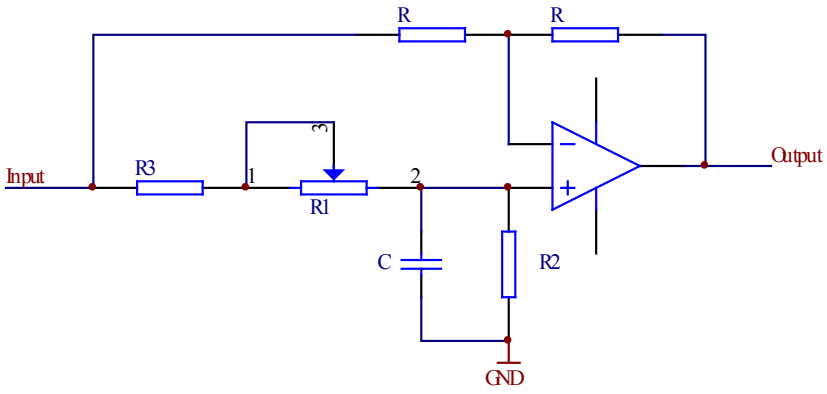

Figure 50: First order all-pass element.

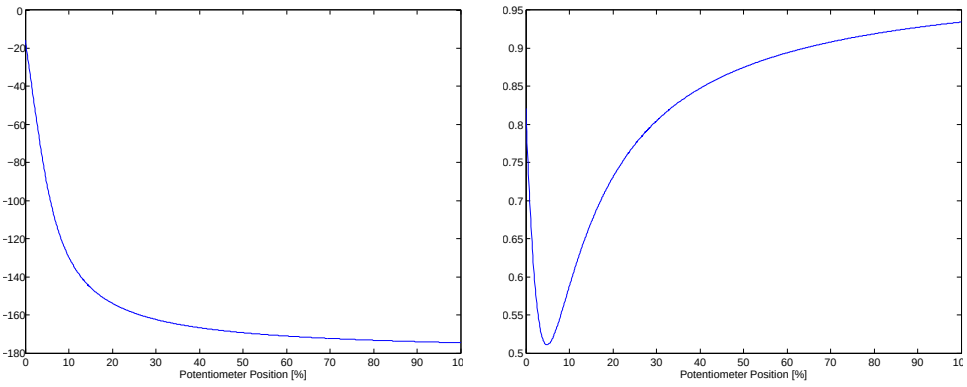

(a) Phase Shift (b) Gain

Figure 51: Phase shifter phase and gain in relation to potentiometer position. Computed at $f = 1\,\mathrm{MHz}$, $C = 220\,\mathrm{pF}$, $R_1 = 10\,\mathrm{k\Omega}$, $R_2 = 1\,\mathrm{k\Omega}$, $R_3 = 100\,\Omega$

5.3.3 Circuit Design

The full circuit design is available in the appendix in sub section C.2. For the amplification path the op amp AD8099 [2] from Analog Devices was selected due to its superior low noise voltage, gain bandwidth product and low distortion figure. The AD8099 is a bipolar transistor op amp and has, thus, higher input noise current specifications in comparison to FET op amps. This has to be considered in the design and the inputs have to be connected to only low impedances to

minimize the effect of the input noise current. Additionally, the AD8099 is not frequency response compensated and requires external compensation capacitors and resistors depending on the feedback gain. This allows, however, to maximize the bandwidth performance of the circuit.

For the probe, excitation and mixer signal paths the op amp LT6200 [30] from Linear Technology was selected because of its lower prize. The LT6200 has a lower gain bandwidth product specification, but is unity gain stable and does not require external frequency response compensation. The probe, excitation and mixer circuitry parts have therefore a lower bandwidth. If required these circuitry parts could be assembled also with the faster AD8099, the current PCB design is prepared for that. More information on bandwidth can be obtained in the following sub section 5.3.5.

In general, achieving low thermal electronic noise figures requires the usage of low ohmic resistors. The noise voltage of the AD8099 or LT6200 is equivalent to that of a 56Ω resistor and especially before the first amplification stage the resistors have to be selected below 56Ω.

5.3.4 Noise Analysis

In this sub section, the spectral density of the thermal noise of the ACSC unit is analyzed and measured. Flicker noise ($1/f$) and other noise sources are not further analyzed, since at the frequency of interest ($f > 100kHz$) thermal noise represents the dominating part.

The noise figures of the thermal noise of the active components are given in their respective datasheets [2]. The dissipated power in a resistor due to thermal noise is given by the Johnson Nyquist relation

$$P = 4k_B T \Delta f \tag{5.18}$$

and one obtains for the noise voltage

$$U_n = \sqrt{4k_B T R \Delta f} \tag{5.19}$$

whereas k_B is the Boltzmann constant, T the absolute temperature, R the resistance in ohms and Δf the bandwidth.

As the individual sources are not coherent the total output noise is sum of the squares of the individual sources multiplied with their transfer function.

$$U_{out} = \sqrt{\sum_n (U_n T_n)^2} \tag{5.20}$$

whereas U_n is the noise voltage of the single source and T_j is the transfer function to the output. If one noise source contribution is less than one fourth of the maximum value it can be neglected due to the summed squares of equation 5.20.

The spectral density is

$$u_{out} = U_{out}/\sqrt{\Delta f} \tag{5.21}$$

The procedure for noise analysis is to add for each component noise equivalent sources into the circuit diagram, which model the noise behavior, and then the components are then thought to be as noise free. By applying equation 5.20 the contribution of each noise source and the total output noise can be calculated. Figure 52 illustrates a noise equivalent schematic for the input stage. In the appendix in sub section C.3 further noise equivalent circuit diagrams are available for other circuit parts.

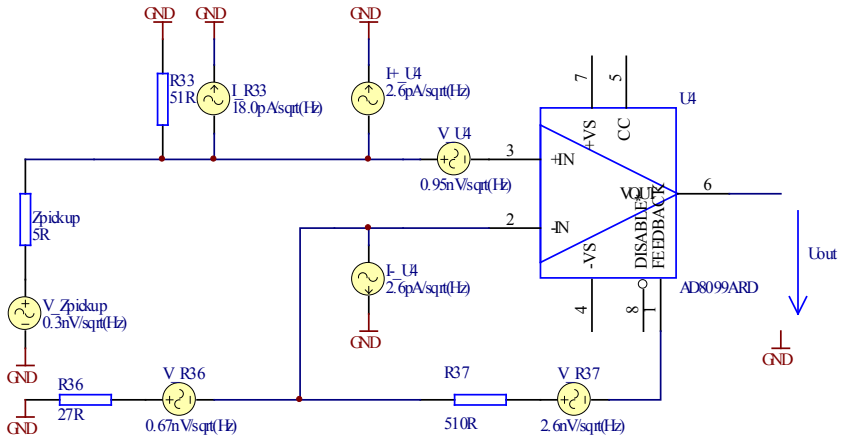

Figure 52: Noise equivalent circuit for the input stage.

Table 12 summarizes the predicted and measured spectral densities of the thermal noise of the output of the ACSC unit. Considering the fact that the noise figures were computed in a simplified model and the situation on a real printed circuit board is more complex, it can be concluded that the predicted values are in rather good agreement with the measured values.

Figure 53 shows the spectral density of the thermal noise at the output of the ACSC unit.

More noise measurements are available in the appendix in sub section C.4.

Input	Prediction	Measurement
Single Ended	$1.85\,\mathrm{nV/Hz^{1/2}}$	$2.5\,\mathrm{nV/Hz^{1/2}}$
Differential	$2.3\,\mathrm{nV/Hz^{1/2}}$	$3.5\,\mathrm{nV/Hz^{1/2}}$

Table 12: Spectral densities of the thermal noise of the output of the ACSC unit. All values are referred to the input. The inductive compensation circuitry is not considered and by-passed.

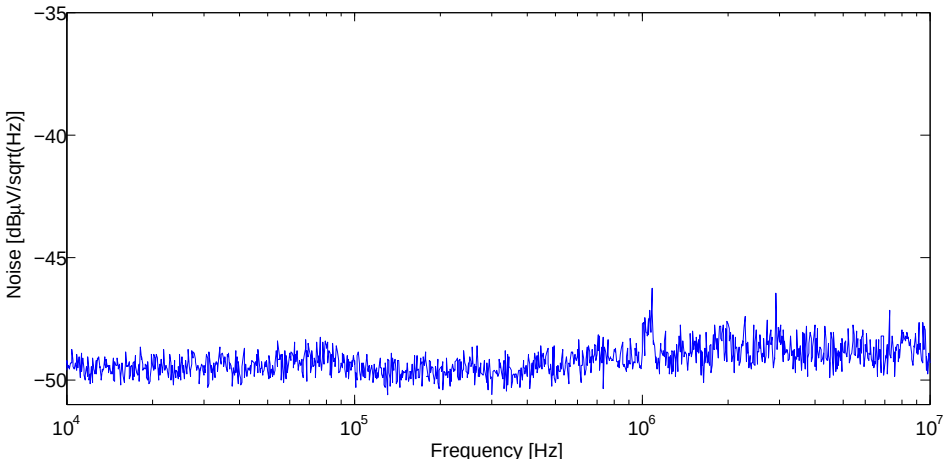

Figure 53: Spectral density of the thermal noise at the output of the ACSC unit. The ACSC unit is used in differential input configuration and the inputs are open. All values are referred to the input. The inductive compensation circuitry is not considered and by-passed.

5.3.5 Frequency Response

The employed AD8099 op amp from Analog Devices [2] allows a bandwidth of up to 100 MHz of the ACSC unit circuit. In the compensation circuitry part another op amp LT6200 from Linear Technology [30] was implemented due to its lower prize. For the compensation circuitry a bandwidth of 20 MHz is accomplished with the usage of the LT6200. However, if needed, the compensation circuitry could be equipped as well with the faster AD8099 in order to increase the bandwidth. In the experimental setup, however, it turned out a bandwidth of 10 MHz is favorable to achieve a sufficient sensitivity. Therefore, the bandwidth was limited to 10 MHz by means of the frequency compensation capacitors of the op amps AD8099. Nevertheless, if required larger bandwidths are possible with the ACSC unit circuit design. Figure 54 shows the measured frequency response.

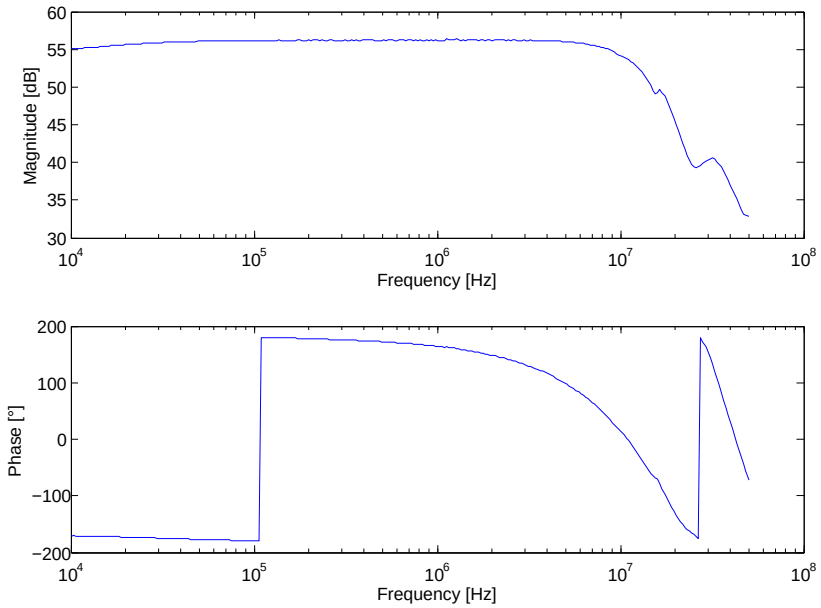

Figure 54: Frequency response of the transfer function input to the output of the ACSC unit. The inductive compensation circuitry is by-passed.

In the appendix in sub section C.5 the frequency response with inductive compensation circuitry is indicated.

5.4 Results

In the following section, several results from the wireless magnetic read out experiments are presented. A top-down approach has been selected, the first experiment starts with a larger device and then, gradually the size is decreased by each experiment. It is known from the simulation section 3, the read-out amplitude decreases when the size of the resonator structure decreases and, hence, the read out becomes more demanding by decreasing the structure size.

In all the performed read out experiments the first side band showed its favorable read out behavior corresponding to the predictions of the section simulation 3. Amplitude overshoots and phase changes can be observed at the higher harmonics as well, but the accentuation is much lower. As a proof for the correctness of the magnetic read out, the resonator structure was measured with the laser vibrometer or the planar motion analyzer. In oder to compare both read out methods, it was necessary to normalize the frequency response at the resonant frequency. So, the magnitude was normalized to one and the phase to zero at resonance. While the laser vibrometer read out delivers deflection amplitude and phase of the resonator structure, the magnetic read out is not so practical yet and measures induced voltage amplitude and phase in the pick-up coils. However, the magnetic read out could be related to the resonator deflection response via a constant factor and phase correction . The relation is, in fact, not so easy and straightforward definable because it depends on a number of parameters like the phase lag between excitation - and probe signal, the magnetization characteristic of the resonator material, the intermodulation distortion component at the side band, the size and geometry of resonator structure and pick-up coil and the gap between resonator structure and pick-up coil. Unfortunately, the phase lag between excitation - and probe signal is not known and cannot be set to a constant value within the used lock-in amplifier. It is randomly determined when the read out is started. Therefore, the read out response is normalized to achieve a meaningful comparison between the two read out methods.

5.4.1 Effect of Distortion on Read Out Response

Distortion of the excitation and the probe signal induced in the pick-up coils arise from non-linearities present in the experimental setup and consist of higher harmonics called harmonic distortion and side bands called intermodulation distortion. Any non-linearity has in its representation as Taylor progression terms of higher orders with multiplications. Multiplications shift frequencies and generate, thus, higher harmonics and also side bands. It is obvious, any side band signal generated from non-linearities is not desirable for the read out since it represents an error signal.

The intermodulation distortion and harmonic distortion are mainly generated by the power amplifier. Another significant source is the non-linear magnetization characteristic. A large fraction of the intermodulation distortion component (IDC) present at the first side band can be compensated by the differential pick-up coil arrangement and the electronic compensation within the ACSC unit. Yet, a minor part is still present in the read out signal and can have interfering effects on the read out. The consequences are, in fact, not so obvious and are hard to predict only by intuition. In the following, the effects are analyzed by using a second order ODE system to model the resonator structure response and by adding up to of a constant signal representing the IDC. The frequency is swept over a band centered at the resonant frequency and the IDC is kept constant in amplitude and phase over the frequency range. In the experiment, amplitude and phase of the IDC might change slightly over the swept frequency range, but this is, however, neglected in the following theoretical investigation. It shall be remarked that the experimental observations match well to the results presented here.

The read out signal of a resonator structure is modeled with the following transfer function

$$\Sigma(s) = \frac{\omega_0^2}{s^2 + 2\delta\omega_0 s + \omega_0^2} \tag{5.22}$$

where ω_0 represents the resonant frequency of the undamped system and δ

the damping ratio. The resonant frequency of the damped system is

$$\omega_R = \omega_0\sqrt{1-2\delta^2} \tag{5.23}$$

if $\delta < \frac{1}{\sqrt{2}}$. The quality factor is related to the damping ratio

$$Q = \frac{1}{2\delta} \tag{5.24}$$

A quality factor of 20 is selected to model an appropriate resonant behavior of the resonator structure. It results a damping ratio $\delta = 0.025$ and a resonant frequency of $\omega_R = 0.9994\omega_0$.

Figure 55 depicts the MATLAB simulation of the read out frequency response for three different IDC amplitudes and figure 56 illustrates the MATLAB computations for three different IDC phases. Figure 55 shows that the amplitude response can change from a nicely shaped resonant overshoot to a step similar form for higher IDC amplitudes. This results from either constructive or destructive superposition of the two signals. Rather unexpectedly, the frequency of the peak shifts by increasing the IDC amplitude. This leads to an alteration of the detected resonant frequency if the resonant frequency is determined via the peak amplitude. Even for moderate IDC levels, the detected resonant frequency may deviate up to one percent from the correct resonant frequency. If only the relative change of the resonant frequency is relevant like in a mass change sensor system, the resonant frequency deviation is not an issue. The IDC affects even more the phase response as illustrated by figure 55 and figure 56. Figure 56 shows the influence of the IDC phase to the read out response.

In the experiment, similar responses as indicated by figure 55 and figure 56 were observed. Usually, the read out response could be improved from a poorly shaped curve to a nicely formed resonant overshoot by tuning the level of the DC magnetization and the side band compensation of the ACSC unit. Yet, the latter requires a sufficiently large resonator structure signal to IDC ratio. The effect of the DC magnetization on the IDC was experimentally observed and not studied

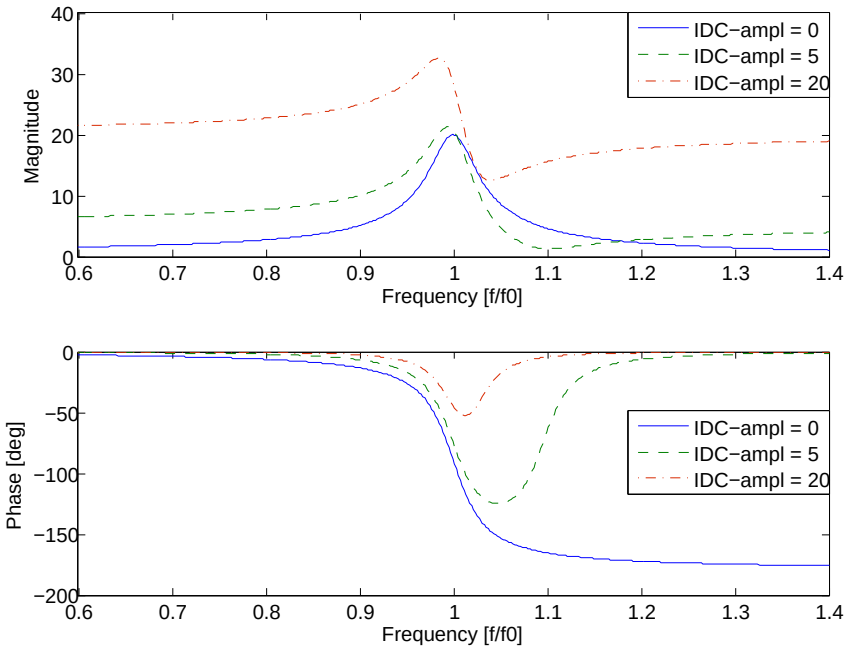

Figure 55: Effect of IDC to the read out frequency response with three different IDC amplitudes (IDC phase = 0).

in detail. It is assumed, since the DC magnetization determines the working point on the magnetization characteristic and the magnetization characteristic is non-linear, that the working point has an influence on the level of the non-linearity. This is obvious for a working point close to the saturation, which represents a large non-linearity. However, in the linear regime of the magnetization characteristic it could be observed that the IDC level could be decreased by increasing the DC magnetization.

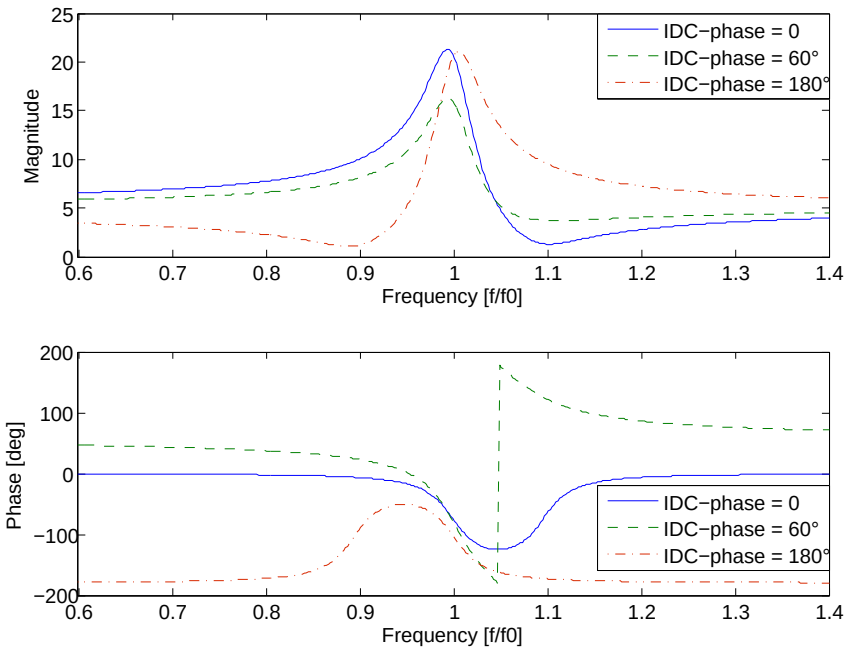

Figure 56: Effect of IDC to the read out frequency response with three different IDC phases (IDC amplitude = 5).

5.4.2 Large Cantilever

A cantilever 6 mm x 3 mm x 30 µm is excited out-plane and read out. The cantilever is made of the amorphous, ferromagnetic alloy glass ribbon 2826MB [32] from Metglas, Inc. Figure 57 illustrates the cantilever. The cantilever was cut out of a ribbon of 2826MB [32] and attached to a 200 µm thick polycarbonate anchor. Maximum deflections at resonance of up to 20 µm were detected with the laser vibrometer read out.

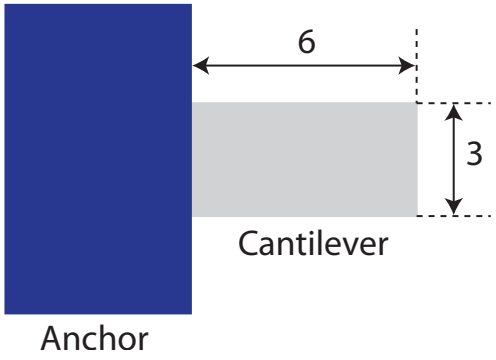

Figure 57: Cantilever 6 mm x 3 mm x 30 µm made of the ferromagnetic alloy 2826MB [32] from Metglas, Inc.

Figure 58 depicts the measured frequency response of the magnetic and laser vibrometer read out. As figure 58 shows, the resonant peak between magnetic and laser vibrometer read out is separated by approximately 15 Hz, which represents 3% of the resonant frequency. It is assumed that the deviation is mainly due to the different excitation setups. In case of the laser vibrometer read out a compact setup has to be used due to the limited available space under the laser vibrometer head. The compact setup employs permanent magnets for the generation of the DC magnetic field. However, the generated DC field is not perfectly uniform and smaller field gradients are present, which provoke static forces acting on the cantilever. A static force may affect the resonant frequency of the cantilever. In case of the magnetic read out, the DC magnetic field is generated by a pair of large DC coils. Large electromagnets generate a more uniform magnetic field at the position of the cantilever. Apart from static forces, other parameters might influence the resonant frequency like the air temperature and humidity. As shown in the previous sub section 5.4.1, the IDC at the read out side band may

shift the resonant peak. Yet, sometimes even practical reasons like small changes in the anchoring due to temperature changes influence the resonant frequency, when plastic anchors are used. Comparing magnetic and laser vibrometer read out, figure 58 shows a similar shape of the magnitude of the resonant overshoot and the shape of the phase change matches as well.

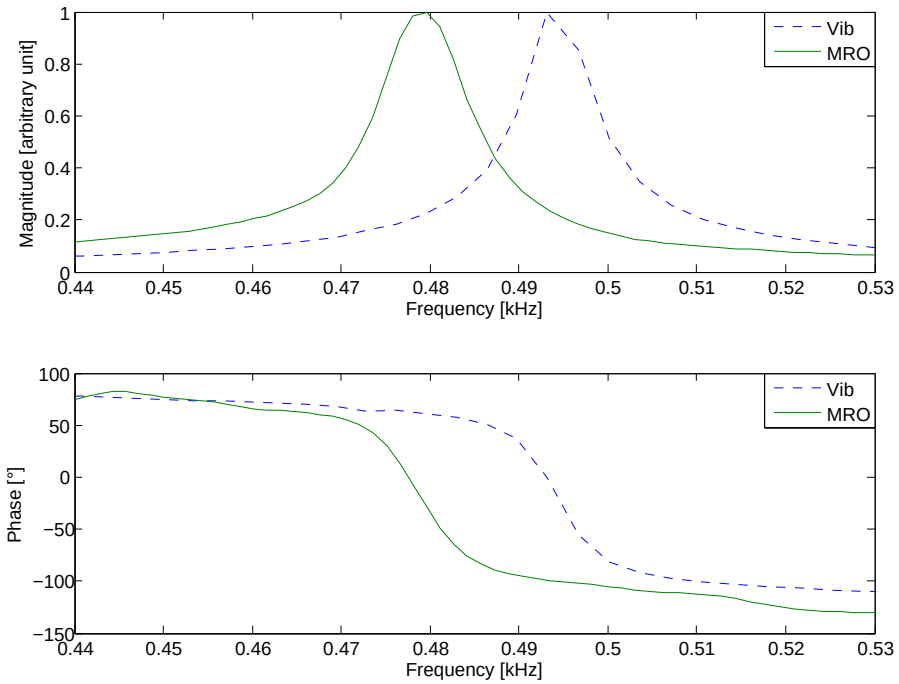

Figure 58: Magnetic read out (MRO) and laser vibrometer read out (Vib) of cantilever 6 mm x 3 mm x 30 µm vibrating in out-plane direction.

5.4.3 Out-Plane Resonator

The second presented experiment is the read out of a vertically vibrating resonator with a nickel die of 1 mm x 1 mm x 50 µm which serves as actuation and read out element. The resonator was originally fabricated for another purpose than this master project and was used as an ultrasonic transducer [18]. For the magnetic read out, the gold base frame acts like a shield and lowers the read out performance. Therefore, the gold base frame was removed for this read out experiment. With the laser vibrometer read out deflection peaks of up to 2 µm were observed at resonance.

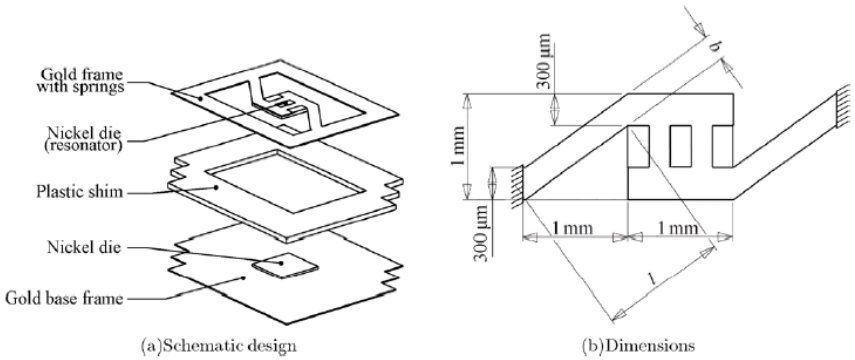

Figure 59: Schematic design of resonator with a nickel die 1 mm x 1 mm x 50 µm. Vibration direction out-plane.

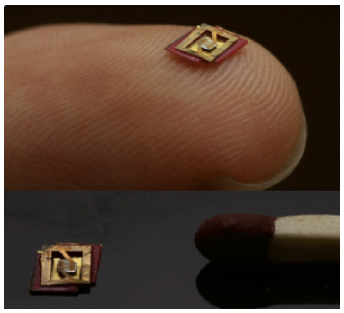

Figure 60: Picture of resonator of figure 59.

Figure 61 depicts the measured frequency response of the magnetic and laser vibrometer read out. The magnetic read out was performed at the first side band of the probe frequency. Again, similar to the previous case 5.4.2, figure 61 shows

a separation of the resonant peaks by approximately 30 Hz between magnetic and laser vibrometer read out. The 30 Hz represent less than 1% of the resonant frequency. Concerning the reasons, the same assumptions can be made as in the previous case 5.4.2. Good agreement is observed between the shapes of the magnitude overshoot and phase change at resonance.

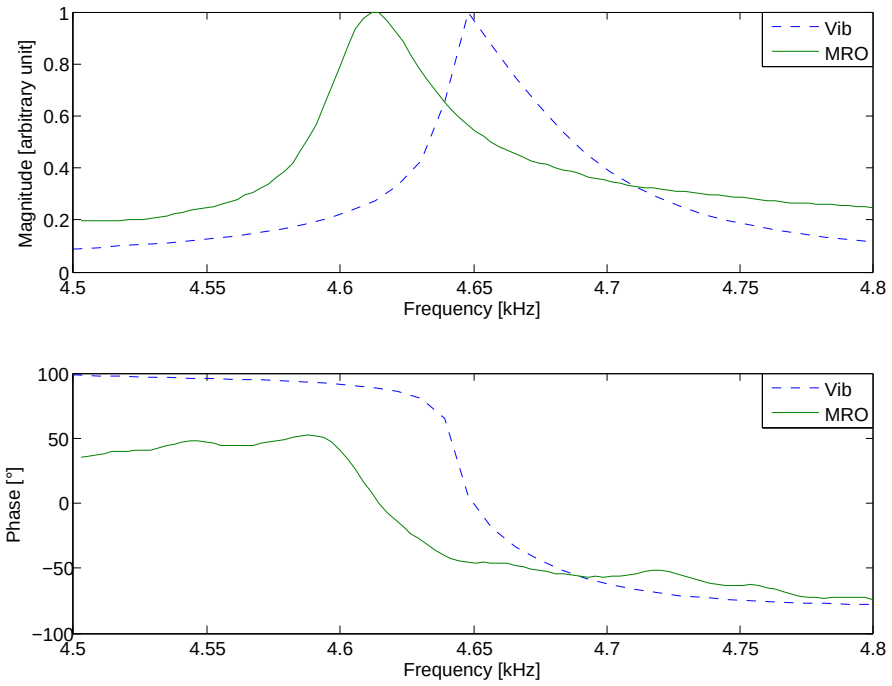

Figure 61: Magnetic read out (MRO) and laser vibrometer read out (Vib) of resonator 1 mm x 1 mm x 50 µm. Vibration direction out-plane.

In the appendix the following responses are shown: figure 92 at the first harmonic, figure 93 at the second harmonic, figure 94 at the third harmonic and figure 95 at the second side band. Rather lower deflections at the resonant frequency are visible in the response diagrams of the first -, second harmonic and second side band. Indeed, the deflections are rather small compared to the resonant characteristic shown at the first side band. This emphasizes again the favorable property of the first side band for the read out.

5.4.4 Magnetostrictive Resonator

This experiment shows the successful read out of a magnetostrictive sensor made of amorphous, ferromagnetic alloy glass ribbon 2826MB [32] from Metglas, Inc. Figure 62 illustrates the sensor. The main advantages of these type of sensors are to be purely passive, the ability for wireless actuation and read out and the fact that the ribbon material can be bought cheaply. Hence, cost efficient passive sensors with high sensitivity can be fabricated rather easy.

In contrast to the first experiment 5.4.2, where the same magnetostrictive material was used, the sensor used here is free standing and has no clamped ends. When exposed to an AC magnetic field, the sensor deforms following the exciting AC magnetic field due to the magnetostrictive property of the material (see figure 62). An acoustic in-plane wave is excited and travels between the ends of the ribbon. At resonance, the wave length $\lambda = n \cdot 2L$, where L represents the length of the ribbon and n a positive integer. Longitudinal and shear waves can be excited and show different resonant frequencies because of their different phase velocities. In this experiment, the read out of the resonance of the longitudinal wave is shown. The longitudinal wave causes a length change of the sensor. The magnetic force can be enhanced if a superposed DC magnetic field is used. The DC magnetic field magnetizes the sensor and, like in the case of the resonator structure magnetization, the acting magnetic force on the body is increased. By means of a pick-up coil the vibration can be sensed. Since the read out at the first side band had been proven to be successfull in the previous experiments, the frequency response of the first side band was used to detect the resonant frequency, .

The resonant frequency for the case of the longitudinal waves is

$$f_R = \sqrt{\frac{E}{\rho(1-\nu^2)}}\frac{n}{2L} \tag{5.25}$$

where E is the Young's modulus, ρ the density, ν the Poisson's ratio, L the length of the sensor and n a positive integer.

A sensor size of length L= 3 mm, width W= 2 mm and thickness th = 30 µm

was used. One obtains for the first mode resonant frequency $f_R = 718\,\text{kHz}$ by using equation 5.25 and the material properties specified in table 13.

Property	Value
Young's Modulus	110 GPa
Poisson's Ratio	0.5
Density	7900 kg/m^3

Table 13: Material properties of 2826MB [32] from Metglas, Inc. The Poisson's ratio was taken from [28].

Figure 62: Magnetostrictive sensor made of ferromagnetic alloy ribbon 2826MB from Metglas, Inc. Dimensions of sensor 3 mm x 2 mm x 30 µm. Length change of 2δ due to magnetostriction.

Figure 63 shows the magnetic read out of the magnetostrictive sensor. A resonant frequency of 729 kHz can be determined from figure 63. The deviation to the predicted resonant frequency is only 1.5%. The tolerance in the sample length and uncertanties in the values of the material properties can be identified as potential reasons for the deviation.

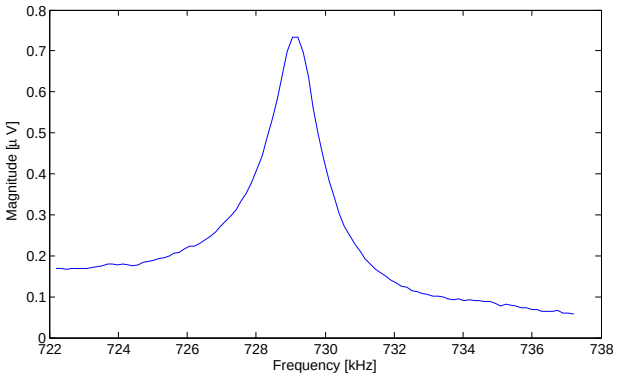

Figure 63: Magnetic read out of magnetostrictive sensor made of ferromagnetic alloy ribbon 2826MB from Metglas, Inc. Dimensions of sensor 3 mm x 2 mm x 30 µm.

5.4.5 CoNi In-Plane Plate Resonator Row

The fourth presented experiment deals with the read out of a row arrangement of CoNi plate resonators as depicted by figure 38. The six plates are excited in-plane and reach a maximum deflection amplitude of $10 - 20\,\mu m$. The plates have a dimension of $400\,\mu m$ x $400\,\mu m$ and are suspended by a spring with dimension $200\,\mu m$ x $11\,\mu m$. The springs are clamped to an anchor bar. The thickness is $6\,\mu m$ in the center of the plate. At the edges of the plate and at the spring the thickness is larger due to the electroplating process.

Figure 64 shows the frequency response measured with the magnetic read out and the planar motion analyzer. It has to be remarked, that in case of the magnetic read out, the measured signal is a superposition of the signals induced by the individual resonator plates. Figure 64 shows three peaks, the largest at $f = 6.04\,kHz$ comes from plate six and is compared with the planar motion analyzer read out. The six plates arranged in the row have all different resonant frequencies due to variations in the spring thickness resulted from the non-uniformity of the electroplating process. In figure 64 the peaks, thus, refer to different plates. The level of the read out amplitude depends on the alignment of resonator structure to pick-up coil and, therefore, the peak of the resonator structure with good alignment is emphasized in the read out as shown by figure 64. Since the read out signal is a superposition of the induced signals of the individual plates, which may have different amplitudes and phases, the resulting frequency response can be a constructive or destructive superposition. In general, the plate with good alignment should induce at resonance a much stronger signal than the others and should be, thus, clearly detectable in the frequency response. The latter applies to the magnitude and phase response.

Similarly to the two previous cases, there is a small deviation of about $15\,Hz$ between the detected resonant frequencies of the two read out methods. Concerning the reasons, the same assumptions apply as in section 5.4.2. Again, good agreement is found between the shapes of the resonant overshoot measured with the magnetic read out and the planar motion analyzer. Since the planar motion analyzer does not provide phase information, the phase cannot be compared.

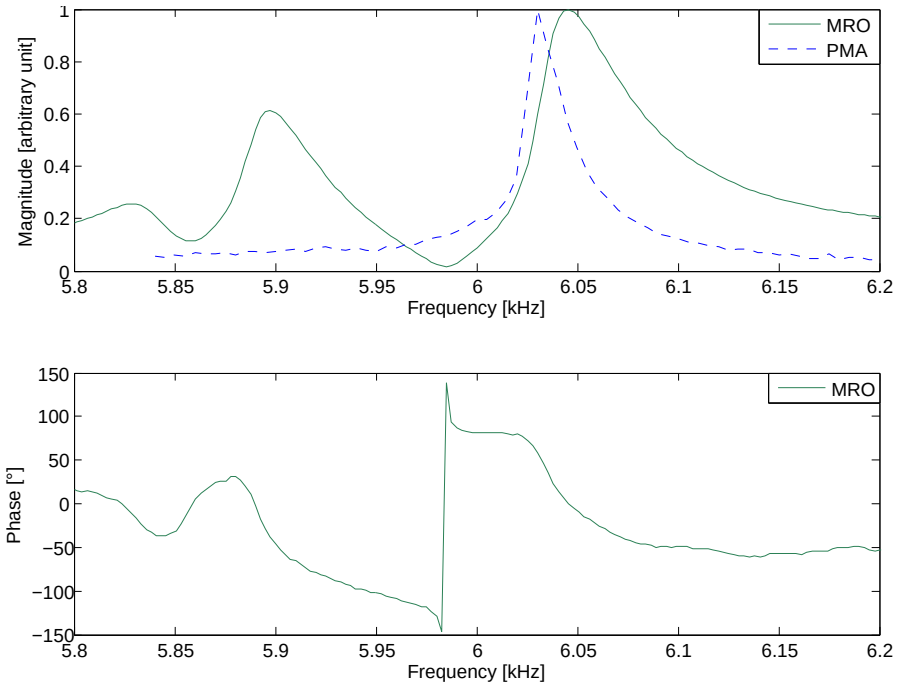

Figure 64: Magnetic read out (MRO) and planar motion analyzer read out (PMA) of a row of plate resonator structures 400 µm x 400 µm x 6 µm. Vibration direction in-plane.

By assuming a plate deflection amplitude of $\hat{x}_d = 20\,\mu\text{m}$ at resonance and a probe field amplitude magnetization of $\hat{M}_z = 2\,\text{kA/m}$, one obtains for a numerical simulation with equation 3.40 a read out amplitude of $U_{SB} = 64\,\text{nV}$ at the resonant frequency. The assumed plate deflection and probe magnetization values represent reasonable values for the used experimental setup and plate resonator design. In the experiment, the measured resonant amplitude was 1.94 µV. The larger measured amplitude is explained by the in-plane magnetization component of the ferromagnetic plate resonator. The above numerical simulation considered only the magnetization component in out-plane direction. Though, the probe magnetic field is mainly directed in out-plane direction at the center line of the coil, there is a small radial component especially if the plate resonator is placed slightly out of the center line. In in-plane direction the ferromagnetic plate is easier magnetized due to the shape anisotropy and, thus, a small in-plane magnetic field component can generate an in-plane magnetization component which is even larger than the out-plane component. There is no shape anisotropy present for superparamagnetic materials like the magnetic nanoparticle polymer composite

and the in-plane magnetization component for these type of materials is much lower.

In the appendix, figure 96 shows another read out of the same structure of plate resonators. This time, the alignment of the pick-up coil was changed and peak four is emphasized.

5.4.6 CoNi In-Plane Plate Resonator Sensor

The last experiment shows the usage of an in-plane plate resonator as sensor. Figure 38 depicts the arrangement, but only plate 6 was used and the other plates were removed. The plate has a dimension of 400 µm x 400 µm x 12.5 µm and is suspended by a spring with dimension 200 µm x 11 µm x 14.5 µm. The plate resonator reaches a maximum deflection amplitude of 20 µm.

Figure 65 shows the frequency response measured with the magnetic read out and the planar motion analyzer. Similar to the previous cases, there is a very small deviation of about 8 Hz between the detected resonant frequencies of the two read out methods. Concerning the reasons, the same assumptions apply as mentioned in section 5.4.2. Satisfactorily agreement is also found between the shapes of the resonant overshoot between magnetic read out and planar motion analyzer read out. The planar motion analyzer does not provide phase information.

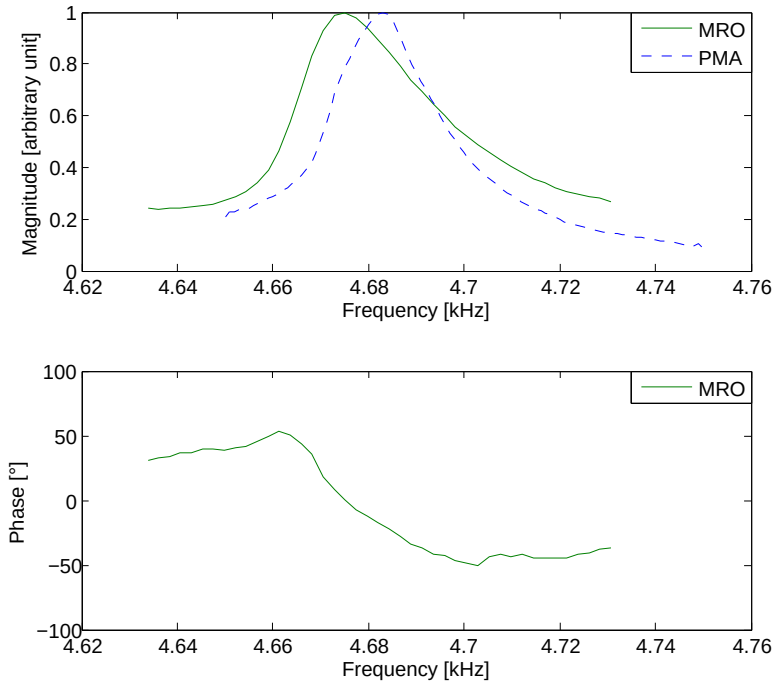

Figure 65: Magnetic read out (MRO) and planar motion analyzer read out (PMA) of plate resonator structure 400 µm x 400 µm x 12.5 µm. Vibration direction in-plane.

On top of the same resonator a mass consisting of 950 polystyrene beads with a mean diameter of 6 µm was applied, which corresponds to a weight of 113 pg. Figure 66 shows the loaded plate with the polystyrene beads.

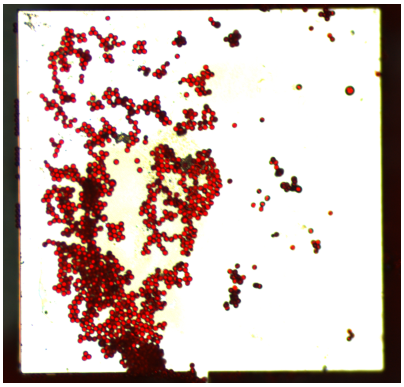

Figure 66: 950 polystyrene beads with a diameter of 6 µm are applied as load on the plate. The added mass corresponds to 113 pg.

Figure 67 shows the frequency response of the plate resonator with load and without load. The frequency response was measured with the magnetic read out. A clear shift of the resonant frequency of about 82 Hz and a lower quality factor for the loaded case can be detected . The lower quality factor is visible on the broadened resonant overshoot and is because of the increased fluidic resistance, which is caused by the beads on top of the plate. The beads have a diameter of 6 µm and increase the damping due to their size and shape.

The shift in the resonant frequency can be assigned to the additional mass, the lower quality factor and to a temperature effect. It was observed in the experiments that the resonant frequency depends on the temperature. This effect is presumably due to a change of the mechanical properties of the anchor material. The stress strain curve of the SU-8 anchor material is a function of the temperature. In addition, the fluidic resistance depends on the air temperature. During the experiment, the temperature was controlled by starting the experiment from room temperature and by measuring the actuation coil temperature. Some temperature variation at the resonator, however, cannot be avoided. An eigenmode analysis with COMSOL showed a frequency change of 10 Hz for the applied mass of 113 pg. It has been assumed that the deviation in the detected

frequency shift can be assigned to inaccuracies in the mass determination, to the temperature effect and to the lower quality factor.

For a frequency shift of 10 Hz, it results a sensor sensitivity of $S = 88.5\,\mathrm{Hz/ng}$.

The sensors mass resolution depends on the resonator sensitivity, the resonator quality factor and the ability of the system to determine the resonant frequency from the frequency response. A high quality factor is demanded to obtain a high resolution of the resonant frequency detection. In this case with a quality factor of about $50 - 100$, a cautious assumption is that the resonant frequency can be resolved in the frequency response to approximately 10 Hz. This yields a mass resolution of $71\,\mathrm{ng/cm^2}$, which represents a good value in the range of $10\,\mathrm{ng/cm^2}$ - $1\,\mu\mathrm{g/cm^2}$ reported for microcantilevers [10].

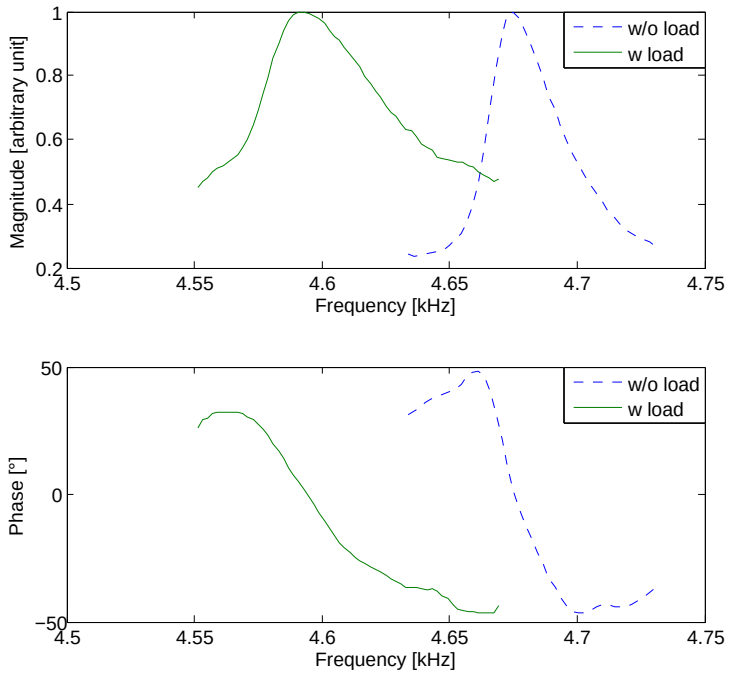

Figure 67: Magnetic read out of plate resonator structure with load and without load. 950 polystyrene beads are applied as load and the added mass corresponds to 113 pg.

As next, the beads were removed from the plate resonator and the plate resonator was built into a flow chamber, which was filled with distilled water. Figure 68 shows the frequency response of the in-plane plate resonator in water

and air. Thereby, the successful operation of the in-plane resonator in water was demonstrated. As expected, a lower quality factor was observed in water when compared to air. This is due to the higher viscosity of water, which results in a higher damping factor. Additionally, a shift in resonant frequency was detected. The shift in the resonant frequency can be assigned to the lower quality factor, to the temperature effect and it has been assumed, that the immersion in water may change the stiction between the CoNi/Au - and SU-8 layer and, thus, changes the resonator suspension.

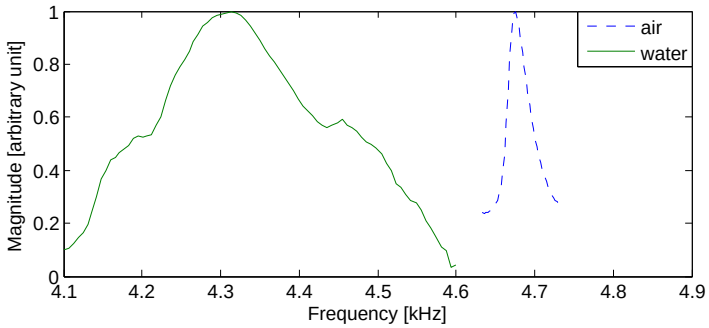

Figure 68: Magnetic read out of plate resonator structure in water and air.

5.5 Limitations of the Experimental Setup

In section 5.4, the successful read out of several resonator structures with different designs and dimensions were presented. However, there are limitations within the current experimental setup, which inhibit the read out of smaller structures and especially the read out of magnetic nanoparticle polymer composite structures.

Limitations arise from the following properties:

- Intermodulation distortion component at the probe side band
- Thermal electronic noise
- 1 MHz bandwidth of the power amplifier
- 1 MHz bandwidth of the probe coil

The IDC at the side band represent the main limitation at the moment. An approximate IDC amplitude of a few hundred nano volt was measured at the first side band even when the compensation in the pick-up coil and ACSC unit was optimally tuned. The IDC amplitude depends on a variety of parameters, but is as expected clearly a function of excitation and probe field amplitude. A higher compensation is unfortunately not possible because the IDC amplitude shifts as a function of the swept excitation frequency and shifts also due to other effects. Main contributor to the current IDC level is the power amplifier and its non-linearity in the transfer characteristic, respectively. Another contributor is the non-linearity in the magnetization characteristic of the resonator material. However, the magnetic material generates far less IDC compared to the power amplifier.

The thermal noise of the experimental setup is approximately $3.5\,\mathrm{nV/Hz^{1/2}}$ as presented in the ACSC unit section 5.3. If the IDC level can be reduced, thermal noise will represent the next problem to overcome. Yet, by using a lower bandwidth at the lock-in amplifier, the effect of the thermal noise can be reduced at the cost of a slow sweep time.

The bandwidth of the experimental setup is currently limited to 1 MHz because of the power amplifier and the probe coil. Increasing the bandwidth and

the probe frequency is favorable in order to increase the read out amplitude and to decrease the effects of the IDC and the thermal electronic noise. For a higher bandwidth, the usage of a power amplifier with a higher bandwidth and the design of a frequency optimized probe coil is required.

For a MPC lateral resonator with plate dimension of 300 µm x 300 µm x 2.5 µm, an optimistic computation with equation 3.40 yields a read out amplitude of 2.7 nV. The read out amplitude was computed with an optimal pick-up coil alignment, a resonator plate probe magnetization $M_z = 0.25\,\mathrm{kA/m}$, a deflection amplitude $x_d = 10\,\mu\mathrm{m}$, a probe frequency $f_p = 800\,\mathrm{kHz}$ and a plate to pick-up coil gap $z_p = 300\,\mu\mathrm{m}$. The selected resonator plate probe magnetization $M_z = 0.25\,\mathrm{kA/m}$ is representative for the used experimental setup and a MPC nanoparticle volume concentration of 4%.

In consideration of the IDC amplitude of a few hundred nano volt, the 2.7 nV read out amplitude from the resonator is too low for a successful read out. However, if the IDC amplitude can be decreased, the successful read out of MPC resonators is in reach and feasible. Additionally, it is favorable to increase the read out amplitude by for example increasing the probe frequency.

6 Summary and Contributions

A magnetic resonator sensor system with wireless magnetic actuation and wireless magnetic read out was designed. Resonator structures made of cobalt nickel (CoNi) and magnetic nanoparticle polymer composite (MPC) were employed. The CoNi structures were fabricated in this work, while the MPC structures were provided by the micro- and nanosystems group of ETH.

For the CoNi structures the process of the MPC structures was adopted and the MPC layer was exchanged by a CoNi layer. The wafer was patterned with a first photolithography step and then CoNi was electroplated as the structural layer on the Cu/Si wafer. The Cu layer served as the release layer. Afterwards, the anchor layer was applied as a SU-8 layer formed by a second photolithography step. The devices were released by etching the Cu layer. One of the major problem to overcome was the low adhesion between CoNi and SU-8. By using a gold layer as adhesion layer and using OmniCoat as adhesion promoter, the adhesion could be sufficiently improved. The structural layer was nicely preserved in CoNi. A few structures were characterized in the in-plane vibration-mode with the planar motion analyzer.

The read out principal is based on the frequency response of the resonator structure. While the resonator structure is excited over a frequency band including the resonant frequency, the deflection of the resonator structure is monitored in amplitude and phase. At resonance, the amplitude and the phase change reaches a maximum. Both effects can be used to determine the resonant frequency. In order to increase significantly the sensitivity and signal to noise ratio, a probe signal was applied, which oscillates at a much larger frequency than the excitation frequency. The vibration of the resonator structure induces a side band at the probe frequency and the side band was deployed for the read out. Within the experiments the beneficial usage of the probe signal was demonstrated and the response of the resonator structure could be observed in a higher quality at the side band.

A specific simulation model was developed to reliably predict the amplitude of the read out. The model is based on a "magnetic charge" model and analyti-

cal field equations of that. An analytical equation of the side band read out was derived. It shows the favorable properties of the side band, the amplitude is amplified by the probe frequency and is a linear function of the resonator structure deflection. The phase of the resonator structure deflection is accordingly perceivable in the side band. Furthermore, analytical approximation equations for the different experimental cases in-/out-plane vibration and in-/out-plane magnetization were provided. The derivative magnetic field can be used to determine the optimal placement and geometry of the pick-up coil. It turned out, that a micro sized coil only slightly outperforms the macro sized coils at the given gap between resonator structure and pick-up coil. The gap is determined by the flow channel arrangement. Numerical simulations with parameter sweeps were performed to analyze the effects of the physical parameters. At the bottom line, the simulation revealed, the read out amplitudes of magnetic nanoparticle polymer composite structures (MPC) are very low ($1 - 5\,\mathrm{nV}$) and the optimal alignment of pick-up coil to resonator structure is essential.

The magnetic field of the coils for the experimental setup was optimized with COMSOL FEM simulations. However, the frequency response of the coils had to be experimentally optimized by fabricating some samples. For the amplification and compensation of the pick-up signal a specific amplification-compensation-signal-conditioning (ACSC) unit was designed with very low noise figures, a highly linear transfer characteristic and the capability for signal compensation.

In the experimental phase several resonator structures were read out with the wireless magnetic read out. The experiment was started with the read out of a larger structure made of full magnetic material and continued then with the read out of smaller-sized structures. A CoNi in-plane oscillating structure with a dimension of $400\,\mu\mathrm{m}$ x $400\,\mu\mathrm{m}$ x $12\,\mu\mathrm{m}$ was succesfully read out and the deployment as a mass sensor was demonstrated. Polystyrene beads were applied to the resonator structure as mass load. A sensitivity of $88.5\,\mathrm{Hz/ng}$ was revealed by the experiment. The possible operation of the same structure in water was shown and indicates that the in-plane resonators can be used in liquids. The vibrating structure in water was read out with the magnetic read out. MPC structures could be, however, not read out yet successfully due to the level of the

intermodulation distortion component at the side band, which is mainly caused by the power amplifiers. Yet, it can be shown with the simulation model that the successful read out of MPC structures is in reach and is feasible if the intermodulation distortion level can be decreased. Additionally, the successful read out of a magnetostrictive sensor made of a ribbon of magnetostrictive alloy was demonstrated. The presented read out method is, hence, successfully applicable for magnetostrictive sensors.

6.1 Future Work

Currently, the intermodulation distortion generated by the power amplifiers represent the main limitation and inhibit the read out of smaller sized CoNi structures and MPC structures. However, the replacement of the power amplifier by another device was already considered and does not represent a solution, since devices from other manufacturers do not show a lower distortion characteristic. The read out sensitivity can be further increased by increasing the probe frequency. For that, a power amplifier with a larger bandwidth is required and the design of the probe coil has to be optimized for higher frequencies. Furthermore, a few practical improvements on the experimental setup simplify the read out process and improve the reliability. Installing a camera to see the alignment of pick-up coil to resonator structure decreases the installation time and ensures optimal alignment. The DC coils become rather fast too warm and plastic material like polycarbonate start to melt. This limits the usage of the DC-coils to a few minutes if they are operated at the full current. A liquid cooling system could, thus, significantly increase the operation time of the DC coils.

For the CoNi structures, it is proposed to study functionalization methods. Subsequently, experiments with functionalized structures can be performed. By means of the functionalization, specific species can be weighted and be recognized.

1. Reduce distortion of power amplifier:
    - Option 1: Design of a power amplifier specifically designed for low distortion at the used frequencies.

- Option 2: Change excitation and probe coil to a smaller size to reduce the power requirement to the power amplifier. Potentially, a power operational amplifier could be used. Power operational amplifier offer significantly improved distortion figures.

2. Increase the bandwidth of the experimental setup. This requires to employ a power amplifier with a higher bandwidth and to optimize the probe coil design for higher frequencies.

3. Install a camera in the experimental setup for the verification of the alignment pick-up coil to resonator structure.

4. Change the design of DC coils and equip it with a liquid cooling system.

5. Study functionalization of CoNi and perform experiments with functionalized structures.

References

[1] J. J. Abbott, O. Ergeneman, M. Kummer, A. M. Hirt, and B. J. Nelson. Modeling magnetic torque and force for controlled manipulation of soft-magnetic bodies. *IEEE Transactions on Robotics*, 23(6):pp. 1247–1252, December 2007.

[2] Analog Devices. *AD8099 datasheet*, 2004.

[3] B. Ando, S. Baglio, M. Bau, V. Ferrari, E. Sardini, N. Savalli, M. Serpelloni, and C. Trigona. Contactless electromagnetic interrogation of a mems based microresonator used as passive sensing element. In *IEEE Transducers*, June 2009.

[4] C. Azzolini, A. Magnanini, M. Tonelli, G. Chiorboli, and C. Morandi. Integrated lock-in amplifier for contactless interface to magnetically stimulated mechanical resonators. In *International Conference on Design and Technology of Integrated Systems in Nanoscale Era*, 2008.

[5] M. Bau, V. Ferrari, and D. Marioli. Contactless excitation of mems resonant sensors by electromagnetic driving. In *Proceedings COMSOL Conference Milan*, 2009.

[6] M. Bau, V. Ferrari, D. Marioli, E. Sardini, M. Serpelloni, and A. Taroni. Contactless electromagnetic excitation of conductive microstructures for resonant sensors. In *Technology Conference - IMTC 2007*, May 2007.

[7] M. Bau, V. Ferrari, D. Marioli, E. Sardini, M. Serpelloni, and A. Taroni. Contactless excitation and readout of passive sensing elements made by miniaturized mechanical resonators. In *IEEE SENSORS*, 2007.

[8] M. Bau, V. Ferrari, D. Marioli, E. Sardini, M. Serpelloni, and A. Taroni. Contactless electromagnetic excitation of resonant sensors made of conductive miniaturized structures. *Sensors and Actuators*, 2008.

[9] M. Bau, M. Motterlini, V. Ferrari, D. Marioli, and A. Taroni. Contactless system for dynamic characterisation of microresonators. *ELECTRONICS LETTERS*, April 2006.

[10] T. P. Burg, M. Godin, S. M. Knudsen, W. Shen, G. Carlson, J. S. Foster, K. Babcock, and S. R. Manalis. Weighing of biomolecules, single cells and single nanoparticles in fluid. *nature*, 446(05741), April 2007.

[11] W. Dai, K. Lian, and W. Wang. A quantitative study on the adhesion property of cured su-8 on various metallic surfaces. *Microsystem Technology*, 2005.

[12] C. De Angelis, V. Ferrari, D. Marioli, E. Sardini, M. Serpelloni, and A. Taroni. Magnetically induced oscillations on a conductive cantilever for resonant microsensors. *Sensors and Actuators*, 2007.

[13] P. Eberle. *Wireless Read Out of Magnetic Polymer Cantilever*. Semester Thesis, ETH Zurich, 2009.

[14] L. Ejsing, M. F. Hansen, A. K. Menon, H. A. Ferreira, D. L. Graham, and P. P. Freitas. Planar hall effect sensor for magnetic micro- and nanobead detection. *APPLIED PHYSICS LETTERS*, 84(23), June 2004.

[15] EPCOS AG. *SIFERRIT material N87 datasheet*, 2006.

[16] O. Ergeneman, K. Sivaraman, E. Pellicer, M. D. Bar, A. M. Hirt, A. Teleki, S. Pan, and B. J. Nelson. Magnetic properties of electrodeposited cobalt-nickel thin films from acidic baths containing glycine. In *Proc. in 216th ECS Meeting, Vienna, Austria*, October 2009.

[17] O. Ergeneman, M. Suter, G. Chatzipirpiridis, J. Zuercher, S. Graf, S. Pane, C. Hierold, and B. J. Nelson. Characterization and actuation of a magnetic photosensitive polymer cantilever. In *IEEE*, 2009.

[18] M. Flueckiger, Z. Nagy, M. Probst, O. Ergeneman, S. Pane, and B. J. Nelson. A microfabricated and microassembled wireless resonator. *Sensors and Actuators A: Physical*, 154(1):109 – 116, 2009.

[19] L. Fu, S. Li, K. Zhang, I.-H. Chen, V. A. Petrenko, and Z. Cheng. Magnetostrictive microcantilever as an advanced transducer for biosensors. *Sensors*, 2007.

[20] L. Fu, S. Li, K. Zhang, and Z.-Y. Cheng. Detection of bacillus anthracis spores in water using biosensors based on magnetostrictive microcantilever coated with phage. In *Micro (MEMS) and Nanotechnologies for Defense and Security*, volume 6556, 2007.

[21] E. P. Furlani. *Permanent Magnet and Electromechanical Devices*. Academic Press, San Diego, 2001.

[22] S. Graf. Superparamagnetic polymer nanocomposite microresonator. Master's thesis, ETH Zurich, 2008.

[23] C. A. Grimes, K. G. Ong, K. Loiselle, P. G. Stoyanov, D. Kouzoudis, Y. Liu, C. Tong, and F. Tefiku. Magnetoelastic sensors for remote query environmental monitoring. *IOP Publishing Ltd*, 1999.

[24] C. A. Grimes, P. G. Stoyanov, and D. Kouzoudis. Magnetoelastic sensing apparatus and method for remote pressure query of an environment. *US patent: US 6,393,921*, May 2002.

[25] M. L. Johnson, J. Wan, S. Huang, Z. Cheng, V. A. Petrenko, D.-J. Kim, I.-H. Chen, B. J. M, J. W. Hong, and B. A. Chin. A wireless biosensor using microfabricated phage-interfaced magnetoelastic particles. *Sensors and Actuators*, 2008.

[26] Krohn-Hite Corporation. *Operating Manual Model 7500 Wideband Power Amplifier*, 2004.

[27] G. Lehner. *Elektromagnetische Feldtheorie*. Springer, 4 edition, 2004.

[28] S. Li, L. Fua, J. Barbareeb, and Z.-Y. Chenga. Resonance behavior of magnetostrictive micro/milli-cantilever and its application as a biosensor. *Sensors and Actuators*, 2009.

[29] S. Li, L. Orona, Z. Li, and Z.-Y. Chenga. Biosensor based on magnetostrictive microcantilever. *APPLIED PHYSICS LETTERS*, 2006.

[30] Linear Technology. *LT6200 datasheet*, 2002.

[31] R. Mestroma, R. Fey, J. van Beekb, K. P. b, and H. Nijmeijer. Modelling the dynamics of a mems resonator: Simulations and experiments. *Sensors and Actuators A:Physical*, 2008.

[32] Metglas, Inc. *Technical Bulletin Magnetic Alloy 2826MB*, 2009.

[33] Micro Chem. *Omnicoat*.

[34] Micro Chem. *SU-8 Material Safety Data Sheet*, 2001.

[35] Micro Resist Technology. *Developer mr-Dev 600 Safety Data Sheet*, 2010.

[36] Microchemicals. *AZ4562 Sicherheitsdatenblatt*, 2005.

[37] F. Nguyen, V. Dau, A. Schuhl, J. Childress, and M. Sussiau. Magnetic sensors for nanotesla detection using planar hall effect. *Sensors and Actuators A:Physical*, 1996.

[38] M. Nordström a, A. Johansson, E. S. Nogueron, B. Clausen, M. Calleja, and A. Boisen. Investigation of the bond strength between the photo-sensitive polymer su-8 and gold. *Microelectronic Engineering*, 2005.

[39] H. J. Oguey. Sensitive flux measurements of thin magnetic films. *The Review of Scientific Instruments*, 31(7), July 1960.

[40] E. K. Reichel, C. Riesch, F. Keplinger, and B. Jakoby. Remote electromagnetic excitation of miniaturized inplane plate resonators for sensing applications. *IEEE*, 2008.

[41] A. Schuhl, F. Nguyen Van Dau, and J. R. Childress. Low-field magnetic sensors based on the planar hall effect. *Appl. Phys. Lett.*, 66, May 1995.

[42] Shipley. *Microposit 351 Developer*, 1991.

[43] M. Suter, O. Ergeneman, S. Schmid, A. Camenzind, B. J. Nelson, and C. Hierold. Superparamagnetic photosensitive polymer nanocomposite for microactuators. In *IEEE*, 2009.

[44] C. Vancura, M. Ruegg, Y. Li, C. Hagleitner, and A. Hierlemann. Magnetically actuated complementary metal oxide semiconductor resonant cantilever gas sensor systems. *Anal. Chem.*, 2005.

[45] P. S. Waggoner, C. P. Tan, L. Bellan, and H. G. Craighead. High-q, in-plane modes of nanomechanical resonators operated in air. *JOURNAL OF APPLIED PHYSICS*, 105, 2009.

[46] J. Wan, M. L. Johnson, R. Guntupalli, V. A. Petrenko, and B. A. Chin. Detection of bacillus anthracis spores in liquid using phage-based magnetoelastic micro-resonators. *Sensors and Actuators*, 2007.

[47] K. Zeng and C. A. Grimes. Wireless magnetoelastic physical, chemical and biological sensors. *IEEE Transactions on Magnetics*, 43(6), June 2007.

[48] C. Ziegler. Cantilever-based biosensors. *Anal Bioanal Chem*, 2004.

[49] Zurich Instruments. *HF2 User Manual*, 2010.

A Appendix Simulation

A.1 Pick-up Voltage in Variation of Resonator Structure Thickness

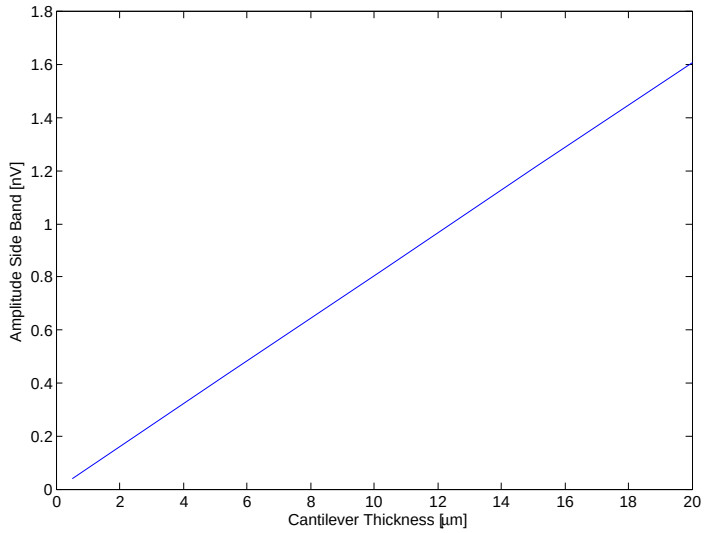

Figure 69: Case in-plane motion and out-plane magnetization: Side band amplitude of a rectangular pick-up coil (4 mm x 4 mm) in variation of the magnet bar thickness with a magnet bar length of $l_x = 400\,\mu\text{m}$ and a width of $w_y = 400\,\mu\text{m}$. Pick-up coil is optimally aligned to magnet bar. Used parameters: magnetization $M_z = 1\,\text{kA/m}$, probe frequency $f_p = 100\,\text{kHz}$, vibration frequency $f_m = 2\,\text{kHz}$ and deflection $\Delta\hat{z}_p = 1\,\mu\text{m}$.

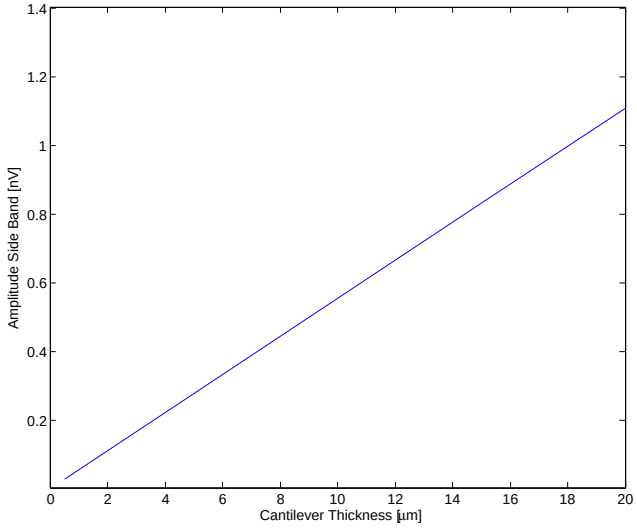

Figure 70: Case out-plane motion and out-plane magnetization: Side band amplitude of a rectangular pick-up coil (4 mm x 4 mm in variation of the magnet bar thickness with a magnet bar length of $l_x = 400\,\mu\text{m}$ and a width of $w_y = 400\,\mu\text{m}$. Pick-up coil is optimally aligned to magnet bar. Used parameters: magnetization $M_z = 1\,\text{kA/m}$, probe frequency $f_p = 100\,\text{kHz}$, vibration frequency $f_m = 2\,\text{kHz}$ and deflection $\Delta\hat{z}_p = 1\,\mu\text{m}$.

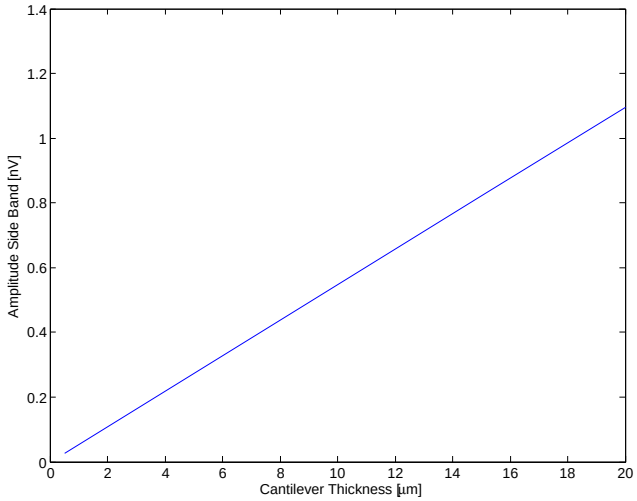

Figure 71: Case in-plane motion and in-plane magnetization: Side band amplitude of a rectangular pick-up coil (4 mm x 4 mm) in variation of the magnet bar thickness with a magnet bar length of $l_y = 400\,\mu\text{m}$ and a width of $w_z = 400\,\mu\text{m}$. Pick-up coil is optimally aligned to magnet bar. Used parameters: magnetization $M_z = 1\,\text{kA/m}$, probe frequency $f_p = 100\,\text{kHz}$, vibration frequency $f_m = 2\,\text{kHz}$ and deflection $\Delta\hat{z}_p = 1\,\mu\text{m}$.

B Appendix Fabrication

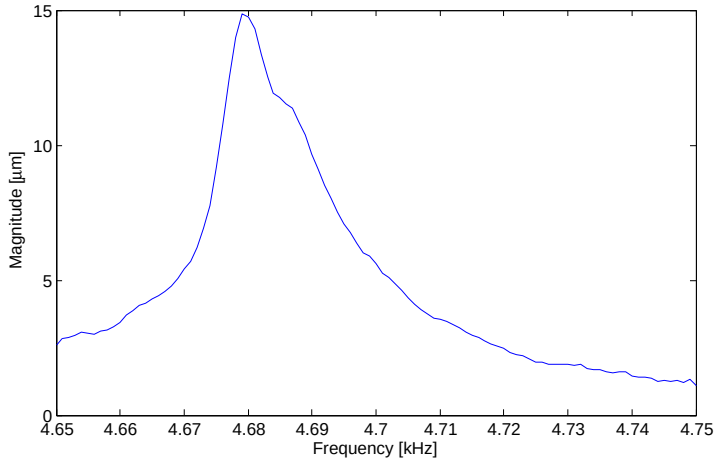

Figure 72: In-plane deflection frequency response of a 400 µm x 400 µm plate suspended by a 200 µm x 11 µm spring. The graph was obtained with the planar motion analyzer. Plate 6 of arrangement as depicted by figure 38 was measured.

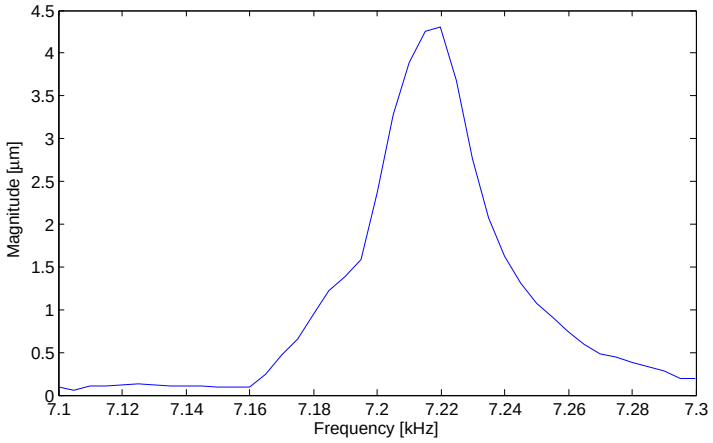

Figure 73: In-plane deflection frequency response of a 300 µm x 300 µm plate suspended by a 200 µm x 11 µm spring. The graph was obtained with planar motion analyzer. Plate 4M of arrangement as depicted by figure 39 was measured.

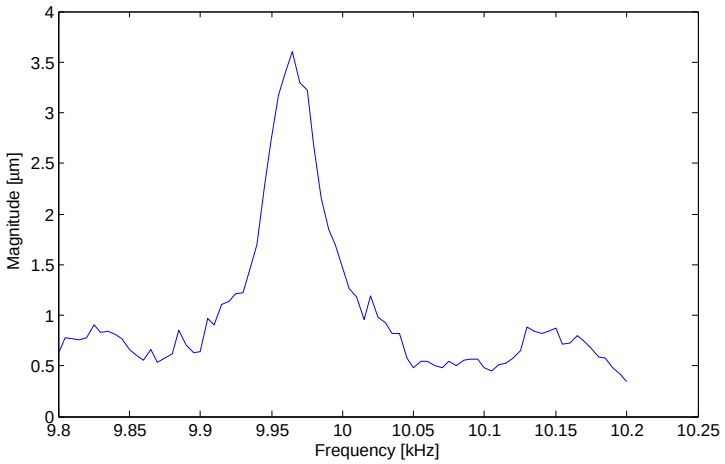

Figure 74: In-plane deflection frequency response of a 250 µm x 250 µm plate suspended by a 200 µm x 11 µm spring. The graph was obtained with planar motion analyzer. Plate 3S of arrangement as depicted by figure 39 was measured.

Type	**Setting**
Mode	*Eigenfrequency solid, stress-strain 3D*
Young's modulus	$E = 2.05 \cdot 10^{11}$ GPa
Poisson's ratio	$\nu = 0.31$
Density	$\rho = 8900\,\mathrm{kg/m^3}$
Boundary conditions computational domain	*fixed on spring, other free*
Mesh	*extended size*
Other	*standard settings*

Table 14: COMSOL settings for eigenfrequency simulation

C Appendix Experiment

C.1 Design of the Experimental Setup

Type	**Instrument**
Lock in amplifier	Zurich Instruments HF2LI with Multifrequency Kit [49]
Power amplifiers	Krohn-Hite Model 7500 (Wideband) [26]
Scope	Tektronix 4 channel
Current probe	Tektronix TCPA300
ACSC unit	Own design as described in 5.3

Table 15: Instruments used in the experimental setup

Type	**Setting**
Mode	*Azimuthal Induction Currents, Vector Potential 2D*
Current density in coil	$J = 3.6 \cdot 10^6\,\mathrm{A/m^2}$
Boundary conditions coil	*continuity* $\vec{n} \times (\vec{H}_1 - \vec{H}_2) = 0$
Boundary conditions symmetry line	*axial symmetry* $r = 0$
Boundary conditions computational domain	*magnetic insulation* $A_\varphi = 0$
Mesh	*extended size*
Other	*standard settings*

Table 16: COMSOL settings for coil simulation

For the current density in table 16 a shape factor $\frac{\pi}{4}$ has to be considered due to the circular form of the wire. A filling factor for the manually wound coil is not considered.

Constraint	**Value**
S_{max} (power amplifier)	75 VA ($f \leq 100$ kHz)
I_{max} (power amplifier)	625 mA (RMS)
U_{max} (power amplifier)	140 V (RMS)

Table 17: Constraints for the design of the excitation and probe coil

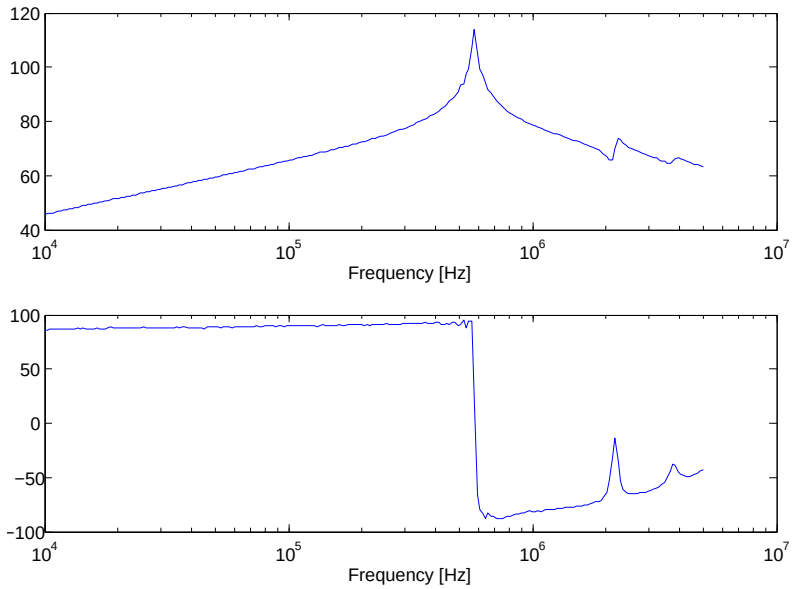

Figure 75: Impedance frequency response of the excitation coil. Due to the magnetic coupling with the probe coil, the probe coil was terminated with a 240 Ω resistor, which is a representative value for the output impedance of the power amplifier.

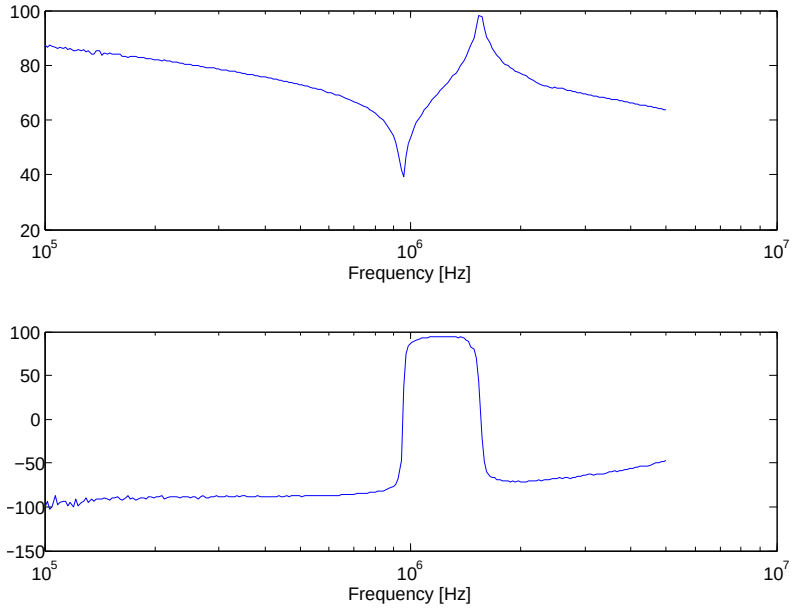

Figure 76: Impedance frequency response of the probe coil with in series connected 47 pF capacitance. The excitation coil was terminated, due to the magnetic coupling with the probe coil, with a 240 Ω resistor to represent the output impedance of the power amplifier. The distinctive dip in magnitude and the rapid phase change at $f = 957$ kHz mark the resonant frequency of probe coil and 47 pF capacitance.

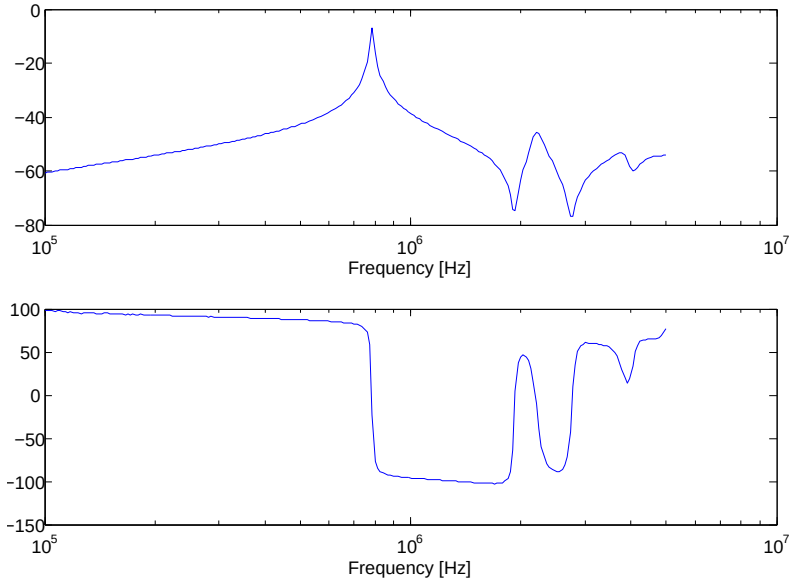

Figure 77: Frequency response of transfer function from probe - to excitation coil. In series to the probe coil a 68 pF capacitance was connected and the excitation coil was terminated with a 240 Ω resistor.

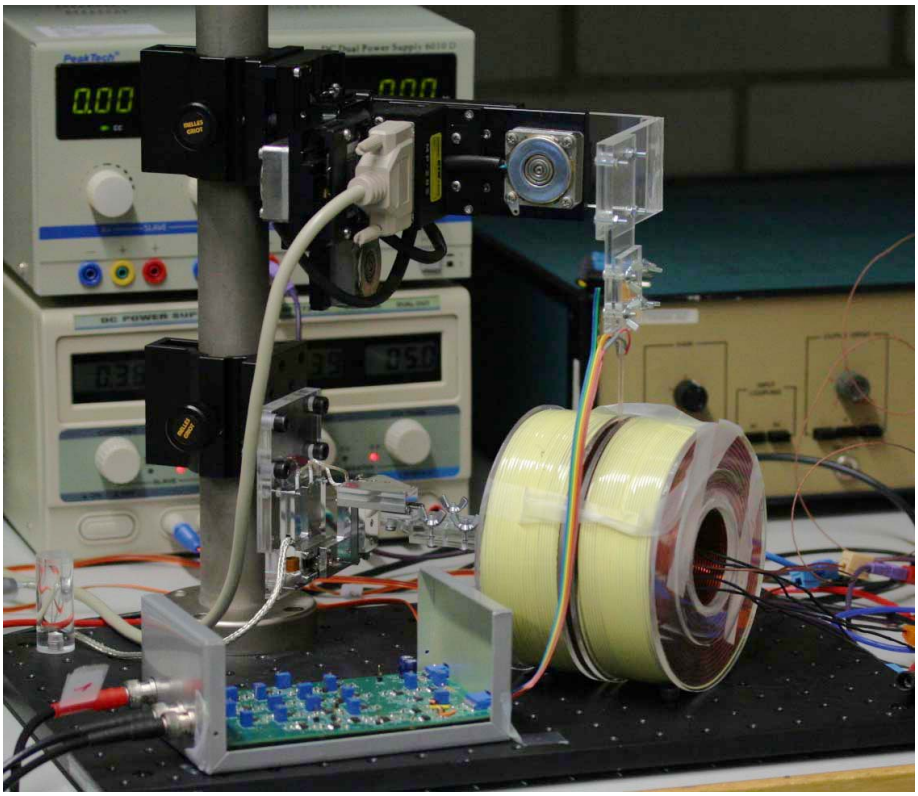

Figure 78: Picture of the experimental setup. The two large yellow colored coils are the DC coil pair. The acrylic rod, which is inserted between the two DC coils, carries the pick-up coils and is positioned in the z-axis via the micro-positioning stage. The pick-up coil wires are connected with the colored ribbon cable to the ACSC unit (grey aluminum box). The second micro-positioning stage is employed to position the resonator in x -, y - and z axis. On the back, the lower DC power supply is used for the ACSC unit and the upper DC power supply provides the current for the DC coil pair. On the right side on the back, the device is one of the two Krohn Hite 7500 power amplifiers.

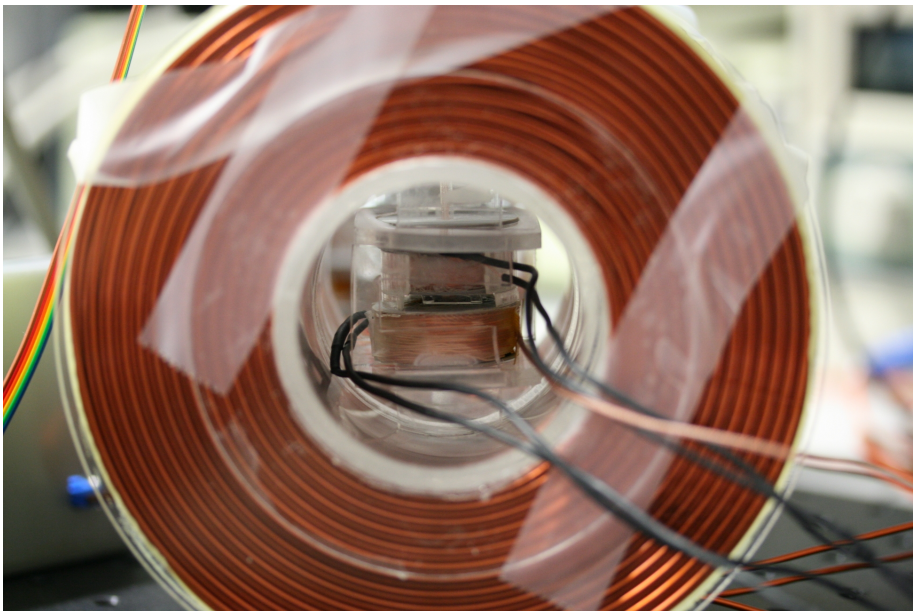

Figure 79: Picture from the right side into the DC coil. The lower coil represents the actuation coil and the upper coil the probe coil. In the slot between the two coils the resonator is introduced for the measurement process. The acrylic rod carrying the pick-up coils goes through the probe coil. One of the pick-up coils resides at the lower edge of the probe coil and the other one stands at the upper edge of the probe coil. By means of the z-axis micro-positioning stage of the acrylic rod the symmetry of the two pick-up coils to the probe coil can be adjusted.

C.2 Circuit Design of the ACSC Unit

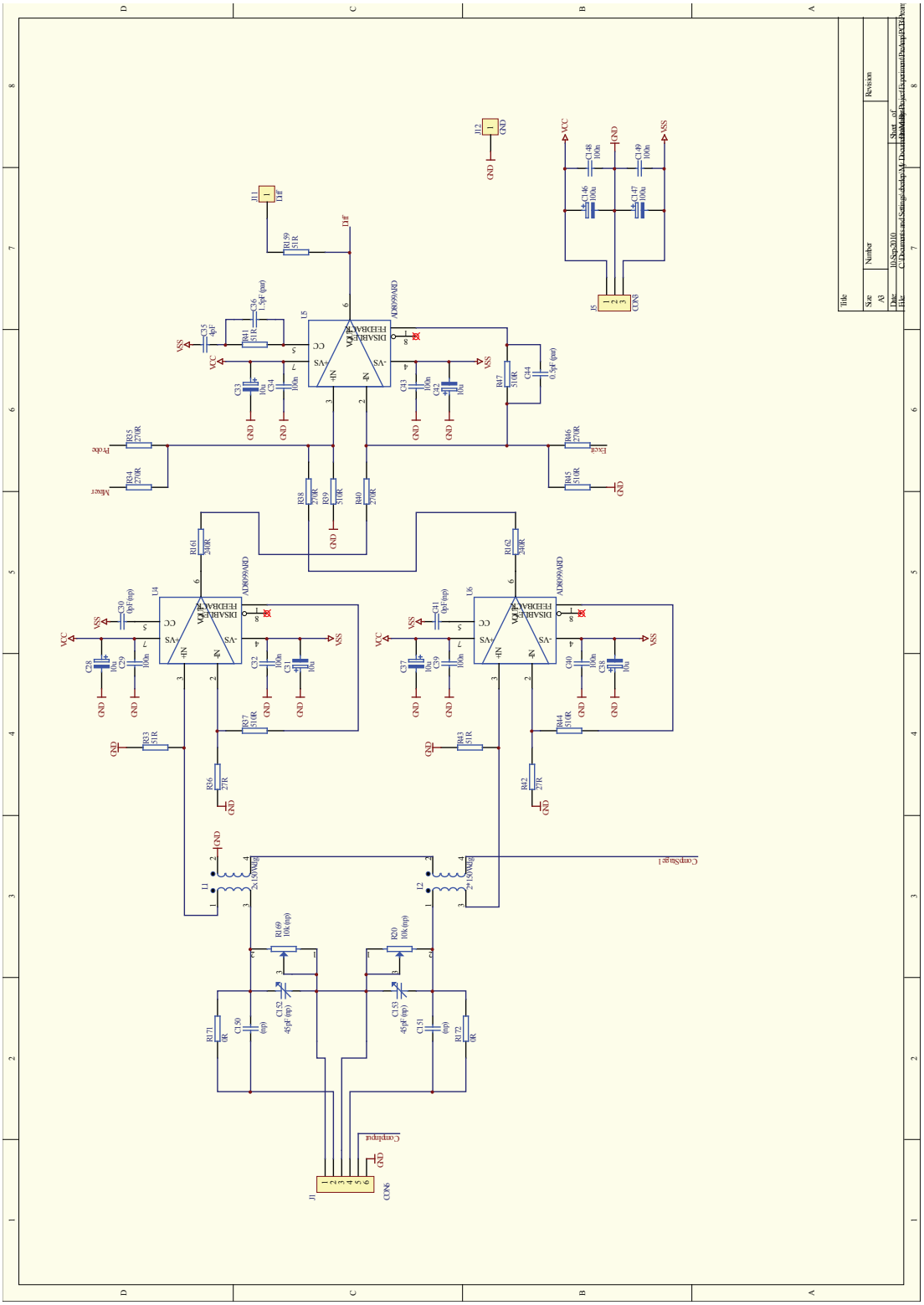

Figure 80: ACSC unit schematic input part.

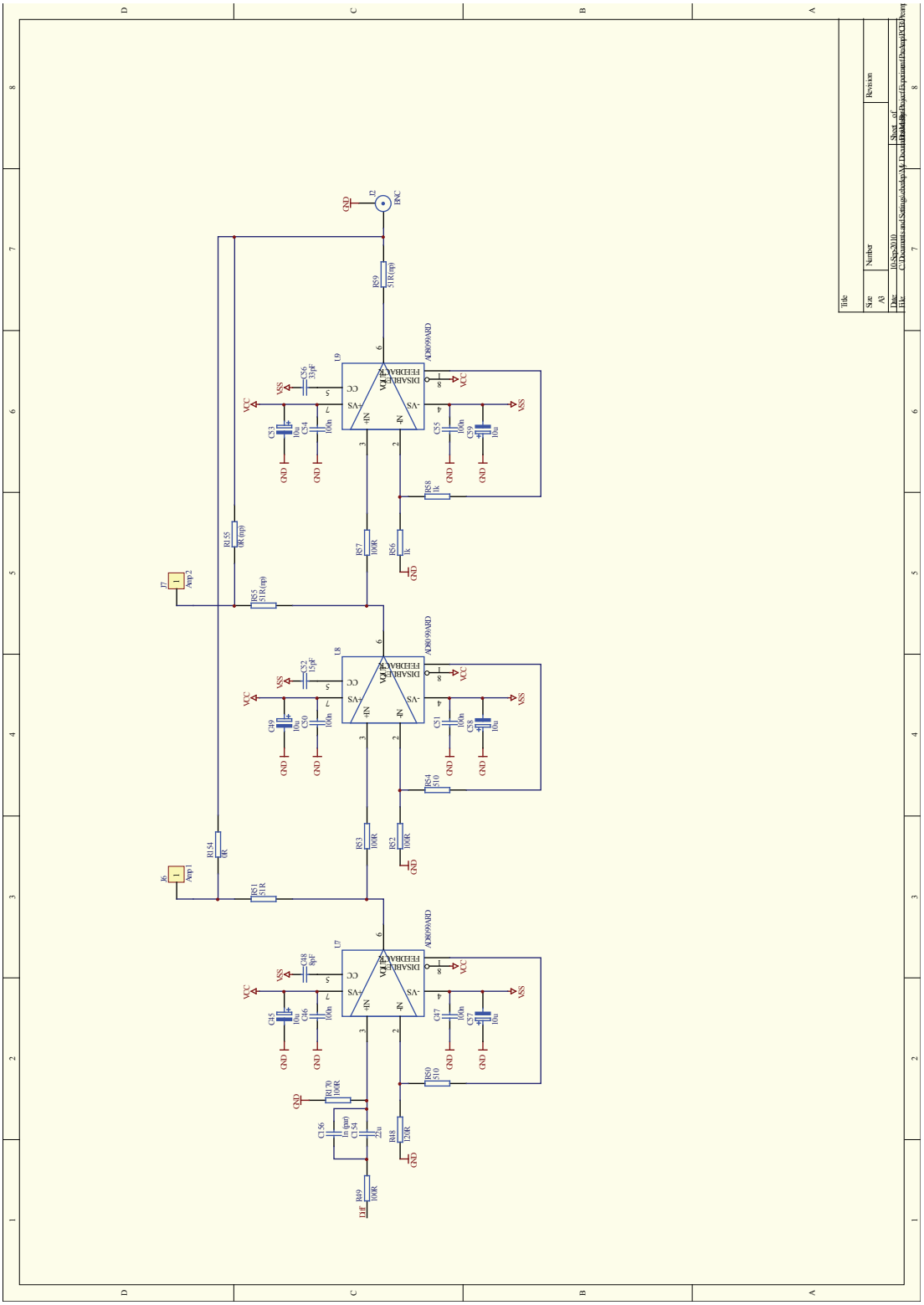

Figure 81: ACSC unit schematic output part.

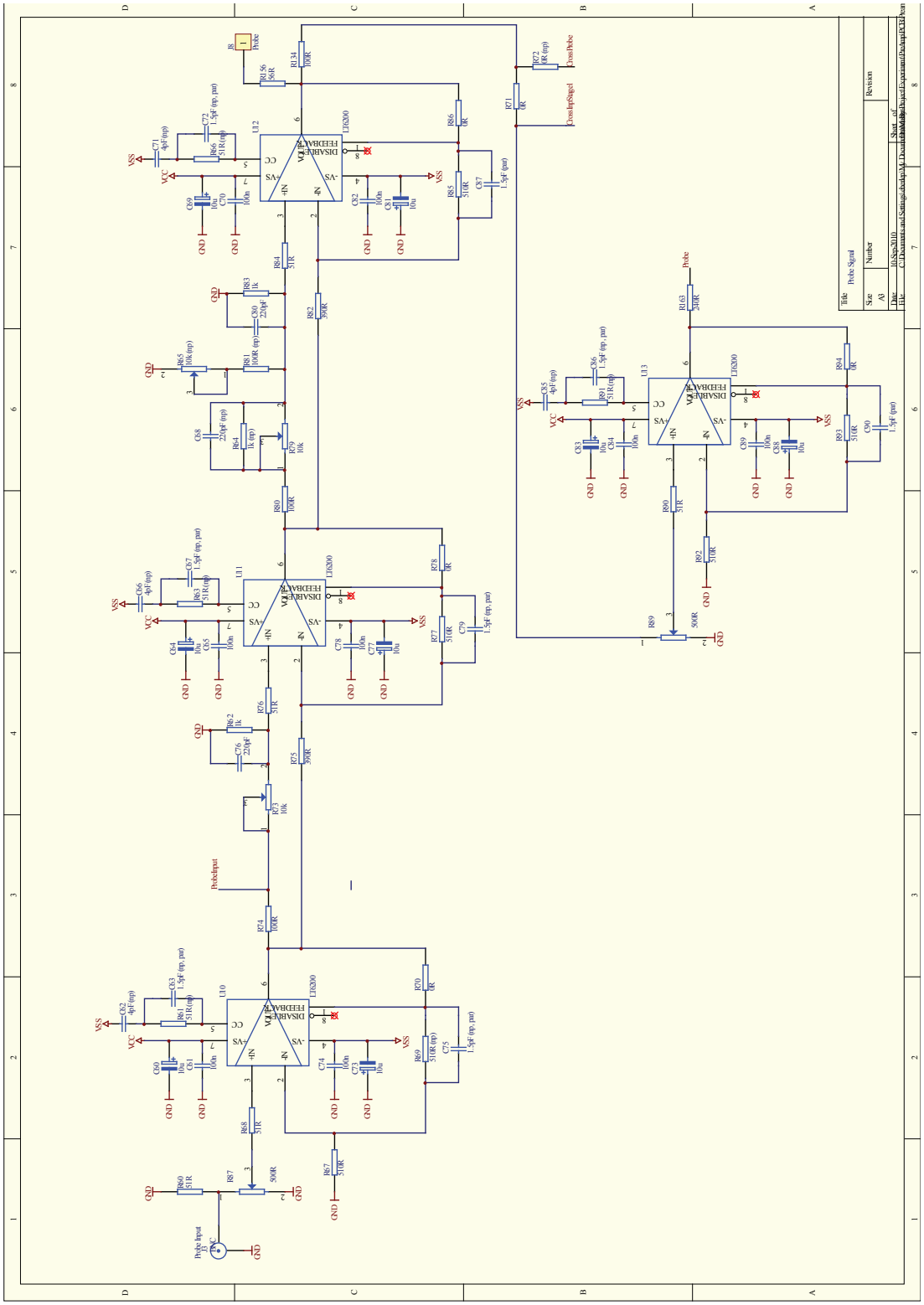

Figure 82: ACSC unit schematic probe part.

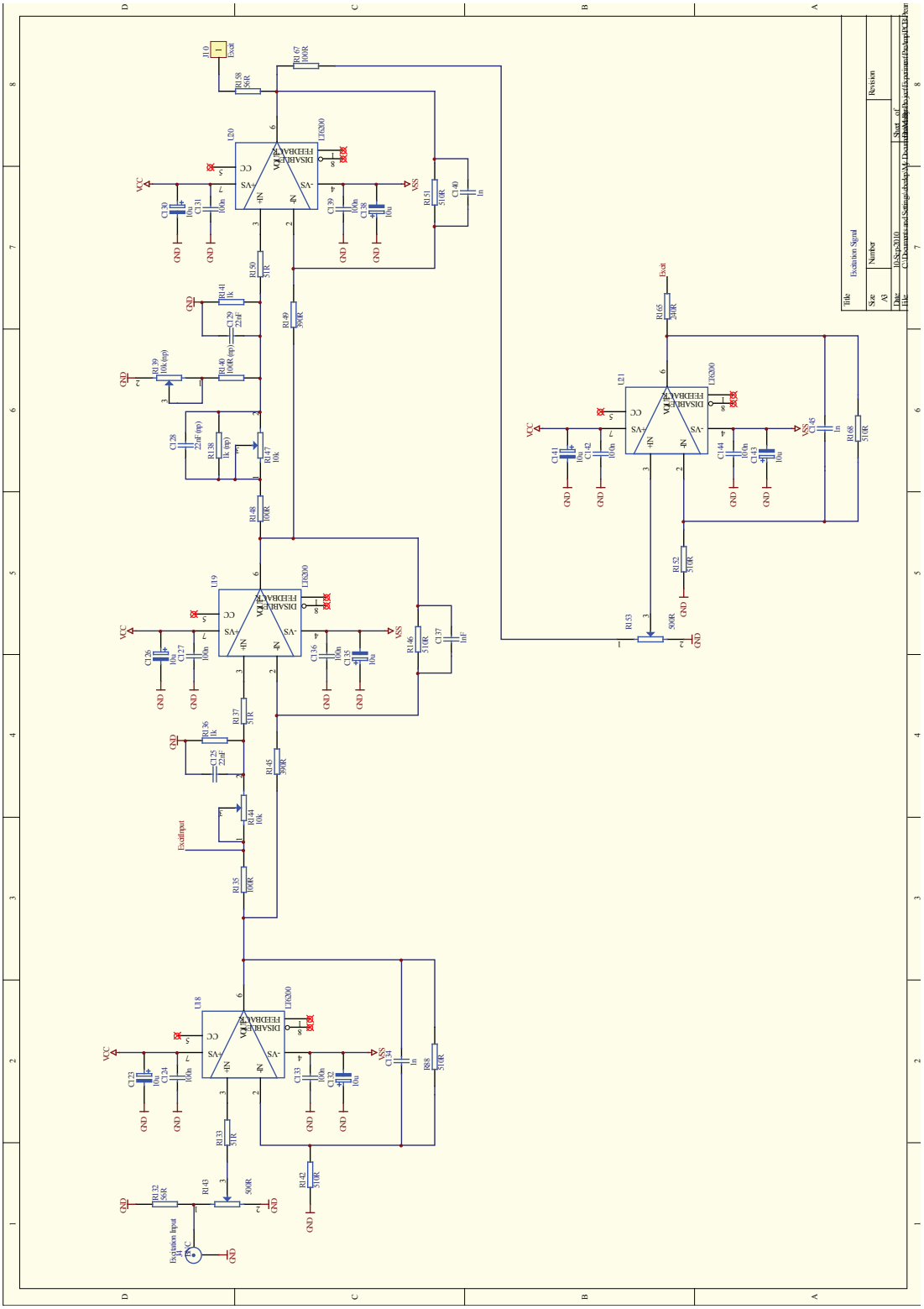

Figure 83: ACSC unit schematic excitation part.

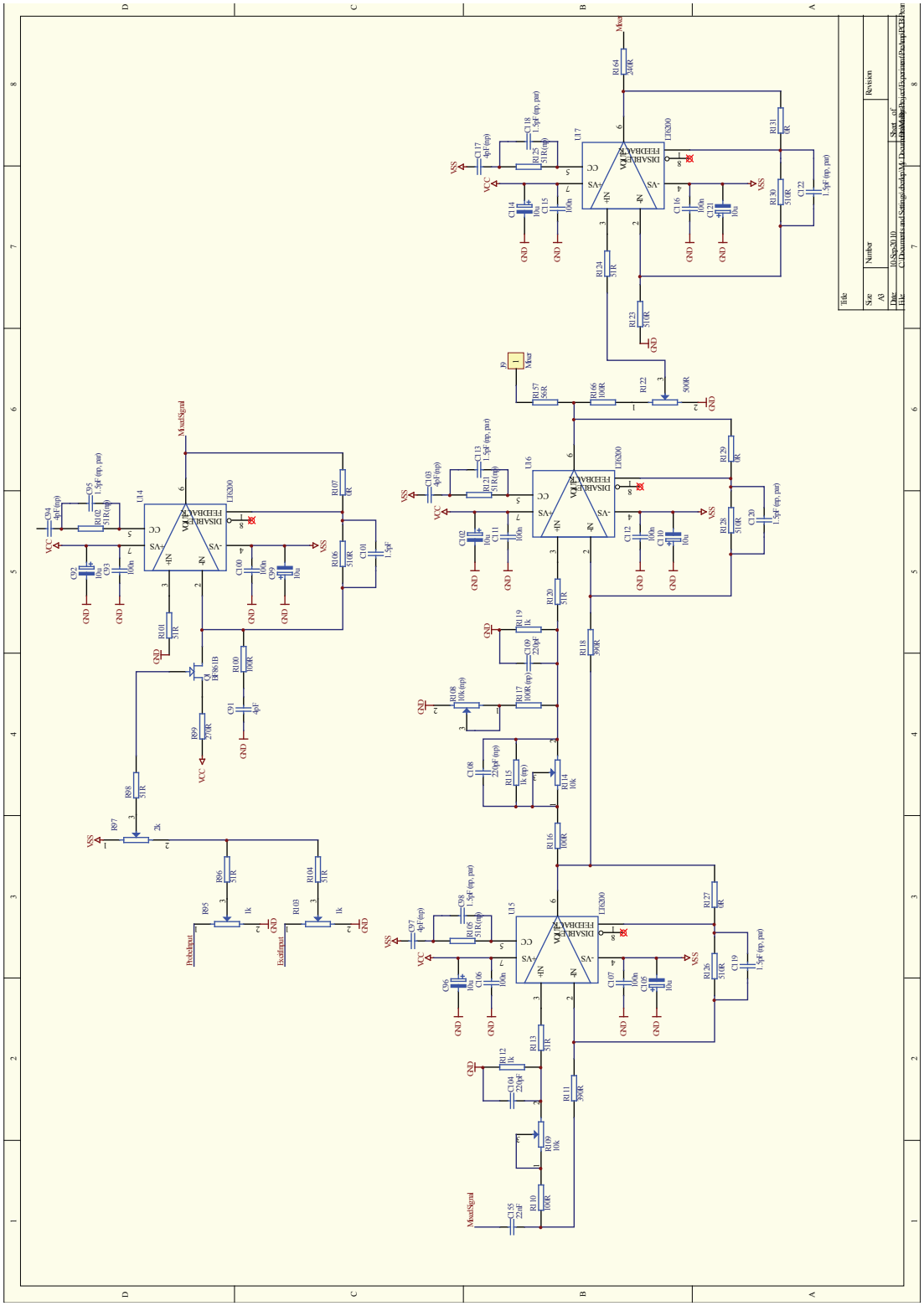

Figure 84: ACSC unit schematic mixer part.

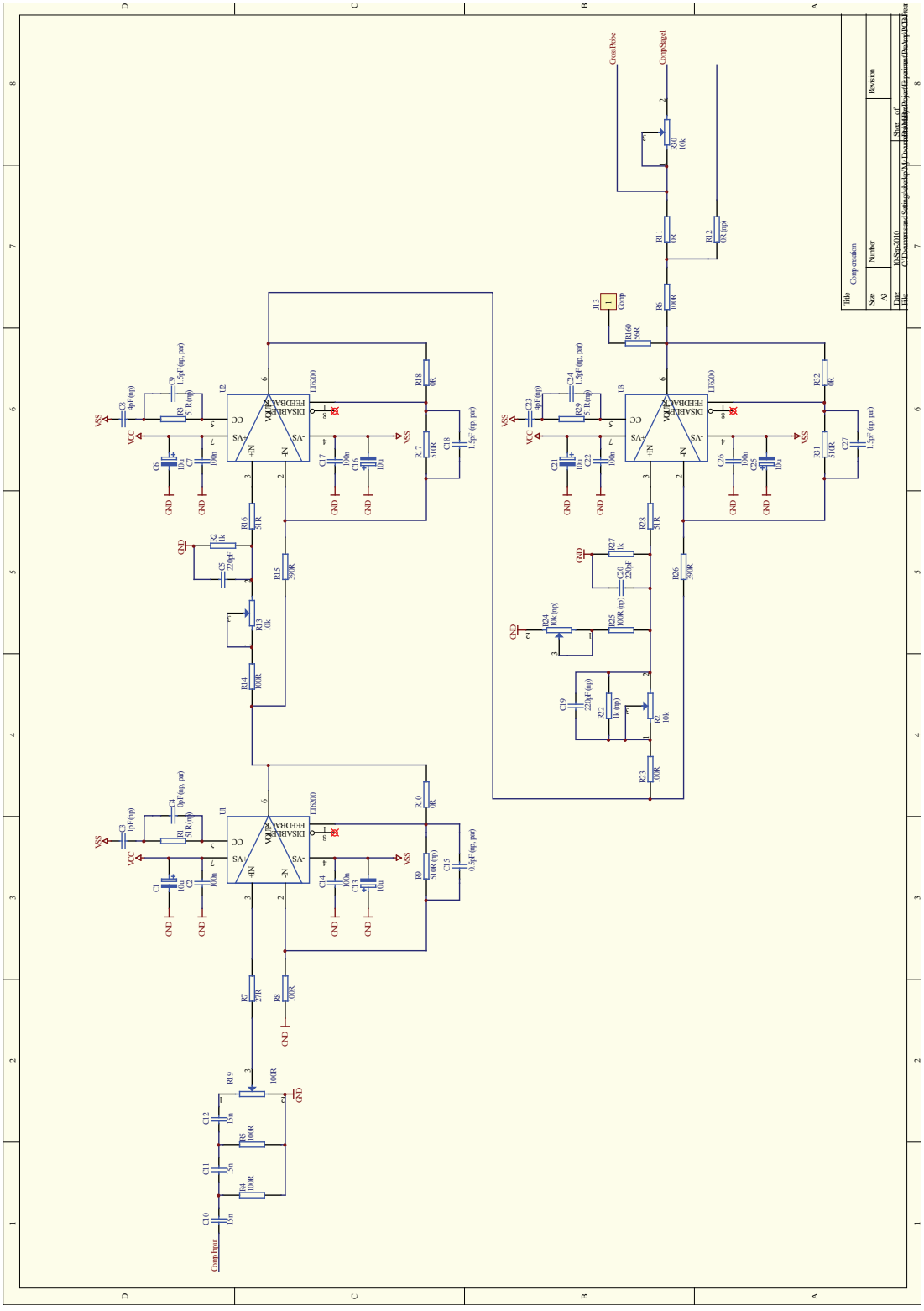

Figure 85: ACSC unit schematic compensation part.

C.3 Noise Equivalent Schematic of the ACSC Unit

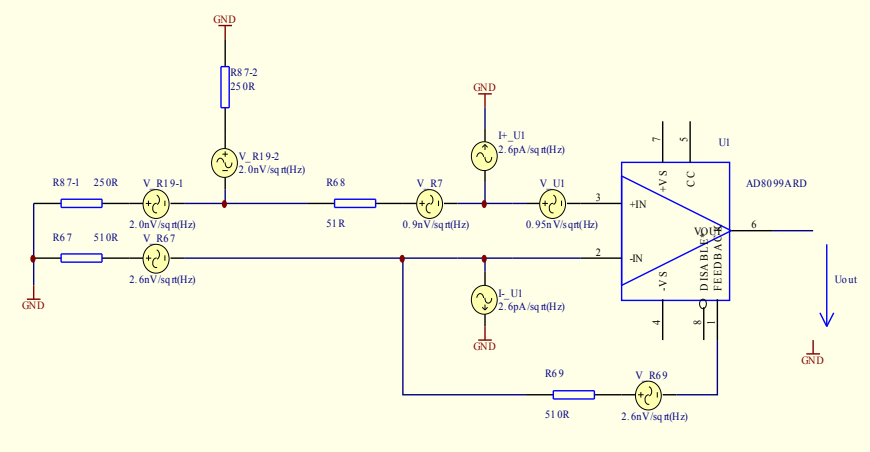

Figure 86: Noise equivalent circuit for the probe input.

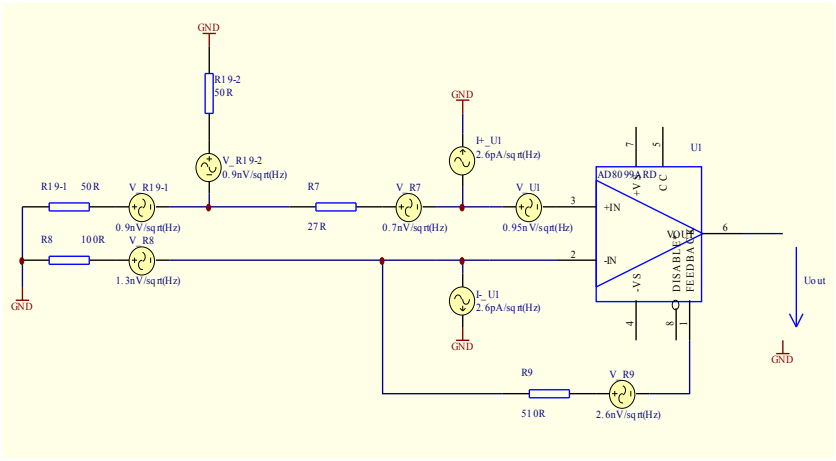

Figure 87: Noise equivalent circuit for the compensation input.

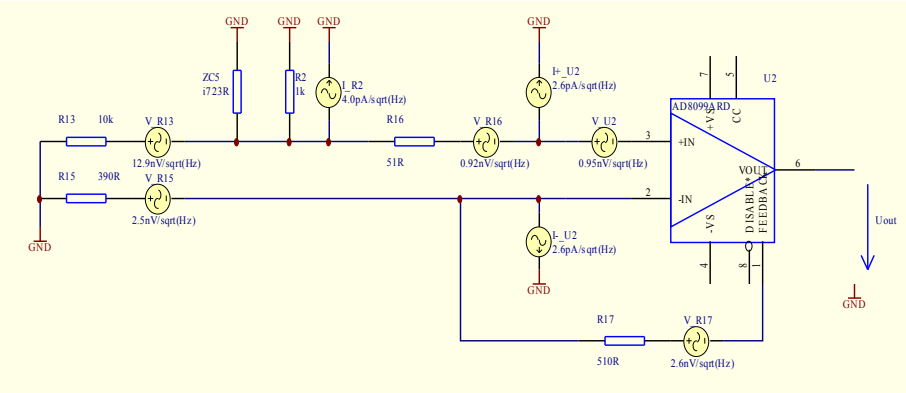

Figure 88: Noise equivalent circuit for the phase shifter.

C.4 Noise Measurement of the ACSC Unit

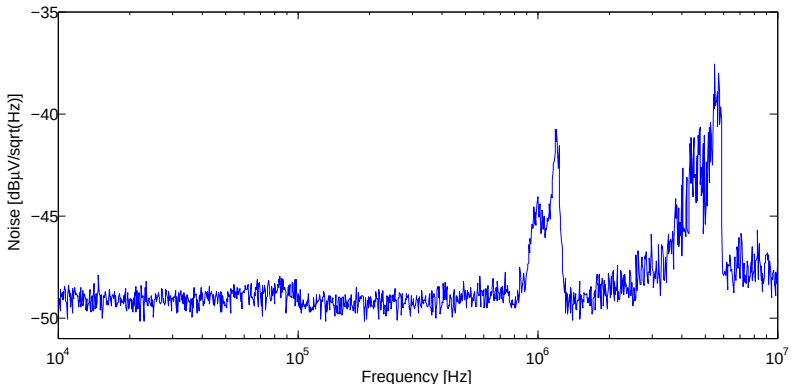

Figure 89: Spectral density of the thermal noise of the output of the ACSC unit with the usage of the inductive compensation circuitry (Potentiometer $R30 = 10\,k\Omega$). The ACSC unit is used in differential input configuration and the inputs are open. All values are referred to the input.

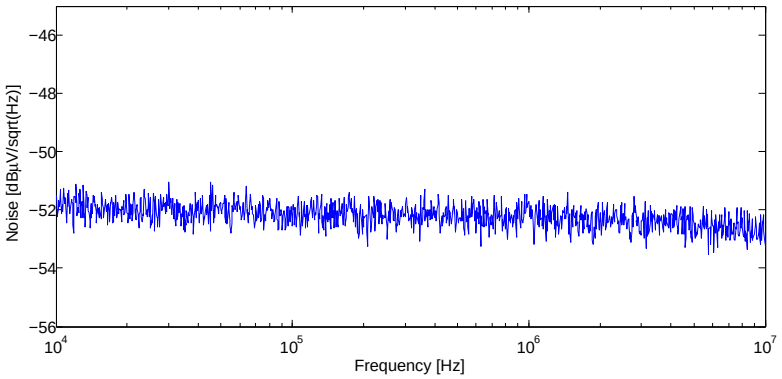

Figure 90: Spectral density of the thermal noise of the output of the ACSC unit in single ended input configuration. The input is open and all values are referred to the input. The inductive compensation circuitry is not considered and by-passed.

C.5 Frequency Response of the ACSC Unit

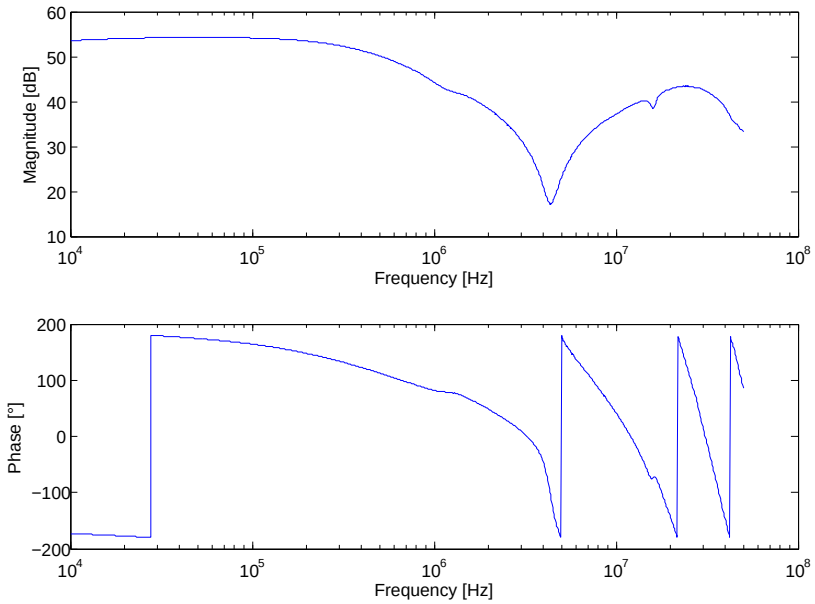

Figure 91: Frequency response of the input to the output of the ACSC unit with inductive compensation circuitry. The coil of the inductive compensation has a resonant frequency at 4.5 MHz, which limits the input bandwidth to < 0.6 MHz

C.6 Results

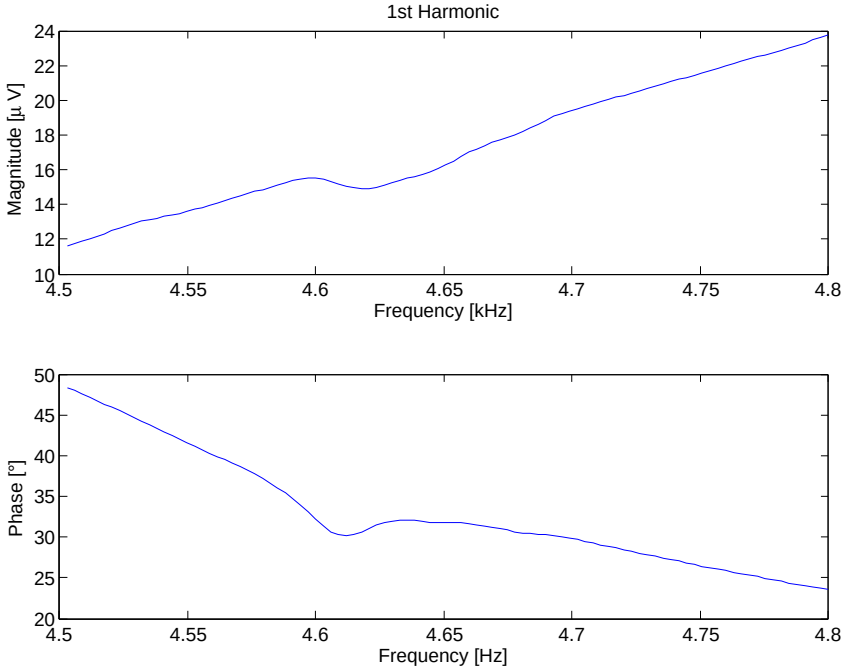

Figure 92: Read out of first harmonic of resonator 1 mm x 1 mm x 50 µm.

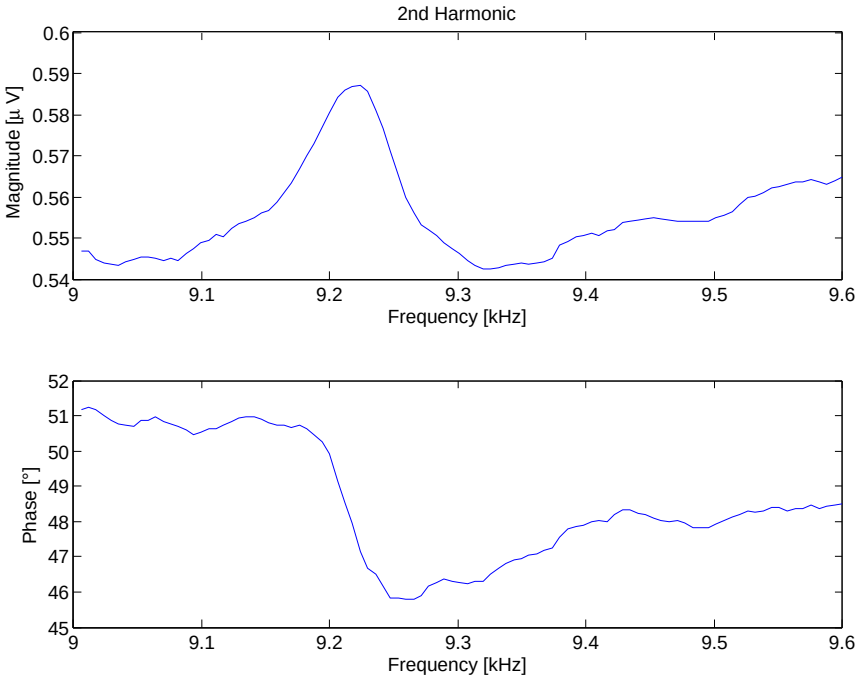

Figure 93: Read out of second harmonic of resonator 1 mm x 1 mm x 50 µm.

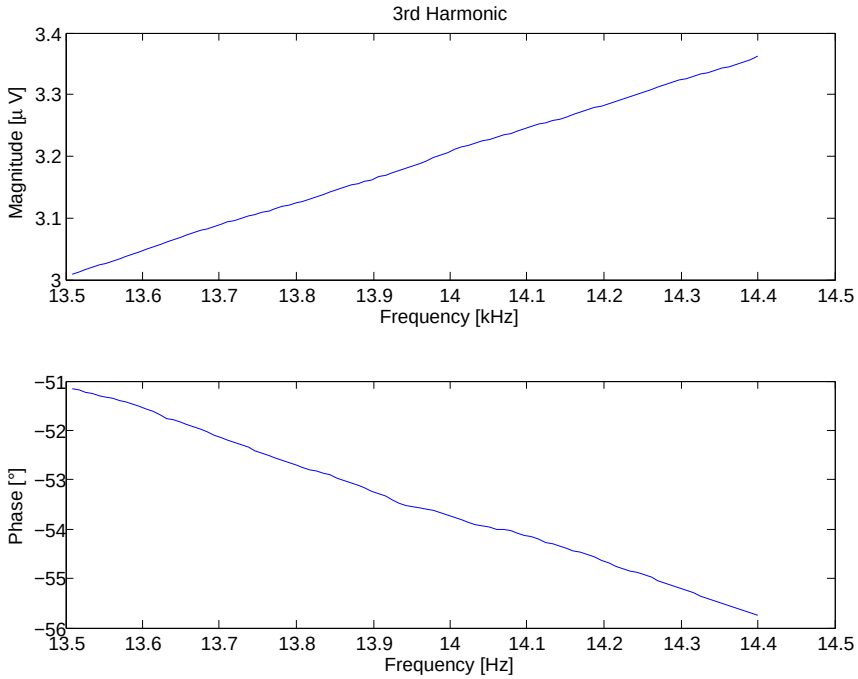

Figure 94: Read out of third harmonic of resonator 1 mm x 1 mm x 50 µm.

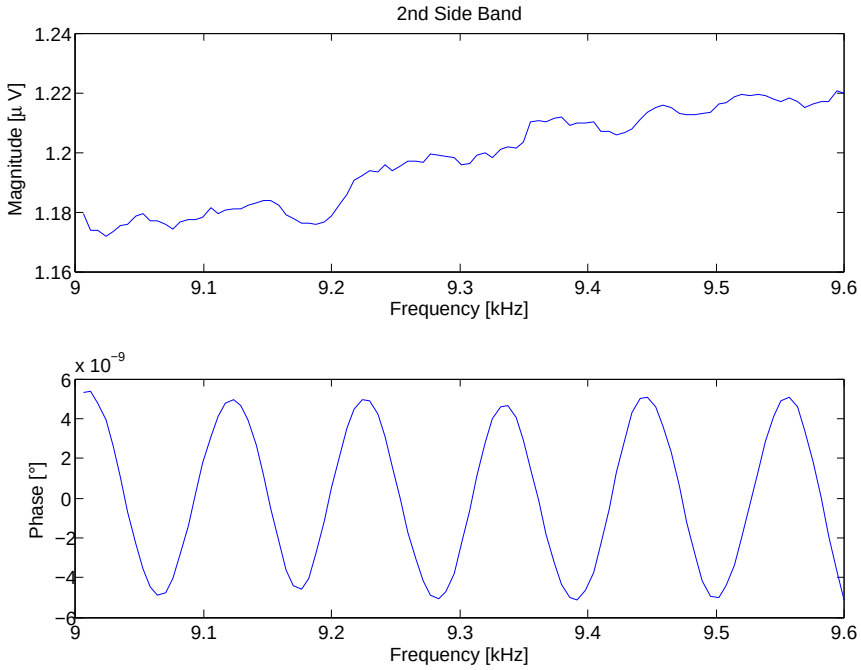

Figure 95: Read out of second side band of resonator 1 mm x 1 mm x 50 µm.

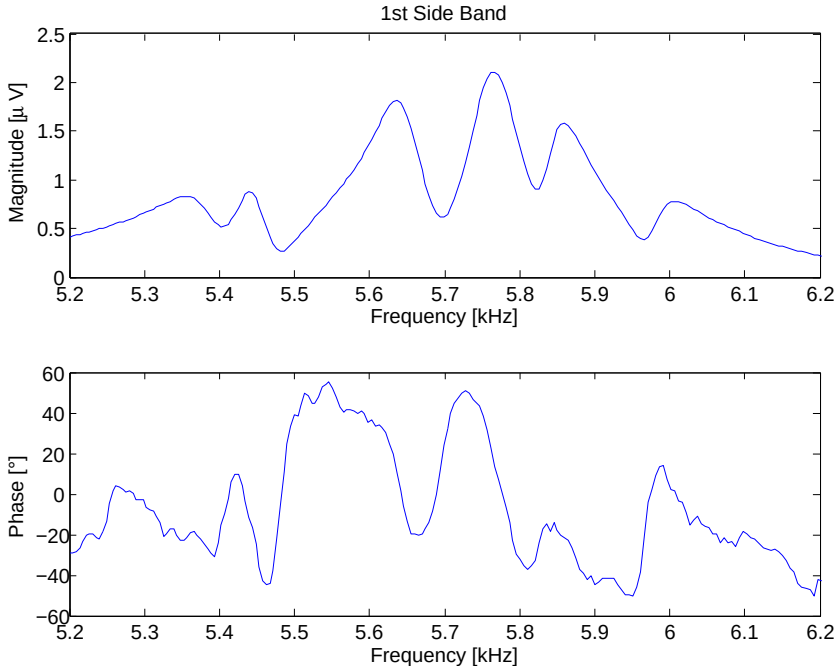

Figure 96: Magnetic read out of a row of six plate resonators 400 µm x 400 µm x 6 µm vibrating in in-plane direction.